

Alma Mater Studiorum – Università di Bologna

DOTTORATO DI RICERCA IN
INGEGNERIA ENERGETICA NUCLEARE
E DEL CONTROLLO AMBIENTALE

Ciclo XXI

Settore scientifico disciplinare di afferenza: ING-IND/10 Fisica Tecnica Industriale

TITOLO TESI

MAGNETOHYDRODYNAMIC EFFECTS ON MIXED
CONVECTION FLOWS IN CHANNELS AND DUCTS

Presentata da: *Ing. Valerio TOMARCHIO*

Coordinatore Dottorato

Chiar.mo Prof. Antonio BARLETTA

Relatore

Chiar.mo Prof. Antonio BARLETTA

Esame finale anno 2009

Magnetohydrodynamic Effects On Mixed Convection Flows In Channels And Ducts

V. Tomarchio

Contents

1	Introduction	2
1.1	Background and Motivation	2
1.1.1	Fundamental phenomena of MHD	3
1.1.2	Liquid metal flow meters and pumps	4
1.1.3	Metallurgy	6
1.1.4	MHD power generation	8
1.1.5	Fusion reactors breeding blankets	9
1.2	Closure	11
2	Mathematical Formulation	12
2.1	Assumptions	12
2.2	Governing equations	13
2.3	Boundary conditions	15
2.3.1	Dynamic boundary conditions	15
2.3.2	Thermal boundary conditions	16
2.3.3	Potential boundary conditions	16
2.4	Dimensionless formulation	19
2.5	Closure	20
3	MHD mixed convection flow in a vertical parallel channel with transverse magnetic field. Steady periodic regime	22
3.1	Governing equations	25
3.2	Analytical solution	28
3.3	Numerical solution	31

3.4	Results and Discussion	34
3.4.1	Velocity and temperature distributions	34
3.4.2	Influence of dissipative terms	37
3.4.3	Fanning friction factors and Nusselt numbers	38
3.5	Closure	44
4	MHD mixed convection flow in a vertical round pipe with transverse magnetic field. Steady periodic regime	46
4.1	Introduction	49
4.2	Governing equations	49
4.3	Solution	53
4.4	Results and Discussion	55
4.4.1	Forced stationary convection with MHD effects	59
4.4.2	Steady periodic mixed convection with MHD effects	60
4.5	Closure	63
5	MHD mixed convection flow in a vertical rectangular duct with transverse magnetic field. Steady periodic regime	68
5.1	Introduction	71
5.2	Governing equations	71
5.3	Solution	75
5.4	Results and Discussion	78
5.4.1	Forced stationary convection without MHD effects	82
5.4.2	Forced stationary convection with MHD effects	83
5.4.3	Steady periodic mixed convection with MHD effects	84
5.5	Closure	90
6	Conclusions	91
6.1	Closure	94
A	Auxiliary functions for the parallel channel problem	95
B	FORTTRAN95 code for the solution of the parallel channel problem	98

List of Figures

1.1	A simple MHD experiment.	4
1.2	A functional sketch of an MHD flowmeter.	6
1.3	A functional sketch of an MHD pump.	7
1.4	A typical setup for an electromagnetic stirrer.	8
1.5	A simple scheme of an MHD generator.	9
1.6	A typical layout of a breeding blanket.	10
2.1	A solid conducting walls example.	18
3.1	Representative scheme of the system	25
3.2	Mean velocity distributions across the channel for different values of M and GR . Frame (a) $GR = 500$, $M = 0$ (continuous), $M = 10$ (dashed), $M = 100$ (dotted). Frame (b) $M = 0$, $GR = 0$ (continuous), $GR = 100$ (dashed), $GR = 500$ (dotted).	35
3.3	Oscillating velocity amplitude distributions across the channel for different values of Ω and Pr in the non-magnetic case. Frame (a) $Pr = 5$, Frame (b) $Pr = 0.05$. $\Omega = 0.001$ (continuous), $\Omega = 100$ (dashed), $\Omega = 500$ (dotted).	35
3.4	Comparison of oscillating velocity amplitude distributions across the channel for different values of Ω between magnetic and non-magnetic case. Frame (a) $M = 0$, Frame (b) $M = 0.05$. $\Omega = 0.001$ (continuous), $\Omega = 100$ (dashed), $\Omega = 500$ (dotted).	36

3.5	Comparison of oscillating temperature amplitude distributions across the channel for different values of Ω and Pr . Frame (a) $M = 0$, $Pr = 0.05$, Frame (b) $M = 0$, $Pr = 5$. $\Omega = 0.001$ (continuous), $\Omega = 100$ (dashed), $\Omega = 500$ (dotted).	37
3.6	Comparison of average temperature distributions across the channel for $M = 0$ and different values of Br . $Br = 0$ (continuous), $Br = 2$ (dashed), $Br = 4$ (dotted).	38
3.7	Distribution of the average (a) and oscillating (b) velocity components across the channel for $Br = 0.25$ and different values of M . $M = 0$ (continuous), $M = 10$ (dashed), $M = 20$ (dotted).	39
3.8	Distribution of the average (a) and oscillating (b) temperature components across the channel for $Br = 0.25$ and different values of M . $M = 0$ (continuous), $M = 10$ (dashed), $M = 20$ (dotted).	40
3.9	Average component of the Fanning friction factor at the cold (a) and hot (b) walls plotted versus GR for different values of M . $M = 0$ (continuous), $M = 50$ (dashed), $M = 100$ (dotted).	40
3.10	Amplitude of the oscillating component of the Fanning friction factor at the cold wall plotted versus Ω for $Pr = 0.05$ (a) or $Pr = 5$ (b) and different values of M . $M = 0$ (continuous), $M = 50$ (dashed), $M = 100$ (dotted).	41
3.11	Amplitude of the oscillating component of the Fanning friction factor at the cold wall plotted versus Ω for $M = 0$ (a) or $M = 100$ (b) and different values of Pr . $Pr = 0.05$ (continuous), $Pr = 0.5$ (dashed), $Pr = 5$ (dotted).	42
3.12	Amplitude of the oscillating component of the Fanning friction factor at the hot wall plotted versus Ω for $Pr = 0.05$ (a) or $Pr = 5$ (b) and different values of M . $M = 0$ (continuous), $M = 50$ (dashed), $M = 100$ (dotted).	42

3.13	Amplitude of the oscillating component of the Fanning friction factor at the hot wall plotted versus Ω for $M = 0$ (a) or $M = 100$ (b) and different values of Pr . $Pr = 0.05$ (continuous), $Pr = 0.5$ (dashed), $Pr = 5$ (dotted).	43
3.14	Dimensionless heat flux Nu as a function of Ω at different locations inside the channel. Frame (a), $\xi = -0.25$ (continuous), $\xi = -0.15$ (dashed), $\xi = -0.05$ (dotted). Frame (b), $\xi = 0.05$ (continuous), $\xi = 0.15$ (dashed), $\xi = 0.25$ (dotted).	44
4.1	A sketch of the channel.	50
4.2	The discretization of the computational domain: (a) An overview of the whole domain, showing the structured boundary layers and the unstructured core. (b) A detailed view of the structured mesh close to the wall. The thickness of the first element is 10^{-7}	56
4.3	Distributions of average dimensionless velocity (a) (c) (e) and electric potential (b) (d) (f), calculated for $Ha = 0$ (a,b), $Ha = 20$ (c,d), $Ha = 50$ (e,f) for steady state forced convection with transverse magnetic field.	57
4.4	Arrow and streamline plots of the current density vector \mathbf{J} across the pipe cross section, calculated for $Ha = 10$ (a,b), $Ha = 50$ (c,d), $Ha = 100$ (e,f) for steady state forced convection with transverse magnetic field.	58
4.5	Behavior of $f_1 Re$ (a) and $f_2 Re$ (b) as functions of Ω obtained for $Ha = 0$ (continuous) $Ha = 5$ (dashed) and $Ha = 10$ (dotted) in mixed convection regime, with $GR = 500$ and $Pr = 0.05$	62
4.6	Behavior of Nu_1 (continuous) and Nu_2 (dashed) as functions of Ω in mixed convection regime with $Pr = 0.05$	63
4.7	Distributions of oscillation amplitudes for dimensionless velocity (a) (b), temperature (c) (d) and electric potential (e) (f), calculated for $Ha = 0$ in mixed convection regime, with $GR = 500$, $Pr = 0.05$ and $\Omega = 100$	64

4.8	Distributions of oscillation amplitudes for dimensionless velocity (a) (b), temperature (c) (d) and electric potential (e) (f), calculated for $Ha = 20$ in mixed convection regime, with $GR = 500$, $Pr = 0.05$ and $\Omega = 100$	65
4.9	Distributions of oscillation amplitudes for dimensionless velocity (a) (b), temperature (c) (d) and electric potential (e) (f), calculated for $Ha = 50$ in mixed convection regime, with $GR = 500$, $Pr = 0.05$ and $\Omega = 100$	66
5.1	A sketch of the channel.	72
5.2	The discretization of the computational domain: (a) An overview of the whole domain, showing the structured boundary layers and the unstructured core. (b) A detailed view of the structured mesh close to the wall. The thickness of the first element is 10^{-7}	79
5.3	Distributions of average dimensionless velocity (a) (c) (e) and electric potential (b) (d) (f), calculated for $Ha = 0$ (a,b), $Ha = 20$ (c,d), $Ha = 50$ (e,f) in a square channel ($\chi = 1$) for a steady state forced convection with transverse magnetic field.	80
5.4	Arrow and streamline plots of the current density vector \mathbf{J} across the duct cross section, calculated for $Ha = 10$ (a,b), $Ha = 50$ (c,d), $Ha = 100$ (e,f) for steady state forced convection with transverse magnetic field.	81
5.5	Behavior of $f_1 Re$, $f_2 Re$, Nu_1 and Nu_2 as functions of Ω obtained for $Ha = 5, 10, 20$. Results apply to a square channel $\chi = 1$ in mixed convection regime, with $GR = 500$, $Pr = 0.05$	85
5.6	Distributions of oscillation amplitudes for dimensionless velocity (a) (b), temperature (c) (d) and electric potential (e) (f), calculated for $Ha = 0$ and $\chi = 1$, in mixed convection regime, with $GR = 500$, $Pr = 0.05$ and $\Omega = 100$	86

5.7	Distributions of oscillation amplitudes for dimensionless velocity (a) (b), temperature (c) (d) and electric potential (e) (f), calculated for $Ha = 20$ and $\chi = 1$, in mixed convection regime, with $GR = 500$, $Pr = 0.05$ and $\Omega = 100$	87
5.8	Distributions of oscillation amplitudes for dimensionless velocity (a) (b), temperature (c) (d) and electric potential (e) (f), calculated for $Ha = 50$ and $\chi = 1$, in mixed convection regime, with $GR = 500$, $Pr = 0.05$ and $\Omega = 100$	88

List of Tables

2.1	A selection of parameters related to fusion experimental devices.	20
4.1	Values of $f Re$ as a function of Ha in stationary forced convection, $GR = 0, \Omega = 0$	60
4.2	Values of the oscillating amplitudes of $f Re$ and Nu as a function of Ω . Results obtained in mixed convection regime, with $Pr = 0.05$ and $GR = 500$	61
4.3	Values of the oscillating amplitudes of $f Re$ and Nu as a function of Ω . Results obtained in mixed convection regime, with $Pr = 1$ and $GR = 500$	61
5.1	Comparison between the factor $f Re_m$ obtained in the present work and the analytical solution available in literature (11). Stationary forced convection, $GR = 0, \Omega = 0$	83
5.2	Values of $f Re$ as a function of Ha in stationary forced convection, $GR = 0, \Omega = 0$	84
5.3	Values of the oscillating amplitudes of $f Re$ and Nu as a function of Ω . Results obtained for a square channel $\chi = 1$ in mixed convection regime, $GR = 500$	89

Acknowledgments

The Author wants to acknowledge the continuous help and support received throughout this project from the Department of Energetic, Nuclear and Environmental Control Engineering (DIENCA). In particular I would like to thank Prof. A. Barletta and Dr. E. Rossi di Schio for their competent, professional, yet friendly behavior. I have sincerely appreciated the possibility I was given to collaborate with them.

Foreword

This work focuses on magnetohydrodynamic (MHD) mixed convection flow of electrically conducting fluids enclosed in simple 1D and 2D geometries in steady periodic regime.

In particular, in Chapter one a short overview is given about the history of MHD, with reference to papers available in literature, and a listing of some of its most common technological applications, whereas Chapter two deals with the analytical formulation of the MHD problem, starting from the fluid dynamic and energy equations and adding the effects of an external imposed magnetic field using the Ohm's law and the definition of the Lorentz force. Moreover a description of the various kinds of boundary conditions is given, with particular emphasis given to their practical realization.

Chapter three, four and five describe the solution procedure of mixed convective flows with MHD effects. In all cases a uniform parallel magnetic field is supposed to be present in the whole fluid domain transverse with respect to the velocity field. The steady-periodic regime will be analyzed, where the periodicity is induced by wall temperature boundary conditions, which vary in time with a sinusoidal law. Local balance equations of momentum, energy and charge will be solved analytically and numerically using as parameters either geometrical ratios or material properties.

In particular, in Chapter three the solution method for the mixed convective flow in a 1D vertical parallel channel with MHD effects is illustrated. The influence of a transverse magnetic field will be studied in the

steady periodic regime induced by an oscillating wall temperature. Analytical and numerical solutions will be provided in terms of velocity and temperature profiles, wall friction factors and average heat fluxes for several values of the governing parameters.

In Chapter four the 2D problem of the mixed convective flow in a vertical round pipe with MHD effects is analyzed. Again, a transverse magnetic field influences the steady periodic regime induced by the oscillating wall temperature of the wall. A numerical solution is presented, obtained using a finite element approach, and as a result velocity and temperature profiles, wall friction factors and average heat fluxes are derived for several values of the Hartmann and Prandtl numbers.

In Chapter five the 2D problem of the mixed convective flow in a vertical rectangular duct with MHD effects is discussed. As seen in the previous chapters, a transverse magnetic field influences the steady periodic regime induced by the oscillating wall temperature of the four walls. The numerical solution obtained using a finite element approach is presented, and a collection of results, including velocity and temperature profiles, wall friction factors and average heat fluxes, is provided for several values of, among other parameters, the duct aspect ratio. A comparison with analytical solutions is also provided, as a proof of the validity of the numerical method.

Chapter six is the concluding chapter, where some reflections on the MHD effects on mixed convection flow will be made, in agreement with the experience and the results gathered in the analyses presented in the previous chapters. In the appendices special auxiliary functions and FORTRAN program listings are reported, to support the formulations used in the solution chapters.

Chapter 1

Introduction

1.1 Background and Motivation

Magnetohydrodynamics (MHD) is concerned with the flow of electrically conducting fluids in the presence of magnetic fields, either externally applied or generated within the fluid by inductive action. Its origin dates back to pioneering discoveries of Northrup, Hartmann, Alfvén, and others in the first half of the twentieth century. After 1950, the subject developed rapidly, and soon became well established as a field of scientific endeavor of great importance in various contexts: geomagnetism and planetary magnetism, astrophysics, nuclear fusion (plasma) physics, and liquid metal technology.

In the last years, a growing interest has been addressed to the study of magnetohydrodynamic effects on mixed and natural convective flows (1)-(6). Such interest in the topic is due to the large number of possible technological applications, like in metallurgy, where the quality of the materials, produced in a regime of controlled crystal growth, can be influenced by the effects of an external imposed magnetic field (7). Recently, being increased the efforts towards the realization of nuclear fusion machines, MHD effects in liquid metal flows are studied to design properly critical components (*e.g.* blankets) of experimental reactors (8).

In particular, in (1) an analytical solution is obtained for the natural

convection in a 2D rectangular cavity in a vertical magnetic field. Pan and Li (2) have studied mixed convection in a parallel vertical channel in a horizontal magnetic field, in microgravity conditions and with a sinusoidally oscillating gravity (g-jitter effect). In (3) the mixed convection in an horizontal circular channel is studied numerically in presence of a vertical uniform magnetic field. An experimental study of the natural convection of a $Na^{22}K^{78}$ alloy in a rectangular cavity with a vertical magnetic field was presented by Burr and Müller (4), demonstrating that magnetic field systematically reduces the heat exchange in the fluid. In (5), mixed convection in a vertical channel is studied considering the effect of viscous dissipation and Joule heating. Sposito and Ciofalo (6) obtained analytical solutions of the local balance equations for a fully developed mixed convection in a vertical parallel channel, with isothermal walls and various electrical boundary conditions.

In the following points a short overview of the fundamental phenomena and applications of MHD will be given.

1.1.1 Fundamental phenomena of MHD

Since the first half of the nineteenth century (1832), Faraday and his contemporaries knew about the existence of induced currents in conducting media, either solid or liquid, being in motion in a magnetic field. This phenomenon is quite dual, in fact two separate but strongly linked events may be described:

- the induced currents create themselves an induced magnetic field, perturbing the original one,
- the interaction between induced currents and total field appears, perturbing the original motion of the conducting media.

These are the two fundamental effects of MHD, which may be defined as the science of the motion of electrically conducting fluids under the action of magnetic fields. These two effects express the mutual interaction

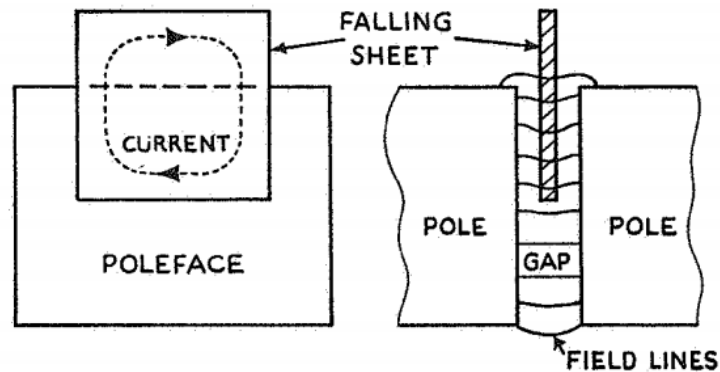


Figure 1.1 — A simple MHD experiment.

between the fluid velocity field and the electromagnetic field; the motion affects the magnetic field as well as the magnetic field affects the motion.

To appreciate these effects a simple experiment may be set up. Dropping a sheet of conducting material (*e.g.* aluminum) across a narrow gap between two magnets pole faces, results in a viscous damping of the falling motion of the sheet. The effects is more pronounced the higher is the conductivity of the material or the strength of the magnetic field. In the extreme situation of a sheet made of superconducting material, the viscous damping would diverge towards a quasi-elastic bouncing back of the sheet. It is interesting to note how the material properties of the moving conductor may change a non conservative viscous effect to a conservative elastic behavior. This simple experimental setup is sketched in Figure 1.1.

Since that time, several practical applications of these phenomena were studied. Some of them are briefly described in the following sections.

1.1.2 Liquid metal flow meters and pumps

Magnetic flowmeters, also known as electromagnetic flowmeters or induction flowmeters, are devices able to measure the velocity of a conducting fluid flowing into a duct which is crossed by a controlled magnetic field, by measuring the changes of induced voltage across the channel walls.

A typical magnetic flowmeter operates based upon Faraday's Law of

electromagnetic induction, which states that a voltage will be induced in a conductor moving through a magnetic field. The magnitude of the induced voltage E is directly proportional to the velocity of the conductor V , conductor width D , and the strength of the magnetic field B ,

$$E \propto BDV. \quad (1.1)$$

A schematic description of an MHD flowmeter is given in Figure 1.2: Two electrical coils are placed on the opposite sides of a pipe to generate a magnetic field which is transverse with respect to the fluid motion. As the electrically conductive fluid moves through the field with average velocity V , two electrodes placed on opposite sides of the pipe, on a line perpendicular to the direction of the magnetic field, sense the induced voltage. The distance between electrodes represents the width of the conductor D . An insulating liner prevents the signal from shorting to the pipe wall. The only variable in this application of Faraday's law is the velocity of the conductive liquid V because field strength is a controlled constant and the electrode spacing is fixed. Therefore, the output voltage E is directly proportional to liquid velocity, resulting in the linear output of a magnetic flow meter.

An MHD pump relies on the same principles of an MHD flowmeter, but applied in reverse order: the conducting fluid is confined into an insulating duct, where electrode plates are installed so to generate an electric field which is orthogonal to an externally impressed magnetic field. The electromotive force exerted by the electrode plates creates a current, and the moving charges are accelerated by the presence of the magnetic field. A typical setup of such device is given in Figure 1.3.

Electromagnetic pumps are commonly used in liquid-metal-cooled reactor plants where liquid lithium, sodium, potassium, or sodium-potassium alloys are used. Other metallic and nonmetallic liquids of sufficiently high electrical conductivity, such as mercury or molten aluminum, lead and bismuth, may also be pumped in nonnuclear applications. The absence of moving parts within the pumped liquid eliminates the need for seals and bearings that are found in conventional mechanical pumps,

thus minimizing leaks, maintenance, and repairs, and improving reliability. In liquid-metal-cooled nuclear reactor plants, electromagnetic pumps with a capacity of up to several thousand liters per minute have operated without maintenance for decades.

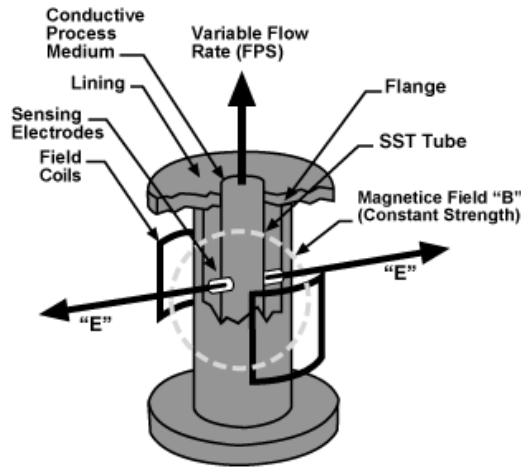


Figure 2.21 - The Magnetic Head Flow Meter

Figure 1.2 — A functional sketch of an MHD flowmeter.

1.1.3 Metallurgy

In the past decade, the continuous casting (CC) process has progressed markedly, has solved many technological problems, and has spread widely as a result. In the meantime, attempts to develop novel casting processes have been made for further innovation in the coming century. Among them, the application of MHD has aroused a great deal of interest as a powerful elementary technology to develop casting processes with higher productivity and better cast steel quality.

Non-contact force electromagnetic field influence on the liquid metal is known to be a component part of modern technological processes both in ferrous and non-ferrous metallurgy. With the help of electromagnetic field it is possible to stir metal in the melting machines, and during the non-furnace treatment. Therefore, the processing of alloy obtaining become

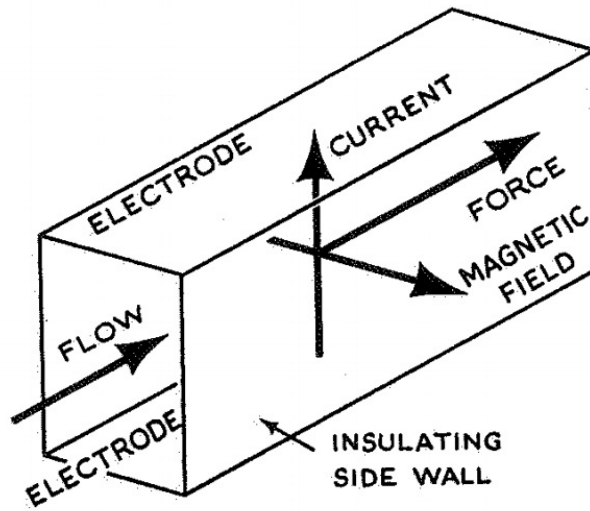


Figure 1.3 — A functional sketch of an MHD pump.

much simpler and accelerated, energy consumption per unit of metal mass is reduced, the working conditions in the metallurgical industry become better, metal quality increases, and the degree of process automation increases as well.

The application of MHD in the continuous casting process of steel has now advanced to electromagnetic stirring in the mold and the control of molten steel flow by an in-mold direct-current magnetic field brake. These applied MHD technologies are designed to improve further the continuous casting process capability. They improve the surface quality of cast steel by homogenizing the meniscus temperature, stabilizing the initial solidification, and cleaning the surface layer. They also improve the internal quality of steel slab by preventing the inclusions from penetrating deep into the strand pool and promoting the flotation of argon bubbles.

A typical electromagnetic stirring system, shown in Figure 1.4, consists of a MHD stirrer (pos. 1), thermal insulation (pos. 2) and melt (pos. 3). The importance of a good understanding of the MHD phenomena is relevant, with respect to this particular application, to predict the velocity distribution patterns in the furnace bath in order to control the quality of the produced material.

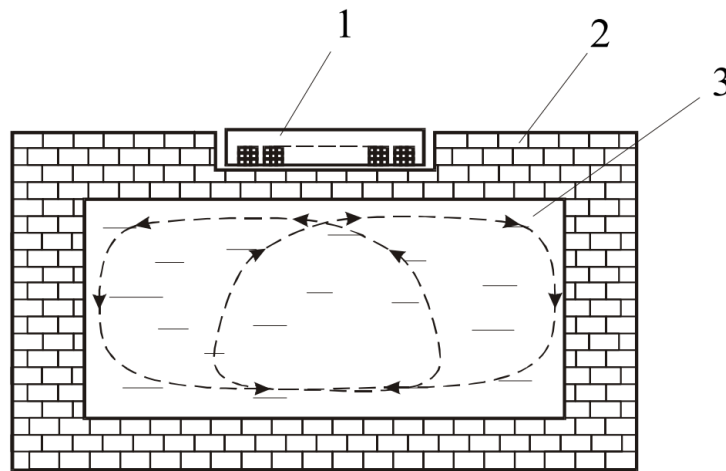


Figure 1.4 — A typical setup for an electromagnetic stirrer.

1.1.4 MHD power generation

MHD power generation is an advanced technology for generating electrical power from fossil fuels by passing an electrically conducting fluid through a magnetic field without rotating machinery or moving mechanical parts.

The underlying principle of MHD power generation is elegantly simple. Typically, an electrically conducting gas is produced at high pressure by combustion of a fossil fuel. The gas is then directed through a magnetic field, resulting in an electromotive force within it in accordance with Faraday's law of induction. The MHD system constitutes a heat engine, involving an expansion of the gas from high to low pressure in a manner similar to that employed in a conventional gas turbo generator. In the turbo generator, the gas interacts with blade surfaces to drive the turbine and the attached electric generator. In the MHD system, the kinetic energy of the gas is converted directly to electric energy as it is allowed to expand.

In principle, any electrical conducting fluid can be used as the working fluid, and power generation has been demonstrated with a number of such fluids, varying from liquid metals to hot ionized gases. The absence of moving machinery allows the MHD generator to operate at much higher

temperatures than other power generation systems and, therefore, higher efficiencies can be reached. A simple scheme of an MHD generator is given in Figure 1.5.

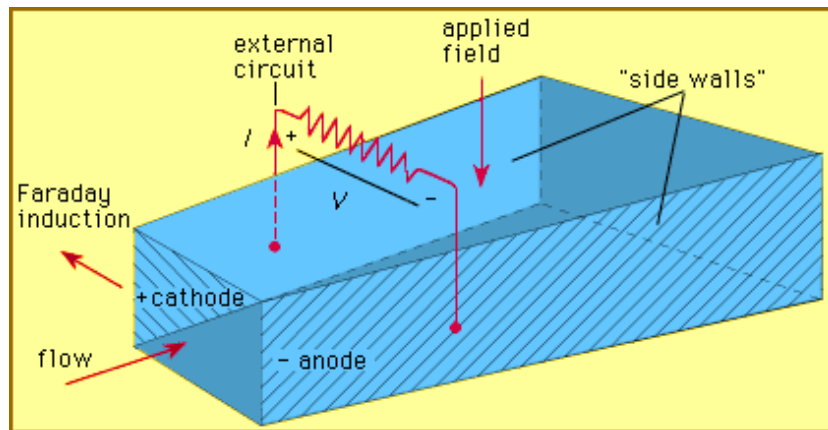


Figure 1.5 — A simple scheme of an MHD generator.

A MHD/steam plant can achieve efficiencies of up to 60% with less environmental impact than from any other direct coal-burning technology. Retrofitting and/or repowering of existing thermal power plants is possible with a significant increase of the efficiency of the plant. Efficiencies greater than 65-70 % can be reached if a triple cycle, including an MHD generator, a gas turbine and a steam turbine, is utilized.

1.1.5 Fusion reactors breeding blankets

In nuclear fission reactors, a reflector is a region of unfueled material surrounding the core. Its function is to scatter neutrons that leak from the core and thereby return some of them to the core. The liquid-metal reactor represents a special case. Most sodium-cooled reactors are deliberately built to allow a large fraction of their neutrons - those not needed to maintain the chain reaction - to leak from the core. These neutrons are valuable because they can produce new fissile material if they are absorbed by fertile material. Thus, fertile material - generally depleted uranium or its dioxide - is placed around the core to catch the leaking neutrons. Such an absorb-

ing reflector is referred to as a blanket or a breeding blanket.

In fusion experimental reactors where part of the fuel consists of Tritium, which is unavailable in nature, special mixtures of Lithium compounds are used in the breeding blankets, in order to trigger the production of Tritium as a consequence of neutron absorption and radioactive decay. Often the breeding material is accompanied by Beryllium neutron multipliers. Such blankets are still in developing phase, and some of their designs are based on a fluid flow of molten salts across narrow rectangular channels. A typical layout of a breeding blanket is given in Figure 1.6.

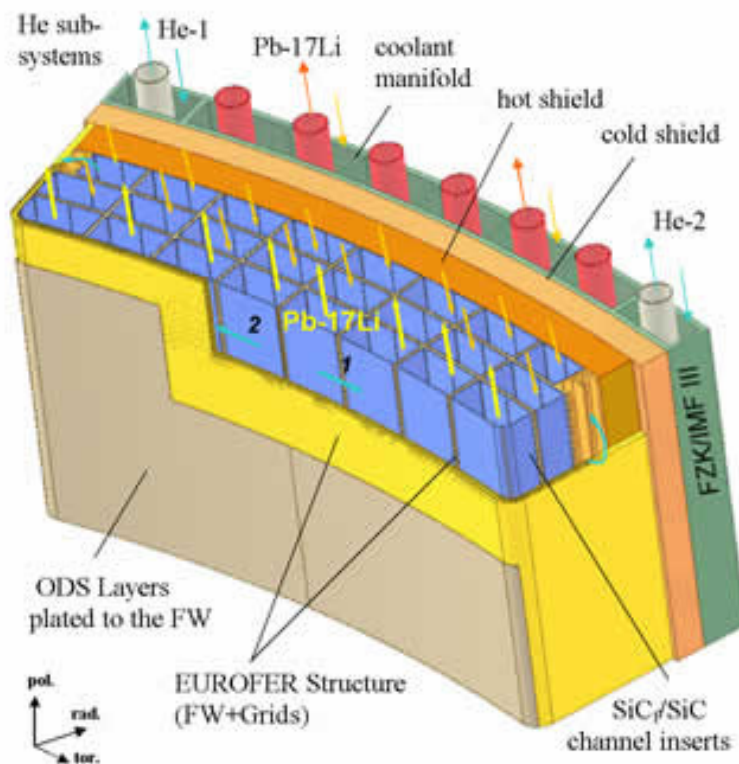


Figure 1.6 — A typical layout of a breeding blanket.

In such MHD flows in blanket channels, interaction of the induced electric currents with the applied plasma-confinement magnetic field results in the flow opposing Lorentz force that may lead to high MHD pressure drop, turbulence modifications, changes in heat and mass transfer

and other important MHD phenomena. In fact, even if liquid blanket designs have the best potential for high power density, MHD interactions of the flowing liquid with the confinement B-field may lead to:

- extreme MHD drag resulting in high blanket pressure and stresses, and flow balance disruption,
- velocity profile and turbulence distortion resulting in severe changes in heat transfer, corrosion and tritium transport.

MHD effects are specific to the blanket design. In self-cooled liquid metal blankets, the MHD pressure drop is considered as the main issue, while in self-cooled molten salt blankets, the blanket performance depends on the degree of turbulence suppression by a magnetic field.

1.2 Closure

This chapter was intended to give a broad but necessarily simplified overview of the history of MHD research and the applications which were envisaged and which are now reality.

In the following chapter the bulk of mathematical equations governing the MHD convective flow in channels and ducts will be investigated, starting from the basic momentum, energy and potential equations and combining them in a self-consistent system.

Chapter 2

Mathematical Formulation

In this chapter will be presented the framework of governing equations which will be used in the rest of the work. Starting from the three-dimensional formulation of the Navier-Stokes and energy conservation equations, the MHD terms will be derived under specific assumptions and included in the complete formulation.

In the next chapters specific geometries will be addressed, and the bulk of governing equations will be simplified accordingly to the problems to be illustrated.

2.1 Assumptions

This work deals with convective MHD flow of a conductive Newtonian fluid with constant thermophysical properties, enclosed in simple geometries in the presence of a transverse imposed magnetic field. The fluid is supposed to be incompressible and the flow to be laminar. The Oberbeck-Boussinesq approximation will be used to model buoyancy.

Moreover, the inductionless approximation is supposed to be valid, so that the magnetic Reynolds number,

$$R_m = \frac{UL}{\eta_m} \ll 1, \quad (2.1)$$

where U is a typical velocity scale of the flow, L is a typical length scale of

the flow and η_m is the magnetic diffusivity, defined as:

$$\eta_m = \frac{1}{\mu_0 \sigma_0}, \quad (2.2)$$

where μ_0 is the magnetic permeability of the medium and σ_0 its electrical conductivity.

In this situation, diffusion dominates induction by fluid motion, and the magnetic field in the fluid is determined, at least at leading order, by geometrical considerations (the geometry of the fluid domain and of the external current-carrying coils or magnets). The additional field induced by the fluid motion is weak compared with the applied field. This is the domain of liquid-metal magnetohydrodynamics in most circumstances of potential practical importance.

2.2 Governing equations

The starting framework of equations consists in the conservation of mass equation, the three dimensional Navier-Stokes equation, and the heat equation, expressed in their time-dependent form. The classical formulation of this equation system is:

$$\frac{\partial \rho}{\partial t} = \nabla \cdot \rho \mathbf{u} \quad (2.3)$$

$$\rho \left(\frac{\partial \mathbf{u}}{\partial t} + \mathbf{u} \cdot \nabla \mathbf{u} \right) = \rho \mathbf{g} - \nabla p + \mu \nabla^2 \mathbf{u} + \mathbf{f}_b + \mathbf{f}_L \quad (2.4)$$

$$\rho c_v \frac{DT}{Dt} = \nabla \cdot (k \nabla T) + D : \tau + q_J \quad (2.5)$$

where \mathbf{f}_b represents the buoyancy force term, \mathbf{f}_L the Lorentz force term, $D : \tau$ the viscous dissipation term and q_J the Joule dissipation term.

Making use of the Boussinesq approximation, the buoyancy term can be written as:

$$\mathbf{f}_b = -\rho_0 [1 - \beta(T - T_0)] \mathbf{g}, \quad (2.6)$$

where ρ_0 is the fluid density, considered constant, β is the thermal expansion coefficient and T_0 is a reference temperature for the fluid, chosen accordingly to the specific problem to be solved.

The Lorentz force and the Joule dissipation term will be discussed in detail in the following paragraphs.

Electric potential field. To describe the phenomena arising in the conducting fluid flowing through a magnetic field, an additional governing equation has to be included in the system, to account for the induced currents.

Starting from the continuum form of Ohm's equation, written in a reference frame which moves together with the fluid with velocity \mathbf{u} through a magnetic field \mathbf{B} , namely:

$$\mathbf{J} = \sigma(-\nabla\phi + \mathbf{u} \times \mathbf{B}), \quad (2.7)$$

and assuming that in the domain to be analyzed the conservation of charge is verified or, in other words:

$$\nabla \cdot \mathbf{J} = 0, \quad (2.8)$$

combining together (2.7) and (2.8) it is possible to obtain:

$$\nabla^2\phi = \nabla \cdot (\mathbf{u} \times \mathbf{B}). \quad (2.9)$$

This scalar equation describes the electric potential field which is established in the fluid due to its flowing through the magnetic field. The induced current distribution is given by (2.7) and due to the inductionless hypothesis the magnetic field arising from this current is negligible compared to the impressed one. Equation (2.9) has to be included in the system of equations (2.3) - (2.5) to complete the mathematical formulation.

Lorentz body force. The general expression of the Lorentz force per volume of fluid is:

$$\mathbf{f}_L = \mathbf{J} \times \mathbf{B}, \quad (2.10)$$

which can be written, following (2.7), as:

$$\mathbf{f}_L = \sigma(-\nabla\phi + \mathbf{u} \times \mathbf{B}) \times \mathbf{B}. \quad (2.11)$$

This term is included in (2.4) to take into consideration the effect of the magnetic field on the flow.

Joule dissipation. In general, the dissipative energy due to the flow of the current in the fluid can be written as:

$$q_J = \frac{1}{\sigma} |\mathbf{J}|^2 = \sigma |-\nabla\phi + (\mathbf{u} \times \mathbf{B})|^2 \quad (2.12)$$

and can be added in the right-hand side of (2.5) together with the viscous dissipation contribution.

Rewriting the system. In the aforementioned hypotheses, it is possible to rewrite the system of (2.3) - (2.5) including all the MHD effects as follows:

$$\nabla \cdot \mathbf{u} = 0 \quad (2.13)$$

$$\rho_0 \left(\frac{\partial \mathbf{u}}{\partial t} + \mathbf{u} \cdot \nabla \mathbf{u} \right) = \rho_0 \beta (T - T_0) \mathbf{g} - \nabla p + \mu \nabla^2 \mathbf{u} + \mathbf{J} \times \mathbf{B} \quad (2.14)$$

$$\rho c_v \frac{DT}{Dt} = \nabla \cdot (k \nabla T) + D : \tau + \sigma |-\nabla\phi + (\mathbf{u} \times \mathbf{B})|^2 \quad (2.15)$$

2.3 Boundary conditions

In this section the various types of boundary conditions, which will be adopted in the solution of the problems shown in the following chapters, will be analyzed. The closure of the system (2.13) - (2.15) is guaranteed by dynamic, thermal and electric potential boundary conditions.

2.3.1 Dynamic boundary conditions

These conditions define the dynamic behavior of the system at the boundary of the domain. Being this study oriented toward flow in ducts and channels, the dynamic boundary conditions are condensed in the no-slip hypothesis. This yields to:

$$\mathbf{u}(\Sigma, t) = 0, \quad (2.16)$$

where Σ is the domain boundary.

2.3.2 Thermal boundary conditions

In this work, convective flows in steady periodic regime will be analyzed. A steady periodic regime is a transient evolution of a system driven by a sinusoidal forcing, which stabilizes itself after a sufficiently high number of cycles. After the stabilization, the flow can be treated as a fully periodic flow, with the same frequency of the driving force, but possibly phase-shifted with respect to it.

In the sample problems solved in the following chapters, the driving force will be provided by wall temperature distributions sinusoidally changing over time. This can be expressed as:

$$T(\Sigma, t) = T_1(\Sigma) + T_2(\Sigma) \cos(\omega t), \quad (2.17)$$

where T_1 represents the average temperature of the wall and T_2 the oscillation amplitude of the wall temperature around its mean value. This varying temperature distribution may be applied to the whole boundary, Σ , or just to part of it. Examples will be given in the following chapters.

2.3.3 Potential boundary conditions

The nature of the walls material has a great influence on the solution of the magnetohydrodynamic convective flow problem in channel and ducts. In fact, depending on the conductivity of the walls, the distribution of electric potential across the fluid changes completely, thus affecting the current distribution in the channel cross section and the intensity of the Lorentz body forces.

Perfectly insulating walls. In the following chapters, the assumption of perfect electrically insulating walls will be adopted. This can be formalized as:

$$\mathbf{J} \cdot \mathbf{n} \Big|_{\Sigma} = 0, \quad (2.18)$$

where \mathbf{n} is the unit vector normal to the boundary Σ . This situation well represents practical applications of MHD phenomena, like the aforemen-

tioned electromagnetic flow meter. Moreover, the perfect electrical insulation decouples the electrodynamic problem in the fluid from that in the walls.

Perfectly conducting walls. In case of walls made of an extremely high conductivity material, the distribution of electric potential across the domain boundary is constant,

$$\phi(\Sigma, t) = \phi_0, \quad (2.19)$$

which can be arbitrarily set to zero. This circumstance is less realistic than that discussed before, and finds a few practical applications. Again, the electrodynamic problem in the fluid and in the wall is decoupled.

Conducting walls: solid walls. When the conductivity of the walls is neither zero nor infinite, the solution of the electrodynamic problem in the solid walls around the fluid is no more decoupled from that inside the fluid. This means that the two problems have to be solved simultaneously. This normally makes the system of governing equations more complicated and adds additional conditions at the internal boundary between fluid and walls. In Figure 2.1 a typical example of this situation is shown: the flow of a liquid metal in a steel conduit.

In this case, the continuity of electric potential and of the normal component of the vector \mathbf{J} are always verified at the boundary Γ between fluid and solid domains. In other words:

$$\mathbf{J} \cdot \mathbf{n} \Big|_{\Gamma} = \mathbf{J}_w \cdot \mathbf{n} \Big|_{\Gamma}; \quad \phi \Big|_{\Gamma} = \phi_w \Big|_{\Gamma}, \quad (2.20)$$

which constitutes, together with Poisson's equation for the electric potential,

$$\nabla^2 \phi_w = 0, \quad (2.21)$$

and the heat equation in the solid domain,

$$\rho_w c_{v,w} \frac{DT_w}{Dt} = \nabla \cdot (k_w \nabla T_w), \quad (2.22)$$

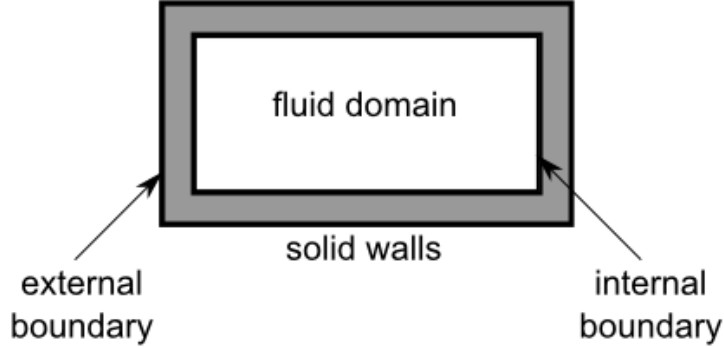


Figure 2.1 — A solid conducting walls example.

an additional set of equations to be incorporated and solved simultaneously with the equation system defined in the fluid domain.

The conclusions drawn before for the perfectly insulating or conducting walls is then transferred to the outer boundary of the conductive walls,

$$\mathbf{J}_w \cdot \mathbf{n} \Big|_{\Sigma} = 0, \quad (2.23)$$

which provides the final closure to the equation system.

Conducting walls: thin walls. In order to simplify the solution of the aforementioned conducting walls problem, without solving simultaneously for temperature, current and electric potential distribution in the solid walls domain, it is possible to use the thin walls approximation. This approximation implies that if the wall is sufficiently thin, the temperature and electric potential changes across the wall thickness can be neglected, together with the wall current density normal to the walls themselves. This allows to write the following closure equations, which have to be solved for the solid domain:

$$\mathbf{J} \cdot \mathbf{n} \Big|_{\Gamma} = \nabla \cdot (c \nabla \phi_w); \quad \phi \Big|_{\Gamma} = \phi_w \Big|_{\Gamma} = \phi_w \Big|_{\Sigma}, \quad (2.24)$$

where c is the conductance parameter, being,

$$c = \frac{\sigma_w t_w}{\sigma L} \quad (2.25)$$

which represents the ratio of thickness and electric resistance of the walls with respect to the fluid. This approach is broadly used in the solution of practical problems regarding liquid metal flows in metallic channels, as reported in (12).

2.4 Dimensionless formulation

Magnetohydrodynamic flows are studied for a broad range of materials and operating conditions: from seawater, in case of magnetic naval propulsion, to molten salts, in case of fast fission reactors, to liquid metals, in case of fusion reactor breeders or casting melts. Among all these cases, the materials range sweeps several orders of magnitudes of densities, viscosities and conductivities. The same can be said for the operating conditions, from the small magnetic fields of a lab setup to the stronger ones of superconducting coils, from the moderate temperatures of a sea stream to those extremely high of a steel continuous cast.

To set up a computational tool able to face the most diverse kinds of problems, a dimensional analysis of the set of equations obtained up to now has to be performed. With the dimensional analysis, in fact, it is possible to rewrite the mathematical model in a form which is independent of the thermophysical properties of the fluid, using a set of parameters obtained as dimensionless ratios of them.

Besides the well known Reynolds, Prandtl and Grashof numbers,

$$Re = \frac{U_0 D \rho_0}{\mu}; \quad Pr = \frac{\mu c_p}{\lambda}; \quad Gr = \frac{g \beta (T - T_0) D^3}{\nu^2}, \quad (2.26)$$

two new parameters will be introduced, to express the ratios of electromagnetic to inertial and viscous forces. These are the interaction parameter, or Stuart number:

$$N = \frac{\sigma L B_0^2}{\rho U_0}, \quad (2.27)$$

and the Hartmann number,

$$Ha = \sqrt{N Re} = L B_0 \sqrt{\frac{\sigma}{\rho_0 \nu}}, \quad (2.28)$$

Table 2.1 — A selection of parameters related to fusion experimental devices.

	ITER, ARIES	C-MOD	NSTX
Hartmann number, Ha	$\sim 10^3 - 10^5$	$\sim 500 - 1000$	$\sim 50 - 500$
Interaction parameter, N	$\sim 10^3 - 10^5$	$\sim 50 - 10^4$	$\sim 0.1 - 1$
Reynolds number, Re	$\sim 10^4 - 10^5$	$\sim 10^4 - 10^5$	$\sim 10^4 - 10^5$
Ha/Re	~ 0.1	~ 0.03	~ 0.003
Most likely flow regimes for insulating ducts	Laminar MHD	Laminar, weakly turbulent MHD	Turbulent MHD

which can cover a very wide range of values, depending on the application to be modeled. In Table 2.1 values of Ha , Re and N for a selection of fusion experimental devices are reported. It can be noted that, for similar values of the Reynolds number, the flow pattern changes from turbulent to laminar for increasing values of the Hartmann number. In fact, as it will be demonstrated in the following Chapters, one of the effects of a transverse magnetic field on the flow of an electrically conductive fluid is to suppress almost completely any kind of fluctuation (*e.g.* turbulence) in the velocity field.

It has to be stressed that the choice of the specific dimensionless groups and variables depends strictly on the problem to be solved. In the next chapters will be given examples of dimensional analysis of convective MHD problems, and analytical and numerical solutions will be presented.

2.5 Closure

This chapter was intended to define the bulk of equations which will be used in the following to solve MHD convective flow problems in simple 1D and 2D geometries. The system of equations is derived from the complete 3D unsteady mass, momentum and energy balance equations, with the addition of the Poisson equation for the electric potential. Special closure equations are defined to create the mutual influence between motion and magnetic field, descending directly from the definition of the generalized Ohm's law and Lorentz force, and to model the behavior at the boundaries of the domain.

The equation system (2.3) - (2.5) will be adapted case by case to the spe-

cific problem to be solved, in order to simplify the equations by removing the unnecessary terms. Also the equations resulting from the dimensional analysis will be adapted to fit the specific set of thermophysical properties and geometrical parameters of the problem under investigation. In the following chapters, either analytical or numerical solutions will be presented, and the results will be critically discussed.

Chapter 3

MHD mixed convection flow in a vertical parallel channel with transverse magnetic field. Steady periodic regime

Symbols used in the section

$A(t)$	function of time, defined in (3.7)
A_1	integration constant
B	intensity of the magnetic field
Br	Brinkman's number
\mathbf{g}	gravitational acceleration
g	modulus of the gravitational acceleration
Gr	Grashof number, defined in (3.12)
i	imaginary unit
I_n	modified Bessel function of first kind and order n
K_n	modified Bessel function of second kind and order n
L	channel half width
M	Hartmann number, defined in (3.13)
n	integer number
p	pressure
P	difference between the pressure and the hydrostatic pressure
Pr	Prandtl number, defined in (3.12)
Re	Reynolds number, defined in (3.12)
\Re	real part of a complex number
t	time
T	temperature
T_0	mean value of the wall temperature
ΔT	amplitude of the wall temperature oscillation
\mathbf{U}	fluid velocity
U	axial component of the fluid velocity
U_0	average value of the fluid velocity
u	dimensionless axial component of the fluid velocity, defined in (3.10)
u^*	dimensionless complex valued function, defined in (3.20)
u_a^*, u_b^*	dimensionless complex valued function, defined in (3.24)
X	longitudinal coordinate
Y	wall-normal coordinate

y dimensionless wall-normal coordinate, defined in (3.10)

Greek Symbols

α thermal diffusivity

β thermal expansion coefficient

η dimensionless time, defined in (3.10)

θ dimensionless temperature, defined in (3.11)

θ^* dimensionless complex valued function, defined in (3.21)

θ_a^*, θ_b^* dimensionless complex valued functions, defined in (3.25)

λ dimensionless parameter, defined in (3.11)

λ^* dimensionless complex valued function, defined in (3.22)

λ_a^*, λ_b^* dimensionless complex valued functions, defined in (3.26)

μ dynamic viscosity

ν kinematic viscosity

ϱ_0 fluid density at the reference temperature

ω frequency of the wall temperature oscillation

Ω dimensionless frequency, defined in (3.13)

Ω' dimensionless parameter, defined in (3.13)

In this chapter, mixed convection in a vertical parallel channel will be analyzed. MHD effects, due the presence of a uniform magnetic field orthogonal to the flow direction, are taken into account. The thermal boundary condition considered is such that one of the wall temperatures varies sinusoidally with time, while the other wall has a constant temperature. Reference is made to parallel fully-developed flow, in steady periodic regime. The local balance equations are expressed accordingly, and two boundary value problems are obtained, accounting for the mean value and the oscillating term of the velocity and temperature distributions respectively. The obtained boundary value problems are then solved analytically and numerically.

3.1 Governing equations

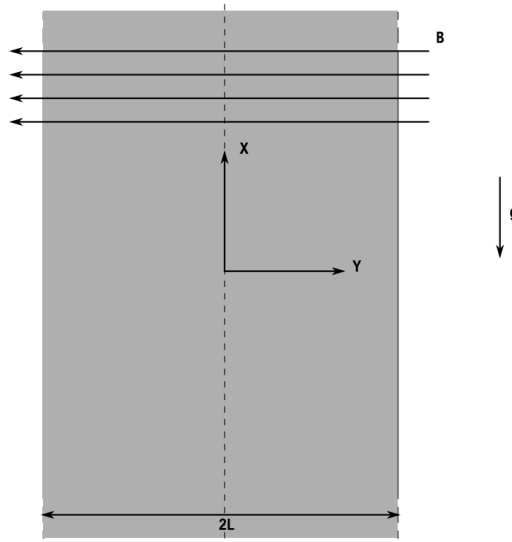


Figure 3.1 — Representative scheme of the system

In this section, the governing equations describing the phenomenon will be presented and written in a dimensionless form.

Let us consider a Newtonian fluid with constant thermophysical properties flowing in a vertical parallel channel having width $2L$, as shown

in Figure 3.1. Let us choose the axial coordinate X parallel to the gravitational acceleration \mathbf{g} but with opposite direction, and let us assume a uniform magnetic field having intensity B in the direction orthogonal to X . Reference is made to parallel and laminar flow, so that the only non-vanishing component of the velocity vector \mathbf{U} is the X -component U . As it is well known, the hypothesis of parallel flow in mixed convection implies that the buoyancy forces are not too intense; the hypothesis of parallel flow is realistic just for sufficiently small values of the Grashof number. The viscous dissipation and Joule heating effects will be neglected and the Boussinesq approximation will be invoked. Under the above described assumptions, the velocity field must be solenoidal, i.e. $U = U(Y, t)$. The thermal boundary conditions prescribed at $Y = \pm L$ are,

$$T(X, -L, t) = T_1, \quad (3.1)$$

$$T(X, +L, t) = T_2 + \Delta T \cos(\omega t). \quad (3.2)$$

Since the boundary conditions do not imply heating or cooling of the fluid, heat transfer arises only in the wall-normal direction and $T = T(Y, t)$. Moreover, the quantity:

$$T_0 = \frac{\omega}{4\pi L} \int_0^{2\pi/\omega} dt \int_{-L}^L dy T(y, t), \quad (3.3)$$

will be defined, which represents the mean value of the fluid temperature in a period, and which will be chosen as reference temperature value within the Boussinesq approximation.

Since the flow rate is steady, the mean velocity of the fluid in a duct section,

$$U_0 = \frac{1}{2L} \int_{-L}^L U(Y, t) dY. \quad (3.4)$$

does not depend on time.

Thus, simplifying the momentum equation (2.14), the X and Y components of the local momentum balance equation may be written as:

$$\varrho_0 \frac{\partial U}{\partial t} = - \frac{\partial P}{\partial X} + \varrho_0 g \beta (T - T_0) + \mu \nabla^2 U - \sigma U B^2, \quad (3.5)$$

$$\frac{\partial P}{\partial Y} = 0 \quad , \quad (3.6)$$

where the quantity $P = p + \varrho_0 g \beta$ has been introduced. Equation (3.6) implies $P = P(X, t)$. By differentiating with respect to X both sides of (3.5) one obtains $\partial^2 P / \partial X^2 = 0$. One can then define a function $A(t)$ such that

$$\frac{\partial P}{\partial X} = -A(t) \quad , \quad (3.7)$$

and (3.5) can be rewritten as

$$\varrho_0 \frac{\partial U}{\partial t} = A(t) + \varrho_0 g \beta (T - T_0) + \mu \frac{\partial^2 U}{\partial Y^2} - \sigma U B^2 \quad . \quad (3.8)$$

The complete local energy balance equation is

$$\frac{\partial T}{\partial t} = \alpha \frac{\partial^2 T}{\partial y^2} + \frac{\nu}{C_p} \left(\frac{\partial U}{\partial Y} \right)^2 + \frac{\sigma U^2 B^2}{\rho_0 C_p} \quad . \quad (3.9)$$

where the last two terms account for the viscous and ohmic dissipations. These two non-linear terms will be neglected during the derivation of the analytical solution of the problem.

Let us introduce the following dimensionless quantities:

$$u = \frac{U}{U_0}, \quad y = \frac{Y}{D}, \quad \eta = \omega t, \quad (3.10)$$

$$\theta = \frac{T - T_0}{\Delta T}, \quad \theta_{1,2} = \frac{T_{1,2} - T_0}{\Delta T}, \quad \lambda = \frac{A(t)D^2}{\mu U_0}, \quad (3.11)$$

$$Gr = \frac{g\beta\Delta T D^3}{\nu^2}, \quad Re = \frac{U_0 D}{\nu}, \quad Pr = \frac{\nu}{\alpha}, \quad Br = \frac{\mu U_0^2}{k\Delta T}, \quad (3.12)$$

$$\Omega = \frac{D^2 \omega}{\nu}, \quad M^2 = \frac{\sigma B^2 D^2}{\mu}, \quad GR = \frac{Gr}{Re}, \quad (3.13)$$

where $D = 4L$ is the hydraulic diameter of the channel. Using the defined dimensionless groups, (3.8) and (3.9) can be rewritten as:

$$\Omega \frac{\partial u}{\partial \eta} = \lambda + \frac{Gr}{Re} \theta + \frac{\partial^2 u}{\partial y^2} - M^2 u \quad , \quad (3.14)$$

$$\Omega Pr \frac{\partial \theta}{\partial \eta} = \frac{\partial^2 \theta}{\partial y^2} + Br \left(\frac{\partial u}{\partial y} \right)^2 + M^2 Br u^2. \quad (3.15)$$

The boundary condition for the dimensionless velocity and for the dimensionless temperature are:

$$u(-1/4, \eta) = u(1/4, \eta) = 0, \quad (3.16)$$

$$\theta(-1/4, \eta) = \theta_1, \quad (3.17)$$

$$\theta(1/4, \eta) = \theta_2 + \cos(\eta). \quad (3.18)$$

Moreover, (3.4) provides a constraint for the dimensionless velocity:

$$\frac{1}{2} = \int_{-1/4}^{1/4} u(y, \eta) dy. \quad (3.19)$$

3.2 Analytical solution

In the steady periodic regime it is possible to solve the governing equations analytically, by neglecting the non linear dissipation terms. Let us consider the functions $u(y, \eta)$, $\theta(y, \eta)$ and $\lambda(\eta)$ as real parts of three complex valued functions:

$$u(y, \eta) = \Re e[u^*(y, \eta)] , \quad (3.20)$$

$$\theta(y, \eta) = \Re e[\theta^*(y, \eta)] , \quad (3.21)$$

$$\lambda(\eta) = \Re e[\lambda^*(\eta)] . \quad (3.22)$$

The functions $u^*(y, \eta)$, $\theta^*(y, \eta)$ and $\lambda^*(\eta)$ must fulfill the following boundary value problem:

$$\left\{ \begin{array}{l} \Omega \frac{\partial u^*}{\partial \eta} = \frac{\partial^2 u^*}{\partial y^2} - M^2 u^* + GR\theta^* + \lambda^*, \\ \Omega Pr \frac{\partial \theta^*}{\partial \eta} = \frac{\partial^2 \theta^*}{\partial y^2}, \\ u^*(-1/4, \eta) = 0 = u^*(1/4, \eta), \\ \theta^*(-1/4, \eta) = \theta_1, \quad \theta^*(1/4, \eta) = \theta_2 + e^{i\eta}, \\ \int_{-1/4}^{1/4} u^*(y, \eta) dy = \frac{1}{2}, \end{array} \right. \quad (3.23)$$

Assuming that

$$u^*(y, \eta) = u_a^*(y) + GR u_b^*(y) e^{i\eta} , \quad (3.24)$$

$$\theta^*(y, \eta) = \theta_a^*(y) + \theta_b^*(y) e^{i\eta} , \quad (3.25)$$

$$\lambda^*(\eta) = \lambda_a^* + GR \lambda_b^* e^{i\eta} , \quad (3.26)$$

it is possible to obtain two boundary value problems:

$$\left\{ \begin{array}{l} \frac{d^2 u_a^*}{dy^2} - M^2 u_a^* + GR \theta_a^* + \lambda_a^* = 0, \\ \frac{d^2 \theta_a^*}{dy^2} = 0, \\ u_a^*(-1/4) = 0 = u_a^*(1/4), \\ \theta_a^*(-1/4) = \theta_1, \quad \theta_a^*(1/4) = \theta_2, \\ \int_{-1/4}^{1/4} u_a^*(y) d\xi = \frac{1}{2}, \end{array} \right. \quad (3.27)$$

and

$$\left\{ \begin{array}{l} \frac{d^2 u_b^*}{dy^2} - (M^2 + i\Omega) u_b^* + \theta_b^* + \lambda_b^* = 0, \\ \frac{d^2 \theta_b^*}{dy^2} - i\Omega Pr \theta_b^* = 0, \\ u_b^*(-1/4) = 0 = u_b^*(1/4), \\ \theta_b^*(-1/4) = 0, \quad \theta_b^*(1/4) = 1, \\ \int_{-1/4}^{1/4} u_b^*(y) dy = 0. \end{array} \right. \quad (3.28)$$

The boundary value problem (3.27) describes the mean value of the complex fields u^* , θ^* e λ^* , while the boundary value problem (3.28) provides the oscillating parts of the same quantities.

The solution of the boundary value problem (3.27) is:

$$\theta_a^*(y) = 4\theta_2 y \quad \text{with} \quad \theta_2 = -\theta_1 \quad (3.29)$$

$$\lambda_a^* = \frac{M^3(e^{M/2} + 1)}{Me^{M/2} + M - 4e^{M/2} + 4} \quad (3.30)$$

$$\begin{aligned} u_a^*(y) = & 4\frac{GR\theta_2 y}{M^2} + \frac{M(e^M - 1)}{Me^M - M - 4e^M + 8e^{M/2} - 4} + \\ & - 2\frac{GR\theta_2 e^{M/4} \sinh(My)}{M^2(e^{M/2} - 1)} + \\ & - 2\frac{M(e^M - 1)e^{M/4} \cosh(My)}{(Me^M - M - 4e^M + 8e^{M/2} - 4)(e^{M/2} + 1)}. \end{aligned} \quad (3.31)$$

As expected, in the limit $M \rightarrow 0$, one obtains the classical expression for the dimensionless velocity distribution,

$$\lim_{M \rightarrow 0} u_a^*(y) = -\frac{1}{24}(36 + GR\theta_2 y)(-1 + 16y^2) \quad (3.32)$$

The dimensionless temperature θ_b^* solution of (3.28) is

$$\theta_b^*(y) = \frac{-e^{1/4(1-4y)\sqrt{i\Omega Pr}} + e^{1/4(3+4y)\sqrt{i\Omega Pr}}}{-1 + e^{\sqrt{i\Omega Pr}}}, \quad (3.33)$$

which can be substituted in the momentum equation of the boundary problem (3.28) to obtain an expression of the dimensionless velocity:

$$\begin{aligned} u_b^*(y) = & [A_{1,a}(M, \Omega, Pr) + A_{1,b}(M, \Omega)\lambda_b^*(M, \Omega, Pr)] \Phi_1(\xi, M, \Omega) + \\ & + [A_{2,a}(M, \Omega, Pr) + A_{2,b}(M, \Omega)\lambda_b^*(M, \Omega, Pr)] \Phi_2(\xi, M, \Omega) + \\ & - \lambda_b^*(M, \Omega, Pr)\Phi_3(\xi, M, \Omega) + \Phi_4(\xi, M, \Omega, Pr). \end{aligned} \quad (3.34)$$

The dimensionless pressure gradient can be determined using the integral constraint in (3.28) and is:

$$\lambda_b^* = \frac{-\Psi_{1,a}(M, \Omega, Pr) - \Psi_{2,a}(M, \Omega, Pr) - \Psi_4(M, \Omega, Pr)}{\Psi_{1,b}(M, \Omega) + \Psi_{2,b}(M, \Omega) - \Psi_3(M, \Omega)}, \quad (3.35)$$

where the functions A , Φ and Ψ are reported in the appendix.

3.3 Numerical solution

To support the analytical investigation of the magnetohydrodynamic effects on a steady-periodic, mixed-convective flow in a parallel channel, a finite differences scheme has been adopted to provide a comparison benchmark for the analytical results, and to extend the validity of the solution to the non-linear case. A first order forward-Euler time discretization scheme was adopted for the present implementation, with second order central difference spatial derivatives.

The problem to be solved consists in a system of two PDEs, (3.14) and (3.15), together with the boundary conditions, (3.16) - (3.18). The system will be solved with respect to the variables u and θ , but the results will be expressed in terms of average value and oscillation amplitude $u_a, |u_b|, \theta_a, |\theta_b|$, to ease the comparison with respect to the analytical results presented previously.

To apply the finite differences method, the domain $y = [-1/4, 1/4]$ of the problem is discretized with a mesh of N_y equally spaced points. From this assumption (3.14) and (3.15) can be rewritten for each internal mesh point as:

$$\Omega Pr \frac{\theta_i^{j+1} - \theta_i^j}{\Delta \eta} = \frac{\theta_{i+1}^j - 2\theta_i^j + \theta_{i-1}^j}{\Delta y^2} + Br \left(\frac{u_{i+1}^j - u_{i-1}^j}{2\Delta y} \right)^2 + M^2 Br u_i^{j2} \quad (3.36)$$

and,

$$\Omega \frac{u_i^{j+1} - u_i^j}{\Delta \eta} = \frac{u_{i+1}^j - 2u_i^j + u_{i-1}^j}{\Delta y^2} - M^2 u_i^{j2} + GR\theta_i^j + \lambda \quad (3.37)$$

In a forward-advancing scheme, for each time step j , the values at the internal mesh points i of the function $\theta(y, \eta)$ at the time step $j + 1$ are obtained solving the (3.36) for θ_i^{j+1} . This yields the set of linear equations:

$$\theta_i^{j+1} = \theta_i^j + \frac{\Delta \eta}{\Omega Pr} \left[\frac{\theta_{i+1}^j - 2\theta_i^j + \theta_{i-1}^j}{\Delta y^2} + Br \left(\frac{u_{i+1}^j - u_{i-1}^j}{2\Delta y} \right)^2 + M^2 Br u_i^{j2} \right], \quad (3.38)$$

with $i = 2 \dots N_r - 1$.

The value of the dimensionless temperature θ_i at the boundary mesh points, $i = 1, N_y$, is given by the boundary conditions (3.17) - (3.18), which can be expressed as:

$$\theta_1^{j+1} = -\theta_2, \quad (3.39)$$

$$\theta_{N_y}^{j+1} = \theta_2 + \cos \eta, \quad (3.40)$$

for each j . To determine the velocity field for any internal mesh point, one has to solve the (3.37) for u_i^{j+1} , as:

$$u_i^{j+1} = u_i^j \left[1 - \frac{\Delta\eta}{\Omega} M^2 \right] + \frac{\Delta\eta}{\Omega} [\lambda^j + GR \theta_i^j] + \frac{\Delta\eta}{\Omega} \left[\frac{u_{i+1}^j - 2u_i^j + u_{i-1}^j}{\Delta y^2} \right], \quad (3.41)$$

while, at the wall boundaries, the no-slip condition yields:

$$u_1^{j+1} = 0, \quad (3.42)$$

$$u_{N_y}^{j+1} = 0, \quad (3.43)$$

for each j .

Then, even if it is possible in principle to determine the value of u_i^j for each mesh point of the domain using the (3.41), the dimensionless pressure gradient λ^j is still an unknown function of the time step j . Its value can be determined using the integral constraint equation (3.19) rewritten in finite terms as:

$$\sum_{i=1}^{N_r} u_i^{j+1} \Delta y = 1/2, \quad (3.44)$$

where the dimensionless velocity u_i^{j+1} can be expressed as:

$$u_i^{j+1} = a_i + b_i(\lambda^j + c_i), \quad (3.45)$$

where

$$a_i = u_1^j \left[1 - \frac{\Delta\eta}{\Omega} M^2 \right], \quad (3.46)$$

$$b_i = \frac{\Delta\eta}{\Omega}, \quad (3.47)$$

$$c_i = GR \theta_i^j + \left[\frac{u_{i+1}^j - 2u_i^j + u_{i-1}^j}{\Delta y^2} \right]. \quad (3.48)$$

By properly managing the sums, Eq. (3.44) can be rewritten as

$$\begin{aligned} \sum_{i=1}^{N_y} u_i^{j+1} \Delta y &= \sum_{i=1}^{N_y} [a_i + b_i(\lambda^j + c_i)] \Delta y = \\ &= \sum_{i=1}^{N_y} a_i \Delta y + \lambda^j \sum_{i=1}^{N_y} b_i \Delta y + \sum_{i=1}^{N_y} b_i c_i \Delta y = 1/2, \end{aligned} \quad (3.49)$$

and, the dimensionless pressure gradient can be evaluated as

$$\lambda^j = \frac{1/2 - A - BC}{B}, \quad (3.50)$$

where

$$A = \sum_{i=1}^{N_y} a_i \Delta y, \quad (3.51)$$

$$B = \sum_{i=1}^{N_y} b_i \Delta y, \quad (3.52)$$

$$BC = \sum_{i=1}^{N_y} b_i c_i \Delta y. \quad (3.53)$$

So, for each time step j , the dimensionless pressure gradient λ^j shall be initialized to an arbitrary value. The temperature field will be computed using Eq. (3.38) and a first tentative velocity field will be obtained from Eq. (3.41). Of course the specialized equations will be used for the boundary nodes. After the first computation of the velocity field, the constraint equation in its inverse form (3.50) will be used to obtain a new value of the pressure gradient. This new value will be then used to compute again the velocity field, and so on until a sufficient convergence of λ^j is obtained. After that, the time step will be incremented, and the calculation will continue.

The previous steps yield a complete overview of the fluid dimensionless velocity and temperature for each time step. To get some information on amplitude and phase shift of the oscillations, an additional stability check has to be done.

For each period of the wall temperature oscillation, a sum-of-square-errors check is made on the dimensionless quantities. If the velocity profile has sufficiently small changes at the end of a given period, within a prescribed tolerance, then the amplitude of the oscillation is computed from the difference between the maximum-velocity value minus the mean-velocity one, evaluated at each node, through the whole period.

The same approach can be used for the phase shift, evaluating the difference between the time of the maximum driving temperature and the time of the local maximum of the oscillating quantities, after the stabilization and in the range of a complete period.

3.4 Results and Discussion

In this section, first the most interesting features of the analytical solution will be described. In particular, the influence of the parameters M , Ω and Pr on the oscillation amplitude of the velocity field will be discussed.

3.4.1 Velocity and temperature distributions

In Figure 3.2(a), the mean velocity distribution is reported for three different values assumed by the Hartmann number M , assuming conditions of asymmetric heating, with $\theta_2 = 1$. The case $M = 0$ corresponds to the classical solution for the parallel channel without MHD effects. The presence of a uniform magnetic field redistributes the flow, counteracting the flow reversal at the cold wall. For high values of M , the dimensionless velocity assumes a typical flat Hartmann profile.

In Figure 3.2(b) is shown the effect of the dimensionless group GR on the flow distribution: for higher values of GR , the buoyancy forces become a relevant contribution and the mixed convective scheme drifts towards natural convection.

In Figure 3.3, the amplitude of the oscillating component of the dimensionless velocity is shown for several values of the dimensionless frequency. It is possible to see how the value of the Prandtl number influ-

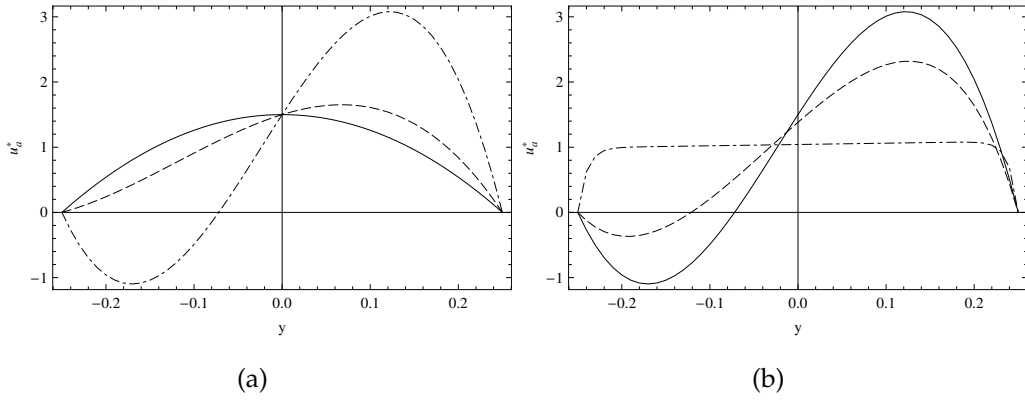


Figure 3.2 — Mean velocity distributions across the channel for different values of M and GR . Frame (a) $GR = 500$, $M = 0$ (continuous), $M = 10$ (dashed), $M = 100$ (dotted). Frame (b) $M = 0$, $GR = 0$ (continuous), $GR = 100$ (dashed), $GR = 500$ (dotted).

ences the penetration depth of the velocity oscillations. While the velocity oscillates across all the channel in the low Pr case (Figure 3.3(b)) even for high frequencies, for a high Pr fluid (Figure 3.3(a)) the oscillations of velocity experience a fast decay across the width of the channel and are confined just close to the hot wall. This effects increases for increasing dimensionless frequencies.

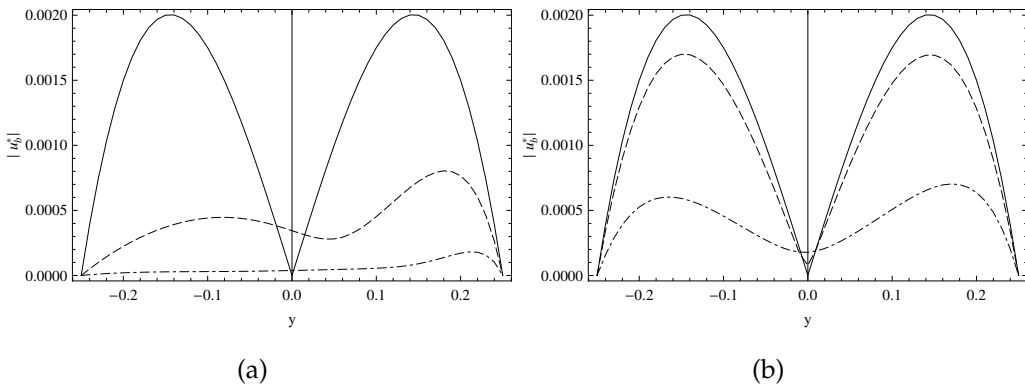


Figure 3.3 — Oscillating velocity amplitude distributions across the channel for different values of Ω and Pr in the non-magnetic case. Frame (a) $Pr = 5$, Frame (b) $Pr = 0.05$. $\Omega = 0.001$ (continuous), $\Omega = 100$ (dashed), $\Omega = 500$ (dotted).

In Figure 3.4 the influence of the external magnetic field on the amplitude of the velocity oscillations is shown. For increasing values of the

parameter M , the velocity oscillations are dampened accordingly. Figure 3.4(a) shows the non MHD case with $M = 0$, while (Figure 3.4(b)) shows the behavior of the system at $M = 0.05$. Even for such a small Hartmann number, the high frequency oscillations are completely suppressed. The damping of oscillations (*e.g.* turbulence) is a well known effect induced by transverse fields on flows of conductive fluids, and has great impact on the estimation of hydraulic losses and flow patterns in many applications.

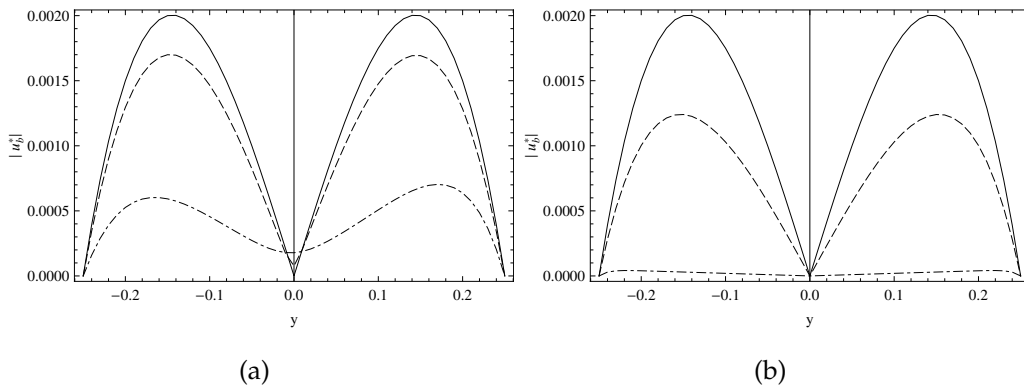


Figure 3.4 — Comparison of oscillating velocity amplitude distributions across the channel for different values of Ω between magnetic and non-magnetic case. Frame (a) $M = 0$, Frame (b) $M = 0.05$. $\Omega = 0.001$ (continuous), $\Omega = 100$ (dashed), $\Omega = 500$ (dotted).

Figure 3.5 shows the amplitude of the oscillating component of the dimensionless temperature across the channel. In analogy with the velocity, the penetration depth of the temperature oscillation is greatly affected by the Prandtl number: in fact, while for low Prandtl fluids (Figure 3.5(a)) the temperature oscillates across the whole width of the channel even for high values of the dimensionless pulsation Ω , for high Prandtl fluids (Figure 3.5(b)) the temperature oscillation is segregated only close the the hot wall. This last behavior is typical of the molten salts used either as coolant or breeding material in several kinds of nuclear reactors, like Fluorine-Lithium-Beryllium compounds, while the first behavior is typical of liquid metals, like mercury, where thermal diffusivity is dominant with respect to viscosity.

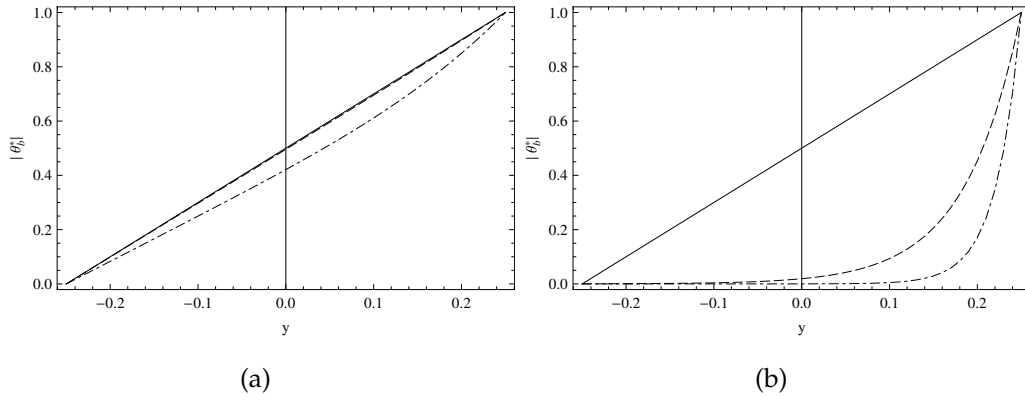


Figure 3.5 — Comparison of oscillating temperature amplitude distributions across the channel for different values of Ω and Pr . Frame (a) $M = 0$, $Pr = 0.05$, Frame (b) $M = 0$, $Pr = 5$. $\Omega = 0.001$ (continuous), $\Omega = 100$ (dashed), $\Omega = 500$ (dotted).

3.4.2 Influence of dissipative terms

Figures 3.6 - 3.8 show some of the results obtained using the numerical method. In this case, the effect of dissipations has been included in the solution of the model, adding new informations to those already obtained.

It is possible to see in Figure 3.6 how, for increasing values of the Brinkman number, the average temperature profile changes radically, showing an absolute maximum close to the axis of the channel, where the velocity is higher, and hence the viscous dissipation term plays a major role as an energy term in the heat equation. Figure 3.6 refers to a non MHD case of a non symmetrically heated channel. It is interesting to see how the core of the temperature profile remains linear close to the mid plane at $y = 0$.

In the magnetic case, whose velocity and temperature components are shown in Figure 3.7 - 3.8, the dissipation terms influence broadly the flow pattern and the heat exchange. In Figure 3.7 are shown the average and oscillating amplitude components of dimensionless velocity, for $Br = 0.25$ and for increasing values of the Hartmann number $M = 0, 10, 20$. The GR ratio is equal to 100, while the dimensionless pulsation is $\Omega = 100$. In both cases one has $Pr = 1$. In 3.7(a) the average component of velocity shows a progressive suppression of the buoyant behavior for increasing Hartmann

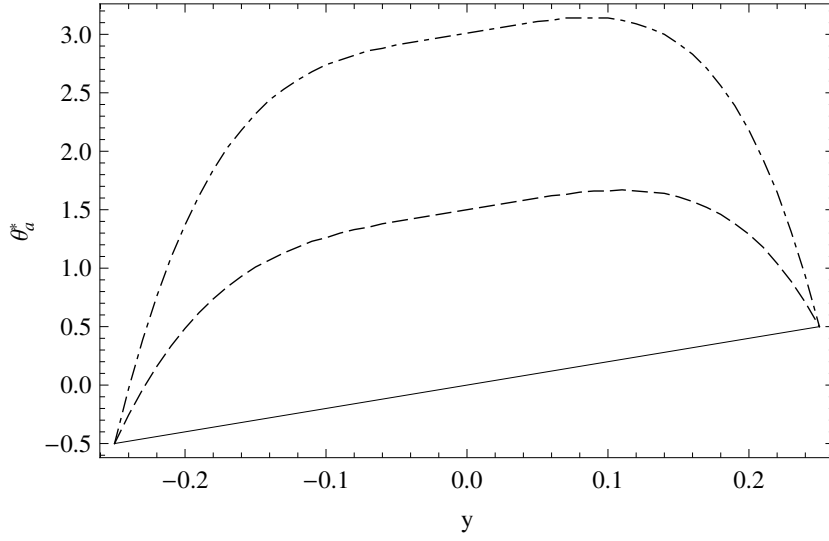


Figure 3.6 — Comparison of average temperature distributions across the channel for $M = 0$ and different values of Br . $Br = 0$ (continuous), $Br = 2$ (dashed), $Br = 4$ (dotted).

number. In 3.7(b) the amplitude of oscillating velocity is reduced as well by the presence of the magnetic field.

The effect of the Joule heating term is clearly visible in the profiles of the dimensionless temperature components. In Figure 3.8(a), the average temperature of the flow core increases rapidly for increasing values of M . Moreover, for the amplitude of the oscillating temperature shown in Figure 3.8(b) it is possible to observe an increased complexity of the profile, which now shows an inflection point with change of concavity whose location depends on the value of M .

3.4.3 Fanning friction factors and Nusselt numbers

The Fanning friction factors at the two walls can be defined as:

$$f_1 Re = \Re (f_{1,a}^* Re + GR f_{1,b}^* Re e^{in}), \quad (3.54)$$

and,

$$f_2 Re = \Re (f_{2,a}^* Re + GR f_{2,b}^* Re e^{in}), \quad (3.55)$$

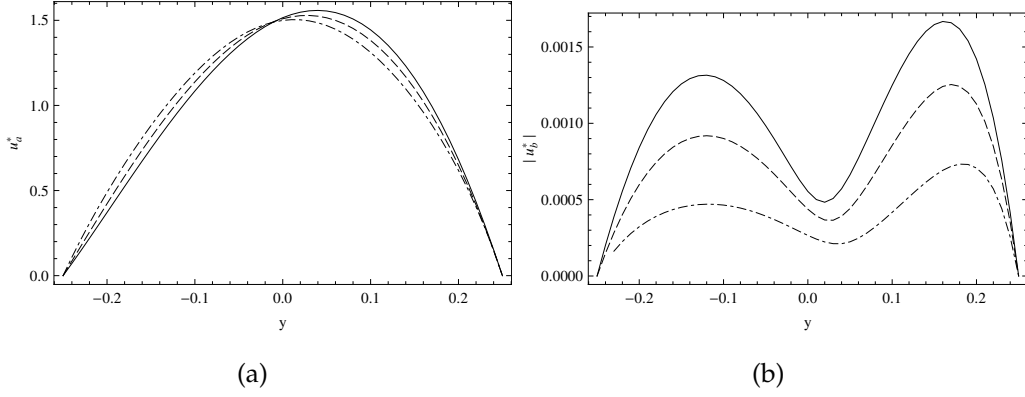


Figure 3.7 — Distribution of the average (a) and oscillating (b) velocity components across the channel for $Br = 0.25$ and different values of M . $M = 0$ (continuous), $M = 10$ (dashed), $M = 20$ (dotted).

where,

$$f_{1,a}^* Re = 2 \frac{\partial u_a^*}{\partial \xi} \Big|_{\xi=-1/4}, \quad f_{1,b}^* Re = 2 \frac{\partial u_b^*}{\partial \xi} \Big|_{\xi=-1/4}, \quad (3.56)$$

and,

$$f_{2,a}^* Re = -2 \frac{\partial u_a^*}{\partial \xi} \Big|_{\xi=1/4}, \quad f_{2,b}^* Re = -2 \frac{\partial u_b^*}{\partial \xi} \Big|_{\xi=1/4}, \quad (3.57)$$

so that the subscript 1 refers to the cold wall and the subscript 2 to the hot wall. Naturally the $f_1 Re$ and $f_2 Re$ are complex valued functions, and may be considered oscillating with the same frequency of the other functions, and can be decomposed in an average and an oscillating component as shown before. Following this definition it is possible to estimate the Fanning friction factors from the local derivatives of the dimensionless velocity at the two walls.

In Figure 3.9 the two average components of $f_1 Re$ and $f_2 Re$ are plotted versus GR and for $M = 0, 50, 100$. Let us note how for increasing values of M the friction factors increase accordingly, due to the steep velocity gradients which are typical of the Hartmann flow. For increasing values of GR , on the other hand, the values of $f_1 Re$ and $f_2 Re$ show opposite variations, due to the onset of flow reversal. It is interesting to note how for $M = 1$ flow reversal starts onseting for $GR \approx 140$, showing a negative $f_{1,a}^* Re$. With increasing M the onset of flow reversal drifts towards higher

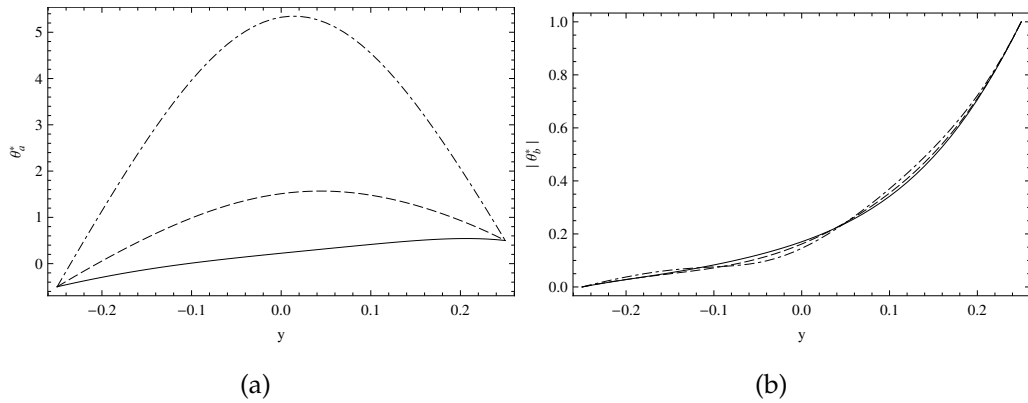


Figure 3.8 — Distribution of the average (a) and oscillating (b) temperature components across the channel for $Br = 0.25$ and different values of M . $M = 0$ (continuous), $M = 10$ (dashed), $M = 20$ (dotted).

values of GR .

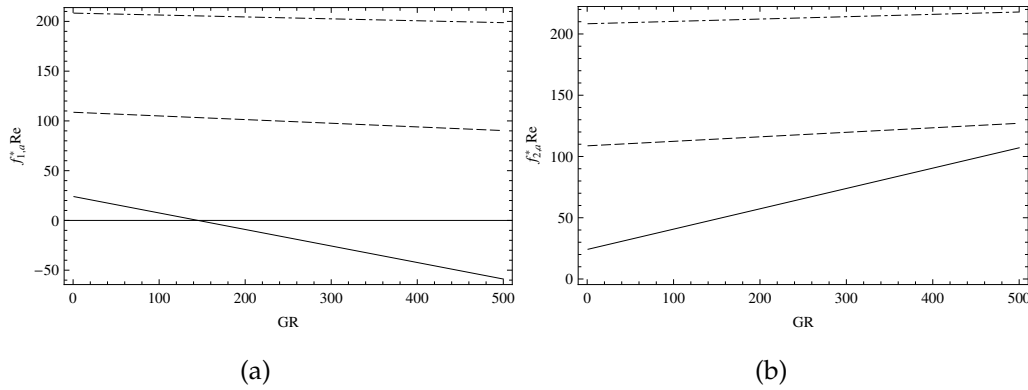


Figure 3.9 — Average component of the Fanning friction factor at the cold (a) and hot (b) walls plotted versus GR for different values of M . $M = 0$ (continuous), $M = 50$ (dashed), $M = 100$ (dotted).

While the average components of $f_1 Re$ and $f_2 Re$ depend on M and GR for a given θ_2 , the oscillating components are also functions of the Prandtl number and the dimensionless pulsation Ω .

In Figure 3.10 the values assumed at the cold wall by the amplitude of the oscillating component of the dimensionless Fanning friction factor $f_{1,b}^* Re$ are shown. Its values are plotted as functions of Ω for several values of the parameter M and for $Pr = 0.05$ or 5. In particular, Figure 3.10(a)

shows the values assumed by $f_{1,b}^* Re$ for $Pr = 0.05$ and $M = 0, 50, 100$, while Figure 3.10(b) shows the same values but for $Pr = 5$. It is evident how the increased value of Pr completely dampens the high frequency oscillations. It is interesting also to note how the presence of the magnetic field introduces dampening even at low frequency.

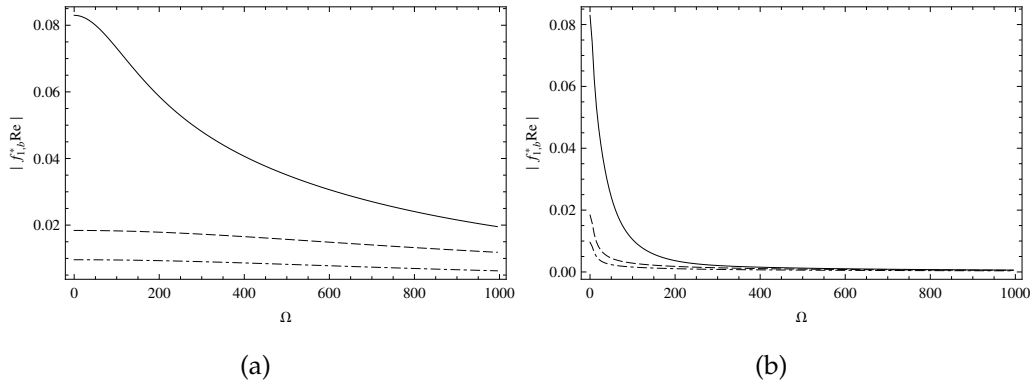


Figure 3.10 — Amplitude of the oscillating component of the Fanning friction factor at the cold wall plotted versus Ω for $Pr = 0.05$ (a) or $Pr = 5$ (b) and different values of M . $M = 0$ (continuous), $M = 50$ (dashed), $M = 100$ (dotted).

In Figure 3.11 the values assumed by $f_{1,b}^* Re$ as function of Ω are shown for several values of the parameter Pr and for $M = 0$ or 100. In particular, Figure 3.11(a) shows the values assumed by $f_{1,b}^* Re$ for $M = 0$ and $Pr = 0.05, 0.5, 5$, while Figure 3.11(b) shows the same values but for $M = 100$. The behavior shown before is hereby confirmed: while the increase of Pr results in a reduction of high frequency oscillations, the increase of M reduces such oscillation amplitude even at very low frequencies.

The amplitude of the oscillating component of the dimensionless Fanning friction factor at the hot wall, $f_{2,b}^* Re$ shows a completely different behavior, which is illustrated in Figure 3.12 and 3.13. The most characteristic feature is the presence of a local maximum whose existence and position are affected by the value of Pr and M . In Figure 3.12(a) it is possible to see that the function $|f_{2,b}^* Re|$ is not monotonic as $|f_{1,b}^* Re|$ for increasing values of Ω : in fact, for sufficiently high values of M the function shows an initial

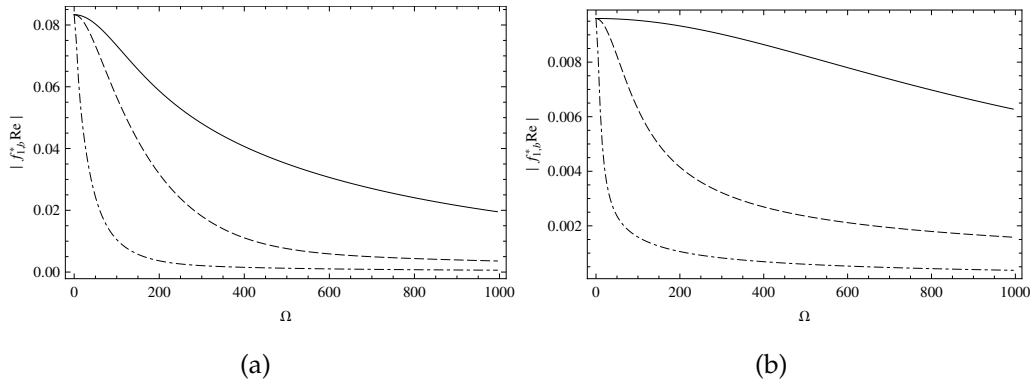


Figure 3.11 — Amplitude of the oscillating component of the Fanning friction factor at the cold wall plotted versus Ω for $M = 0$ (a) or $M = 100$ (b) and different values of Pr . $Pr = 0.05$ (continuous), $Pr = 0.5$ (dashed), $Pr = 5$ (dotted).

increase with increasing Ω . This behavior at $Pr = 0.05$ is an indication of the existence of a local maximum, which is clearly visible for $Pr = 5$ in Figure 3.12(b).

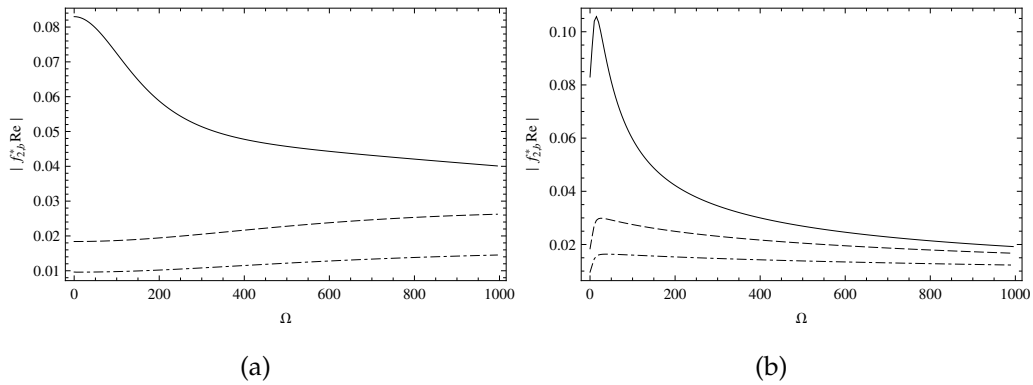


Figure 3.12 — Amplitude of the oscillating component of the Fanning friction factor at the hot wall plotted versus Ω for $Pr = 0.05$ (a) or $Pr = 5$ (b) and different values of M . $M = 0$ (continuous), $M = 50$ (dashed), $M = 100$ (dotted).

In Figure 3.13 how the local maximum of $|f_{2,b}^* Re|$ drifts on the dimensionless pulsation axis is clearly shown for various values of Pr and M . In Figure 3.13(a) it is possible to see the appearance of the local maximum for $Pr = 0.05, 0.5, 5$ in the non magnetic case at $M = 0$. For high Prandtl fluids the maximum is present, and its position drifts towards lower fre-

quencies for increasing values of Pr . For low Pr fluids the function is monotonically decreasing for increasing values of Ω . In Figure 3.13(b) the magnetic case at $M = 100$ is illustrated: the effect of the magnetic field is to reduce globally the value of $|f_{2,b}^* Re|$, even at low frequencies, and to make the maximum location shift towards higher frequencies. Interestingly, the maximum at $Pr = 0.05$ is present in the magnetic case, while it was not in the non magnetic case.

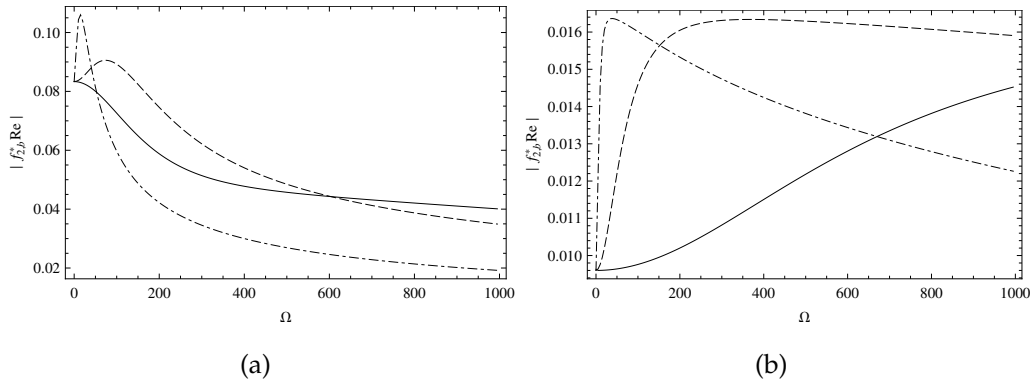


Figure 3.13 — Amplitude of the oscillating component of the Fanning friction factor at the hot wall plotted versus Ω for $M = 0$ (a) or $M = 100$ (b) and different values of Pr . $Pr = 0.05$ (continuous), $Pr = 0.5$ (dashed), $Pr = 5$ (dotted).

The dimensionless heat flux at a given position ξ' between the channel walls may be defined as:

$$Nu^*|_{\xi'} = \left. \frac{\partial \theta_a^*}{\partial \xi} \right|_{\xi'} + \left. \frac{\partial \theta_b^*}{\partial \xi} e^{i\eta} \right|_{\xi'} = Nu_a^*|_{\xi'} + Nu_b^*|_{\xi'}, \quad (3.58)$$

where the average value at $\Omega = 0$ is simply $Nu_a^* = 2$ in agreement with the classical steady state solution. In case of a steady periodic regime, neglecting the influence of the dissipative terms, the magnitude of the dimensionless heat flux Nu^* assumes the values shown in Figure 3.14. In particular, in Figure 3.14(a) the values of $|Nu^*|$ at $\xi = -0.25, -0.15, -0.05$ are shown as functions of Ω . In this part of the channel, the one close to the cold wall, the magnitude of Nu^* progressively decreases for increasing values of Ω , in agreement with the reduced penetration of the wall temperature oscillation at high frequencies.

In the part of the channel closer to the hot wall it can be noted that the magnitude of Nu^* shows a local maximum for a single value of the dimensionless pulsation Ω . In particular, as shown in Figure 3.14(a) for $\xi = 0.05, 0.15, 0.25$, the pulsation which maximizes the local dimensionless heat flux increases approaching the hot wall at $\xi = 0.25$.

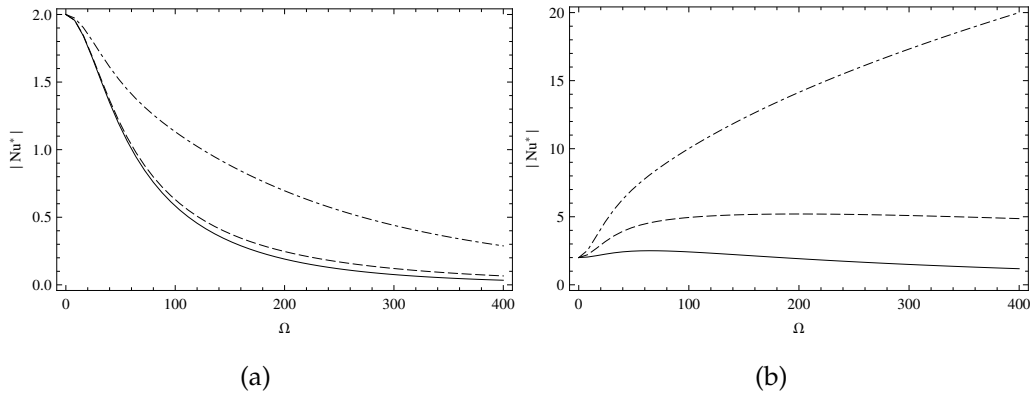


Figure 3.14 — Dimensionless heat flux Nu as a function of Ω at different locations inside the channel. Frame (a), $\xi = -0.25$ (continuous), $\xi = -0.15$ (dashed), $\xi = -0.05$ (dotted). Frame (b), $\xi = 0.05$ (continuous), $\xi = 0.15$ (dashed), $\xi = 0.25$ (dotted).

3.5 Closure

In this chapter were illustrated the effects of a transverse magnetic field on a steady periodic flow in a parallel vertical channel. The driving effect of the steady-periodic regime was the temperature of one of the two walls, which was assumed as varying sinusoidally with time. The Boussinesq approximation was considered as valid to model buoyancy. The average temperature across the channel section was used as a reference for the linearization of the state equation $\rho = \rho(T)$. The dimensionless local balance equations were solved in steady-periodic regime analytically, neglecting the dissipative terms in the energy equation, and numerically using a finite difference FORTRAN code.

The solution has shown that the external transverse magnetic field influences both the average velocity distribution and the amplitude of the

oscillating velocity component. In particular for increasing values of the Hartmann number, the average velocity profile changes from that of the classical non-magnetic case to the *Hartmann profile*, characterized by an almost uniform velocity at the core and steep velocity gradients at the walls. Moreover, for increasing values of the Hartmann number it was shown that the critical ratio of the Grashof over Reynolds number for the onset of flow reversal increases accordingly. Finally, with respect to the oscillating components of velocity, the effect of the transverse magnetic field is to progressively reduce their amplitudes, up to almost completely suppress them.

Chapter 4

MHD mixed convection flow in a vertical round pipe with transverse magnetic field. Steady periodic regime

Symbols used in the section

B	magnetic induction vector
<i>B</i>	magnitude of the magnetic induction vector
<i>c_p</i>	specific heat at constant pressure
<i>D</i>	pipe diameter
<i>f</i>	Fanning friction factor
g	gravity vector
<i>Gr</i>	Grashof's number
<i>GR</i>	ratio Gr/Re
<i>Ha</i>	Hartmann's number
j	current density vector
<i>k</i>	thermal conductivity
n	wall normal vector
<i>Nu</i>	Nusselt's number
<i>P</i>	pressure
<i>Pr</i>	Prandtl's number
\bar{q}_w	average heat flux
<i>R</i>	pipe radius
<i>Re</i>	Reynolds' number
<i>t</i>	time
ΔT	amplitude of wall temperature oscillation
<i>T</i>	temperature
<i>T_w</i>	wall temperature
<i>T_m</i>	average temperature
U	velocity vector
<i>V</i>	dimensionless electric potential
<i>W</i>	channel axial velocity
<i>w</i>	dimensionless velocity
<i>W_m</i>	average velocity
<i>w_m</i>	dimensionless average velocity
<i>W_R</i>	reference velocity, $-\partial P/\partial z \cdot D^2/\mu$
<i>x, y, z</i>	cartesian coordinates

Greek Symbols

α	thermal diffusivity
β	coefficient of thermal expansion
η	dimensionless time
θ	dimensionless temperature
μ	dynamic viscosity
ν	kinematic viscosity
ξ, ζ	dimensionless coordinates
ρ_m	density at $T = T_m$
σ	electrical conductivity
Σ	fluid domain boundary
ς	curvilinear abscissa on Σ
$\bar{\tau}_w$	average wall viscous stress
ϕ	electric potential
χ	aspect ratio
ω	angular frequency
Ω	dimensionless angular frequency

4.1 Introduction

In this section mixed convection in a vertical rectangular channel with an applied uniform horizontal magnetic field will be discussed. The steady-periodic regime will be analyzed, where the periodicity is induced by an uniform wall temperature which varies in time with a sinusoidal law. Local balance equations of momentum, energy and charge will be solved numerically for several values of the dimensionless parameters Ha and Pr . The temperature, velocity and potential field will be decomposed in an average and an oscillating component, and solved independently. The walls will be assumed as perfectly electrically insulating.

4.2 Governing equations

Let us consider the laminar flow of a Newtonian fluid in a vertical circular channel, with an uniform horizontal magnetic field of constant intensity B . The channel is assumed to be circular, with radius R . Under the hypothesis of fully developed flow, the velocity field is parallel, and the only non vanishing component of the velocity vector, $W(x, y, t)$, is parallel to the channel axis and independent of the vertical coordinate z . The thermal conductivity of the fluid k , the thermal diffusivity α and the dynamic viscosity μ will be assumed as constant. The system so defined is illustrated in Figure 4.1.

The complete set of governing equations is obtained assembling together the local balance equations for momentum, energy and electric potential.

An uniform temperature at the channel wall is assumed, varying in time with a sinusoidal law. Being the temperature uniform along the channel vertical direction, the heat flux in this direction can be considered equal to zero, therefore $\partial T/\partial z = 0$. Consequently:

$$T(x, \pm\sqrt{R^2 - x^2}, t) = T_w + \Delta T \cos(\omega t). \quad (4.1)$$

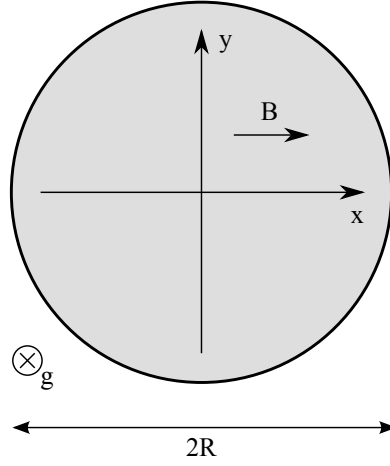


Figure 4.1 — A sketch of the channel.

The average temperature in the channel may be written as:

$$T_m = \frac{\omega}{2\pi^2 R^2} \int_0^{2\pi/\omega} dt \int_{-R}^R dx \int_{-\sqrt{R^2-x^2}}^{\sqrt{R^2-x^2}} dy T(x, y, t), \quad (4.2)$$

and is identically equal to the average wall temperature T_w . Being the thermal gradient along the channel axis equal to zero, T_m is independent of the axial coordinate z .

The no-slip boundary condition at the wall may be written as:

$$W(x, \pm\sqrt{R^2-x^2}, t) = 0, \quad (4.3)$$

and the average velocity across the channel section is:

$$W_m = \frac{1}{\pi R^2} \int_{-R}^R dx \int_{-\sqrt{R^2-x^2}}^{\sqrt{R^2-x^2}} dy W(x, y, t). \quad (4.4)$$

Let us assume the electric potential as independent of z , *i.e.* $\phi = \phi(x, y, t)$. To formulate the governing equation for the electric potential, let us write the law of conservation of charge and the generalized Ohm's equation as follows:

$$\nabla \cdot \mathbf{j} = 0, \quad \mathbf{j} = \sigma(-\nabla\phi + \mathbf{U} \times \mathbf{B}), \quad (4.5)$$

it is then possible to combine them in a more compact expression:

$$\nabla^2 \phi = \nabla \cdot (\mathbf{U} \times \mathbf{B}). \quad (4.6)$$

Under the hypothesis of parallel flow and transverse magnetic field oriented along the x axis, the previous equation can be further simplified as:

$$\frac{\partial^2 \phi}{\partial x^2} + \frac{\partial^2 \phi}{\partial y^2} = B \frac{\partial W}{\partial y}. \quad (4.7)$$

The boundary condition of perfectly insulating walls yields:

$$\mathbf{j} \cdot \mathbf{n} = 0, \quad \Rightarrow \quad \frac{\partial \phi}{\partial n} = 0, \quad (4.8)$$

where \mathbf{j} is the current density vector and \mathbf{n} is the direction vector normal to the channel wall.

Assuming the validity of the Oberbeck-Boussinesq approximation, the balance equation for momentum in its three components may be written as follows:

$$\frac{\partial P}{\partial x} = 0, \quad \frac{\partial P}{\partial y} = 0, \quad (4.9)$$

and, along z ,

$$\begin{aligned} \rho_m \frac{\partial W}{\partial t} = -\frac{\partial P}{\partial z} + \mu \left[\frac{\partial^2 W}{\partial x^2} + \frac{\partial^2 W}{\partial y^2} \right] + \\ + \rho_m g \beta (T - T_m) + \sigma \left[\frac{\partial \phi}{\partial y} B - B^2 W \right], \end{aligned} \quad (4.10)$$

where $P = p + \rho_m g z$ is the excess over the hydrostatic pressure, defined as the difference between the pressure and the hydrostatic pressure. As a consequence of (4.9), one has $P = P(z, t)$. Moreover, differentiating (4.10) with respect to z one obtains the identity $\partial^2 P / \partial z^2 = 0$. This shows that $\partial P / \partial z$ depends only on t . In the following it will be assumed that $\partial P / \partial z$ is independent of t as well.

Neglecting viscous dissipation and Joule heating, the balance equation for energy may be written as:

$$\rho_m c_p \frac{\partial T}{\partial t} = k \left[\frac{\partial^2 T}{\partial x^2} + \frac{\partial^2 T}{\partial y^2} \right]. \quad (4.11)$$

The system of governing equations is then assembled from (4.10), (4.11) and (4.7), which can be rewritten in terms of the following dimensionless groups:

$$\begin{aligned}
\xi &= \frac{x}{R}; & \zeta &= \frac{y}{R}; & w &= \frac{W}{W_R}; & w_m &= \frac{W_m}{W_R}; & \eta &= \omega t; \\
\Omega &= \frac{\omega D^2}{\nu}; & V &= \frac{\phi}{BDW_R}; & \theta &= \frac{T - T_m}{\Delta T}; & Re &= \frac{W_R D}{\nu}; \\
Pr &= \frac{\nu}{\alpha}; & Nu &= \frac{\bar{q}_w D}{k\Delta T}; & Gr &= \frac{g\beta\Delta T D^3}{\nu^2}; & GR &= \frac{Gr}{Re}; \\
Ha &= BD\sqrt{\frac{\sigma}{\mu}}; & W_R &= -\frac{dP}{dz} \frac{D^2}{\mu}; & D &= 2R; & \varsigma &= \frac{s}{R}.
\end{aligned} \tag{4.12}$$

where W_R and D are the reference velocity and the hydraulic diameter of the channel. The system of governing equation is then rewritten as:

$$\Omega \frac{\partial w}{\partial \eta} = 1 + 4 \left[\frac{\partial^2 w}{\partial \xi^2} + \frac{\partial^2 w}{\partial \zeta^2} \right] + GR\theta + Ha^2 \left[2 \frac{\partial V}{\partial \zeta} - w \right], \tag{4.13}$$

$$\Omega Pr \frac{\partial \theta}{\partial \eta} = 4 \left[\frac{\partial^2 \theta}{\partial \xi^2} + \frac{\partial^2 \theta}{\partial \zeta^2} \right], \tag{4.14}$$

$$\frac{\partial^2 V}{\partial \xi^2} + \frac{\partial^2 V}{\partial \zeta^2} = \frac{1}{2} \frac{\partial w}{\partial \zeta} \tag{4.15}$$

with the boundary conditions:

$$w(\xi, \pm\sqrt{1-\xi^2}, \eta) = 0, \tag{4.16}$$

$$\theta(\xi, \pm\sqrt{1-\xi^2}, \eta) = \cos(\eta), \tag{4.17}$$

$$\left. \frac{\partial V}{\partial n} \right|_{\Sigma} = 0 \tag{4.18}$$

where \mathbf{n} is the direction vector normal to the boundary Σ .

The average heat flux exchanged between the walls and the fluid may be written as:

$$\bar{q}_w = \frac{1}{S} \left[-k \int_S \frac{\partial T}{\partial n} ds \right]. \tag{4.19}$$

being,

$$\frac{\partial T}{\partial n} = \frac{\partial T}{\partial x} \cos \arctan \frac{y}{x} + \frac{\partial T}{\partial y} \sin \arctan \frac{y}{x}. \tag{4.20}$$

Using (4.12) it is possible to rewrite the heat flux in dimensionless form, obtaining an expression of the Nusselt number:

$$Nu = -\frac{1}{\pi} \int_{\Sigma} \frac{\partial \theta}{\partial n} d\zeta. \quad (4.21)$$

The Fanning friction factor can be derived from the average viscous stress at the walls:

$$f = 2 \frac{\bar{\tau}_w}{\rho_m W_R^2}, \quad (4.22)$$

being,

$$\bar{\tau}_w = \frac{1}{S} \left[\mu \int_S \frac{\partial W}{\partial n} ds \right], \quad (4.23)$$

in dimensionless form, using (4.12), it is possible to write:

$$f \text{ Re} = \frac{2}{\pi} \int_{\Sigma} \frac{\partial w}{\partial n} d\zeta. \quad (4.24)$$

4.3 Solution

Exploiting the linearity of the system, which follows from the assumption of negligible heat generation, it is possible to solve the system of partial differential equations (4.13) - (4.15) under the boundary conditions (4.16) - (4.18), decomposing the functions w , θ and V in the following components:

$$w(\xi, \zeta, \eta) = w_0(\xi, \zeta) + w_1(\xi, \zeta) \cos \eta + w_2(\xi, \zeta) \sin \eta, \quad (4.25)$$

$$\theta(\xi, \zeta, \eta) = \theta_0(\xi, \zeta) + \theta_1(\xi, \zeta) \cos \eta + \theta_2(\xi, \zeta) \sin \eta, \quad (4.26)$$

$$V(\xi, \zeta, \eta) = V_0(\xi, \zeta) + V_1(\xi, \zeta) \cos \eta + V_2(\xi, \zeta) \sin \eta, \quad (4.27)$$

so to obtain two new systems, which are linearly independent and stationary. The solution of the first provides the expressions of the average components of the dimensionless velocity, temperature and electric potential fields. The solution of the second represents the distribution of oscillating amplitude of the aforementioned dimensionless fields. The two systems may be written as:

For the average component:

$$\left\{ \begin{array}{l} 0 = 1 + 4 \left[\frac{\partial^2 w_0}{\partial \xi^2} + \frac{\partial^2 w_0}{\partial \zeta^2} \right] + GR \theta_0 + Ha^2 \left[\frac{\partial V_0}{\partial \zeta} - w_0 \right], \\ 0 = \frac{\partial^2 \theta_0}{\partial \xi^2} + \frac{\partial^2 \theta_0}{\partial \zeta^2}, \\ \frac{\partial^2 V_0}{\partial \xi^2} + \frac{\partial^2 V_0}{\partial \zeta^2} = \frac{1}{2} \frac{\partial w_0}{\partial \zeta}. \end{array} \right. \quad (4.28)$$

and for the oscillation amplitudes:

$$\left\{ \begin{array}{l} \Omega w_2 = 4 \left[\frac{\partial^2 w_1}{\partial \xi^2} + \frac{\partial^2 w_1}{\partial \zeta^2} \right] + GR \theta_1 + Ha^2 \left[\frac{\partial V_1}{\partial \zeta} - w_1 \right], \\ \Omega Pr \theta_2 = \frac{\partial^2 \theta_1}{\partial \xi^2} + \frac{\partial^2 \theta_1}{\partial \zeta^2}, \\ \frac{\partial^2 V_1}{\partial \xi^2} + \frac{\partial^2 V_1}{\partial \zeta^2} = \frac{1}{2} \frac{\partial w_1}{\partial \zeta}, \\ -\Omega w_1 = 4 \left[\frac{\partial^2 w_2}{\partial \xi^2} + \frac{\partial^2 w_2}{\partial \zeta^2} \right] + GR \theta_2 + Ha^2 \left[\frac{\partial V_2}{\partial \zeta} - w_2 \right], \\ -\Omega Pr \theta_1 = \frac{\partial^2 \theta_2}{\partial \xi^2} + \frac{\partial^2 \theta_2}{\partial \zeta^2}, \\ \frac{\partial^2 V_2}{\partial \xi^2} + \frac{\partial^2 V_2}{\partial \zeta^2} = \frac{1}{2} \frac{\partial w_2}{\partial \zeta}. \end{array} \right. \quad (4.29)$$

The boundary conditions for the first system are:

$$\left\{ \begin{array}{l} w_0(\xi, \pm\sqrt{1-\xi^2}, \eta) = 0 \\ \theta_0(\xi, \pm\sqrt{1-\xi^2}, \eta) = 0 \\ \left. \frac{\partial V_0}{\partial n} \right|_{\Sigma} = 0, \end{array} \right. \quad (4.30)$$

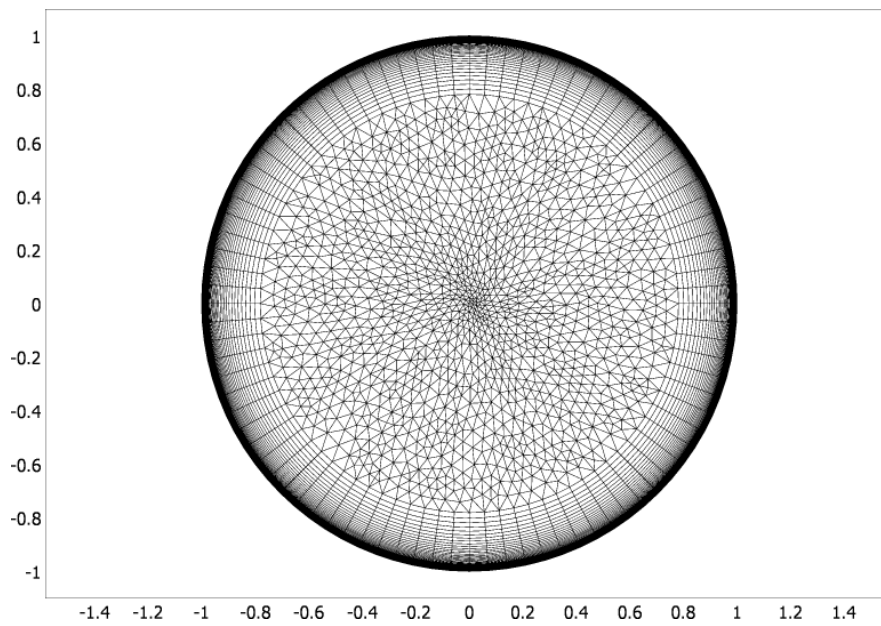
and, for the second:

$$\left\{ \begin{array}{l} w_1(\xi, \pm\sqrt{1-\xi^2}, \eta) = 0 \\ \theta_1(\xi, \pm\sqrt{1-\xi^2}, \eta) = 1 \\ \frac{\partial V_1}{\partial n} \Big|_{\Sigma} = 0, \\ w_2(\xi, \pm\sqrt{1-\xi^2}, \eta) = 0 \\ \theta_2(\xi, \pm\sqrt{1-\xi^2}, \eta) = 0 \\ \frac{\partial V_2}{\partial n} \Big|_{\Sigma} = 0, \end{array} \right. \quad (4.31)$$

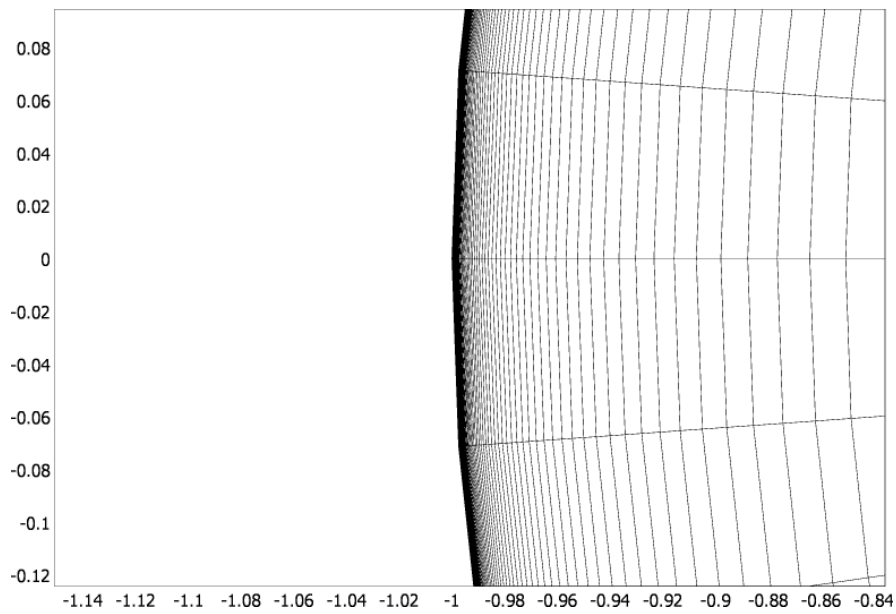
These two systems are solved numerically using the finite element code *COMSOL Multiphysics*. The discretization of the computational domain is shown in Figure 4.2(a). The mesh consists of $\cong 14000$ elements, divided in two groups. The core of the flow was discretized using an unstructured triangular meshing scheme, while the elements at the periphery of the section were modeled by extrusion of the boundary elements, starting from a thickness in direction normal to the wall of 10^{-7} , and progressively inflating the thickness of the elements following a geometrical progression with ratio 1.2. A structured mesh of 64 layers with quadrilateral elements was created, in order to accurately describe the thin Hartmann layer even for high values of the parameter Ha . A detailed view of the boundary layer elements is given in 4.2(b).

4.4 Results and Discussion

In the following sections the values assumed by the Fanning friction factor and by the Nusselt number will be reported for various flow configurations. As for (4.25)-(4.27), it is possible to decompose the functions f Re

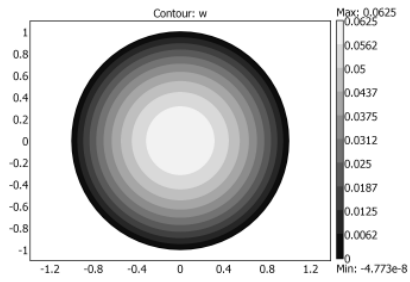


(a)

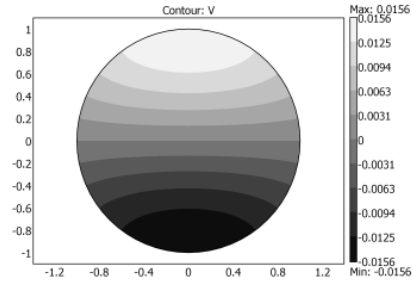


(b)

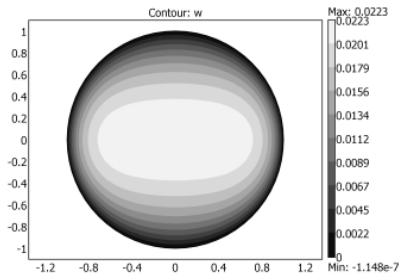
Figure 4.2 — The discretization of the computational domain: (a) An overview of the whole domain, showing the structured boundary layers and the unstructured core. (b) A detailed view of the structured mesh close to the wall. The thickness of the first element is 10^{-7} .



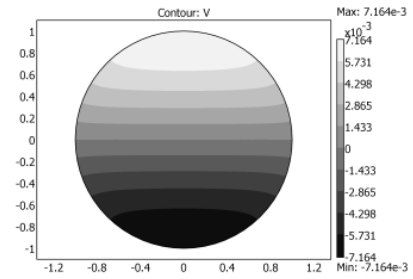
(a)



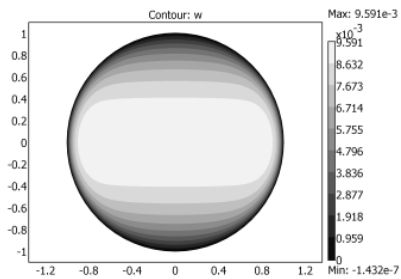
(b)



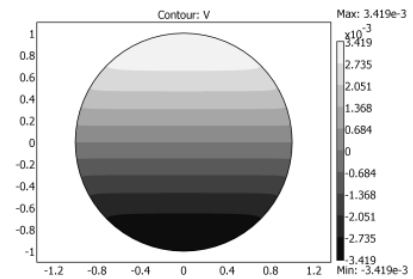
(c)



(d)



(e)



(f)

Figure 4.3 — Distributions of average dimensionless velocity (a) (c) (e) and electric potential (b) (d) (f), calculated for $Ha = 0$ (a,b), $Ha = 20$ (c,d), $Ha = 50$ (e,f) for steady state forced convection with transverse magnetic field.

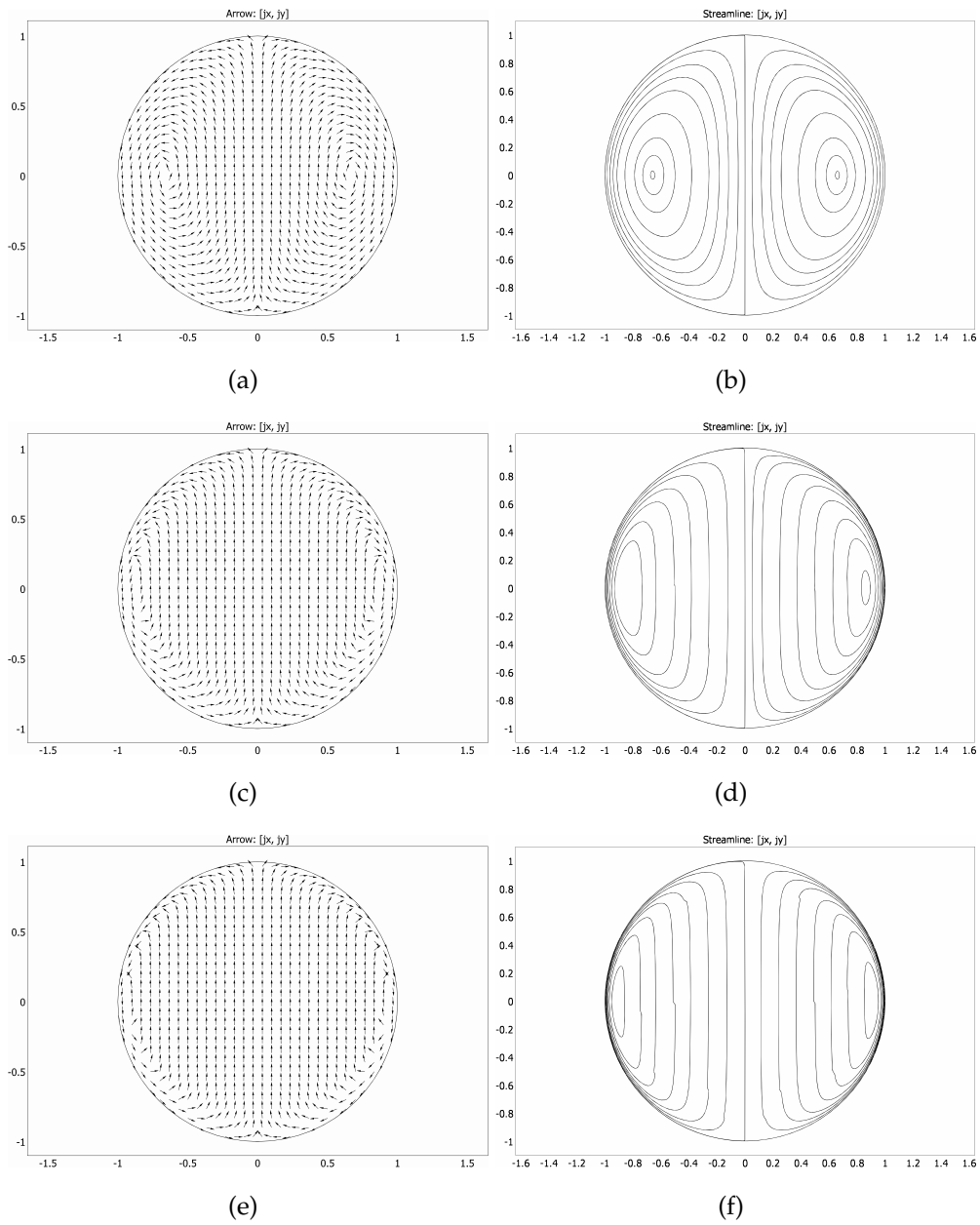


Figure 4.4 — Arrow and streamline plots of the current density vector \mathbf{J} across the pipe cross section, calculated for $Ha = 10$ (a,b), $Ha = 50$ (c,d), $Ha = 100$ (e,f) for steady state forced convection with transverse magnetic field.

and Nu in their average and oscillating components. The decomposition is as follows:

$$f Re = f_0 Re + f_1 Re \cos \eta + f_2 Re \sin \eta \quad (4.32)$$

$$Nu = Nu_0 + Nu_1 \cos \eta + Nu_2 \sin \eta \quad (4.33)$$

where the subscript 0 indicates the average components and the subscripts 1 and 2 indicate the oscillation amplitudes of the two oscillating components (respectively oscillating with cosine and sine). Moreover, it is possible to define the resulting oscillation amplitudes as:

$$|f Re| = \sqrt{(f_1 Re)^2 + (f_2 Re)^2}, \quad (4.34)$$

$$|Nu| = \sqrt{(Nu_1)^2 + (Nu_2)^2}.$$

4.4.1 Forced stationary convection with MHD effects

This first case has been chosen to demonstrate the consistency of the model and to show some preliminary results in steady state laminar flow. In the literature the analytical solution for the Fanning friction factor for laminar flow in a smooth round pipe is well known, being for this particular case:

$$f Re = 16. \quad (4.35)$$

In Table 4.1 the values of $f Re$ in case of forced convection ($GR = 0$) with a transverse external magnetic field are reported as they were obtained numerically in the present work for several values of the Hartmann number. It should be noted that the numerical results for $f Re$ were rescaled with respect to w_m , in order to obtain results which are ready for comparison with further applications, by evaluating numerically the integral in (4.4).

In Figure 4.3, contour plots of dimensionless velocity, temperature and electric potential are reported for $Ha = 0$, $Ha = 20$ and $Ha = 50$. In particular, in Figure 4.3(c) the distribution of velocity w across the pipe section is represented for $Ha = 20$. It is evident that the velocity gradient

Table 4.1 — Values of $f Re$ as a function of Ha in stationary forced convection, $GR = 0$, $\Omega = 0$.

Ha	$f Re w_m$	Ha	$f Re w_m$	Ha	$f Re w_m$
0	16.00	50	68.13	5000	4289.47
1	16.08	100	126.48	10000	6712.76
5	17.90	500	578.27	50000	12271.36
10	22.30	1000	1107.59	100000	13897.92

is greater at the walls normal to the direction of the magnetic field. This effect is more relevant for increasing values of Ha . Moreover, in Figure 4.3(d) the distribution of electric potential V is plotted. It can be noted that V depends mainly on ζ , which is the direction orthogonal to the magnetic field. This implies that the electric and the magnetic field are orthogonal in almost all the duct cross section.

In Figure 4.4, arrow and streamline plots of the current density vector \mathbf{J} across the pipe cross section are reported for $Ha = 10$, $Ha = 50$ and $Ha = 100$. It is evident, as reported in Figures 4.4(b), 4.4(d) and 4.4(f), that the current lines are closed inside the section, with no current crossing the insulated walls. Moreover, it can be noted that for increasing values of the Hartmann number, the closure of the current lines is segregated to a narrow region near the *Hartmann walls*, where consequently the effect of the Lorentz force is more intense, and large velocity gradients appear.

4.4.2 Steady periodic mixed convection with MHD effects

In case of mixed convection, so when $GR \neq 0$, it is possible to study the effects of an oscillating wall temperature on the Fanning friction factor and on the Nusselt number. In Table 4.2 the resulting oscillation amplitudes of $f Re$ and Nu are reported as functions of Ω , Pr and Ha .

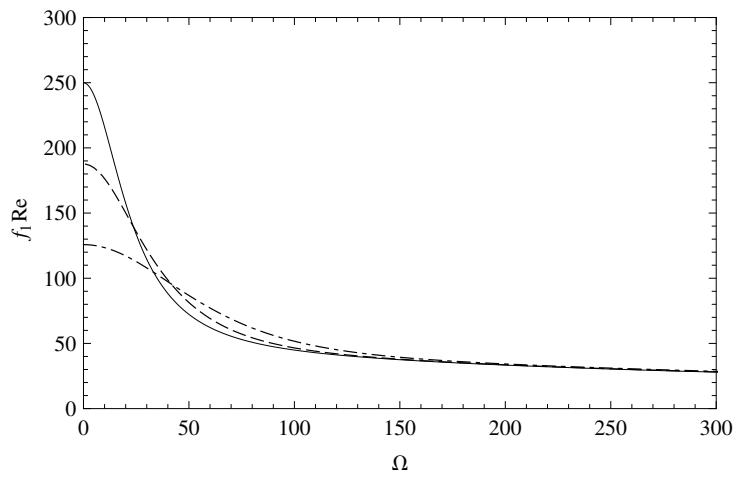
The numerical results prove that $|Nu|$ increases monotonically with Ω , while $|f Re|$ decreases with Ω . Moreover, in Figures 4.5 and 4.6, the values of $f_{1,2} Re$ and $Nu_{1,2}$ are plotted versus Ω for several values of Ha . It may be noted that $f_2 Re$ shows some absolute maxima whose position is affected

Table 4.2 — Values of the oscillating amplitudes of $f Re$ and Nu as a function of Ω . Results obtained in mixed convection regime, with $Pr = 0.05$ and $GR = 500$.

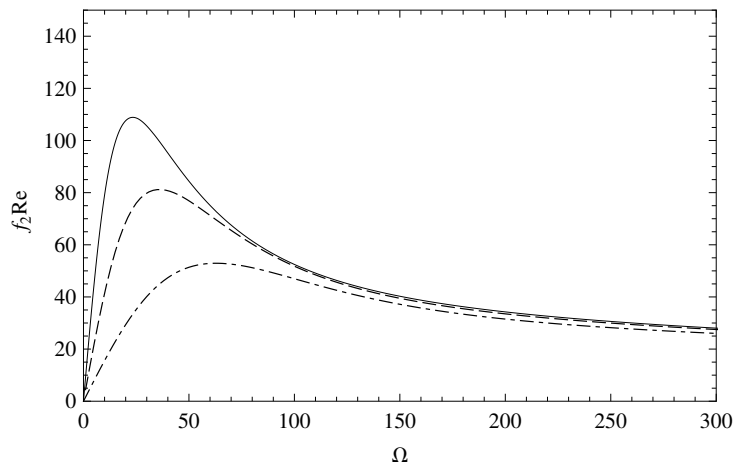
$Pr = 0.05$					
Ω	$ Nu $	$Ha = 0$	$Ha = 1$	$Ha = 10$	$Ha = 100$
		$ f Re $	$ f Re $	$ f Re $	$ f Re $
0	0.00	250.00	246.18	125.90	16.61
1	0.05	249.77	245.97	125.89	16.61
5	0.25	244.50	241.01	125.57	16.60
10	0.50	230.00	227.31	124.59	16.58
50	2.32	111.16	111.29	100.97	16.03
100	3.96	69.11	69.13	69.90	14.97
500	9.32	30.91	30.90	30.54	12.12
1000	13.46	21.85	21.84	21.75	11.15
5000	30.92	9.77	9.77	9.77	8.12

Table 4.3 — Values of the oscillating amplitudes of $f Re$ and Nu as a function of Ω . Results obtained in mixed convection regime, with $Pr = 1$ and $GR = 500$.

$Pr = 1$					
Ω	$ Nu $	$Ha = 0$	$Ha = 1$	$Ha = 10$	$Ha = 100$
		$ f Re $	$ f Re $	$ f Re $	$ f Re $
0	0.00	250.00	246.18	125.90	16.61
1	0.99	246.30	242.56	124.53	16.51
5	3.96	188.46	186.05	103.71	15.00
10	5.84	124.85	123.96	82.29	13.60
50	13.46	46.43	46.43	44.55	11.44
100	19.31	33.34	33.33	32.38	10.62
500	44.02	14.91	14.91	14.85	8.41
1000	62.54	10.54	10.54	10.53	7.26
5000	140.70	4.71	4.71	4.71	4.35



(a)



(b)

Figure 4.5 — Behavior of $f_1 Re$ (a) and $f_2 Re$ (b) as functions of Ω obtained for $Ha = 0$ (continuous) $Ha = 5$ (dashed) and $Ha = 10$ (dotted) in mixed convection regime, with $GR = 500$ and $Pr = 0.05$.

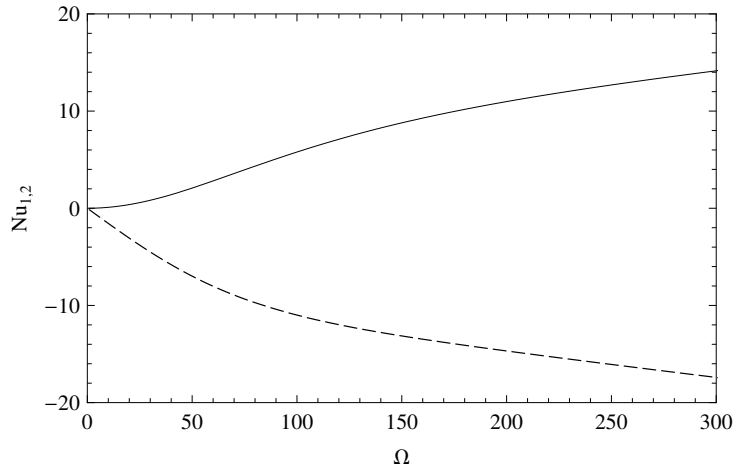


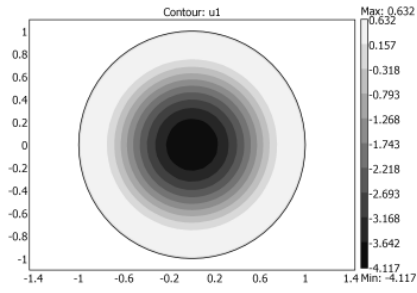
Figure 4.6 — Behavior of Nu_1 (continuous) and Nu_2 (dashed) as functions of Ω in mixed convection regime with $Pr = 0.05$.

by Ha .

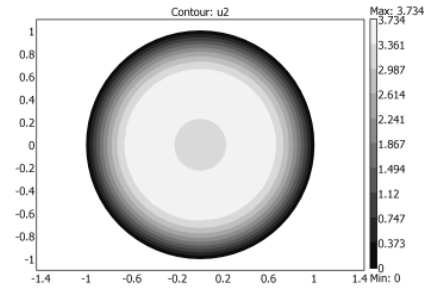
In Figure 4.7 the distributions of oscillation amplitudes for the components of velocity w_1 and w_2 (Figures 4.7(a) and 4.7(b)), of temperature θ_1 and θ_2 (Figures 4.7(c) and 4.7(d)), and of electric potential (Figures 4.7(e) and 4.7(f)) are plotted for $Ha = 0$. Analogous plots are reported in Figure 4.8 and 4.9 for $Ha = 20$ and $Ha = 50$, respectively. The results show that w_1 has both positive and negative values for small values of Ha , while for higher values of Ha it is always positive. On the contrary, w_2 is always positive, but its maximum value across the sections decreases with increasing values of Ha .

4.5 Closure

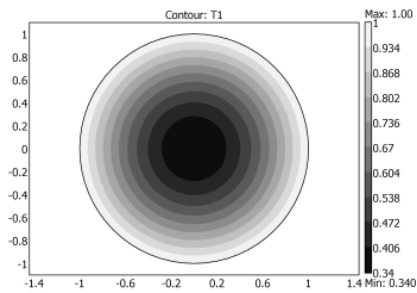
In the present section the effects of a transverse magnetic field on a steady periodic flow in a vertical circular pipe were studied, for several values of the Hartmann and Prandtl numbers. The driving effect of the steady-periodic regime was the wall temperature, which was assumed uniform across the pipe wall and varying sinusoidally with time. The Boussinesq approximation was assumed to model buoyancy. The average tempera-



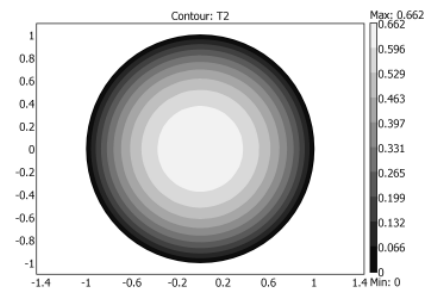
(a)



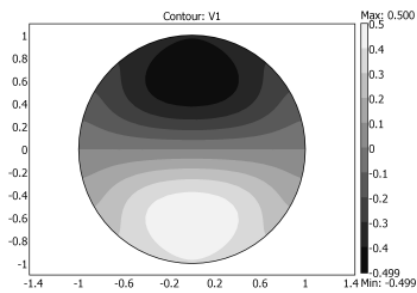
(b)



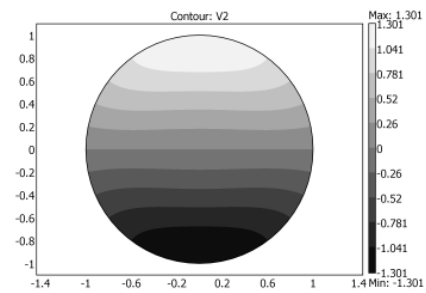
(c)



(d)



(e)



(f)

Figure 4.7 — Distributions of oscillation amplitudes for dimensionless velocity (a) (b), temperature (c) (d) and electric potential (e) (f), calculated for $Ha = 0$ in mixed convection regime, with $GR = 500$, $Pr = 0.05$ and $\Omega = 100$.

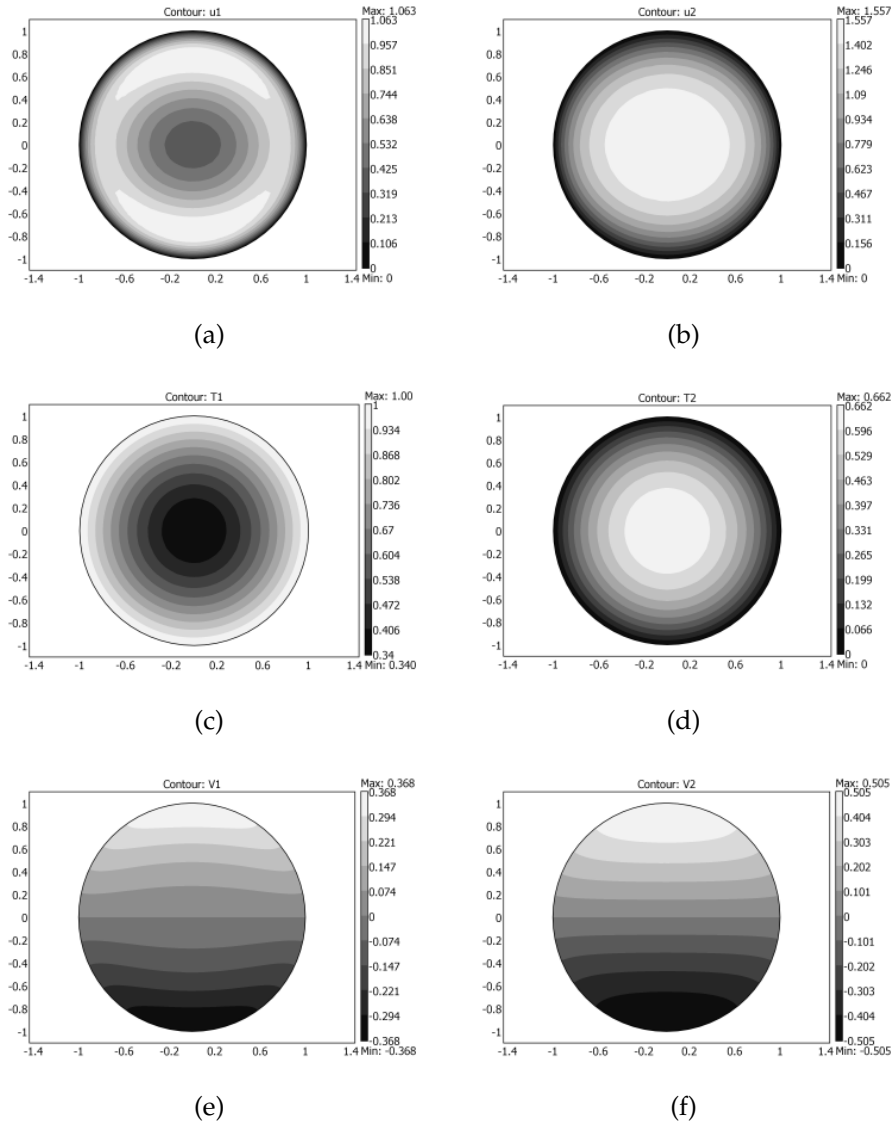
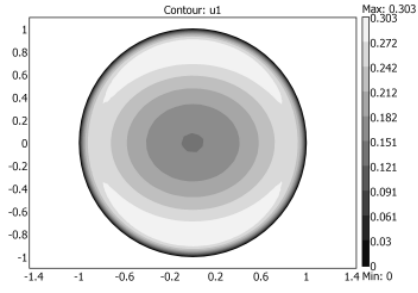
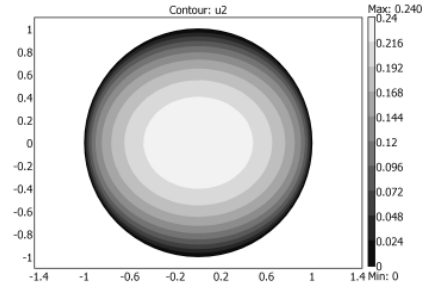


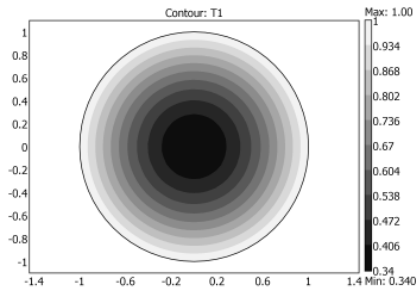
Figure 4.8 — Distributions of oscillation amplitudes for dimensionless velocity (a) (b), temperature (c) (d) and electric potential (e) (f), calculated for $Ha = 20$ in mixed convection regime, with $GR = 500$, $Pr = 0.05$ and $\Omega = 100$.



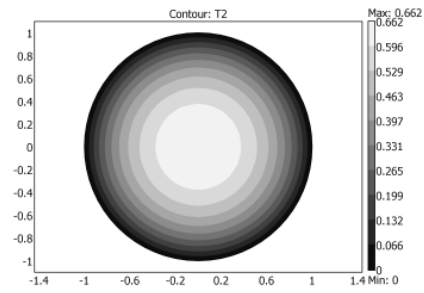
(a)



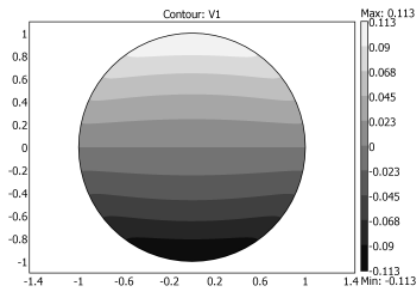
(b)



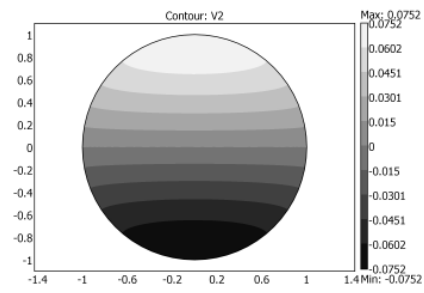
(c)



(d)



(e)



(f)

Figure 4.9 — Distributions of oscillation amplitudes for dimensionless velocity (a) (b), temperature (c) (d) and electric potential (e) (f), calculated for $Ha = 50$ in mixed convection regime, with $GR = 500$, $Pr = 0.05$ and $\Omega = 100$.

ture across the pipe cross section was used as a reference for the linearization of the equation of state $\rho = \rho(T)$. The dimensionless local balance equations were solved numerically in steady-periodic regime using the commercial software *COMSOL Multiphysics*.

In the particular case of forced convection, the numerical results shown in the present work were compared with those available in the literature, obtaining a perfect agreement in the determination of the Fanning friction factor for the circular pipe configuration.

Moreover, in case of steady periodic mixed convection with MHD effects, the amplitudes of the oscillating components of the Fanning friction factor and of the Nusselt number were computed as functions of Ω and Ha . It was shown that the value of $|Nu|$ increases for increasing values of Ω and that $f_1 Re$ is an always decreasing function of the same Ω . Finally, it was proved the existence of a local maximum of $f_2 Re$ for each value of Ha , whose position on the Ω axis shifts towards higher values for increasing values of Ha .

Chapter 5

MHD mixed convection flow in a vertical rectangular duct with transverse magnetic field. Steady periodic regime

Symbols used in the section

B	magnetic induction vector
<i>B</i>	magnitude of the magnetic induction vector
<i>c_p</i>	specific heat at constant pressure
<i>D</i>	hydraulic diameter, $4L\chi/(1+\chi)$
<i>f</i>	Fanning friction factor
g	gravity vector
<i>Gr</i>	Grashof's number
<i>GR</i>	ratio Gr/Re
<i>Ha</i>	Hartmann's number
j	current density vector
<i>k</i>	thermal conductivity
<i>L</i>	channel characteristic dimension
n	wall normal vector
<i>Nu</i>	Nusselt's number
<i>P</i>	pressure
<i>Pr</i>	Prandtl's number
\bar{q}_w	average heat flux
<i>Re</i>	Reynolds' number
<i>t</i>	time
ΔT	amplitude of wall temperature oscillation
<i>T</i>	temperature
<i>T_w</i>	wall temperature
<i>T_m</i>	average temperature
U	velocity vector
<i>V</i>	dimensionless electric potential
<i>W</i>	channel axial velocity
<i>w</i>	dimensionless velocity
<i>W_m</i>	average velocity
<i>w_m</i>	dimensionless average velocity
<i>W_R</i>	reference velocity, $-\partial P/\partial z \cdot D^2/\mu$
<i>x, y, z</i>	cartesian coordinates

Greek Symbols

α	thermal diffusivity
β	coefficient of thermal expansion
η	dimensionless time
θ	dimensionless temperature
μ	dynamic viscosity
ν	kinematic viscosity
ξ, ζ	dimensionless coordinates
ρ_m	density at $T = T_m$
σ	electrical conductivity
$\bar{\tau}_w$	average wall viscous stress
ϕ	electric potential
χ	aspect ratio
ω	angular frequency
Ω	dimensionless angular frequency

5.1 Introduction

In this section mixed convection in a vertical rectangular channel with an applied uniform horizontal magnetic field will be discussed. The steady-periodic regime will be analyzed, where the periodicity is induced by an uniform wall temperature which varies in time with a sinusoidal law. Local balance equations of momentum, energy and charge will be solved numerically using the channel aspect ratio as the main parameter. The temperature, velocity and potential field will be decomposed in an average and an oscillating component, and solved independently. The walls will be assumed as perfectly insulating.

5.2 Governing equations

Let us consider the laminar flow of a Newtonian fluid in a vertical rectangular channel, with an uniform horizontal magnetic field of constant intensity B . The channel is assumed to be rectangular, with a size $2L \times 2\chi L$, so that χ is the channel aspect ratio. Under the hypothesis of fully developed flow, the velocity field is parallel, and the only non vanishing component of the velocity vector, $W(x, y, t)$, is parallel to the channel axis and independent on the vertical coordinate z . The thermal conductivity of the fluid k , the thermal diffusivity α and the dynamic viscosity μ will be assumed as constant. The system so defined is illustrated in Figure 5.1.

The complete set of governing equations is obtained assembling together the local balance equations for momentum, energy and electric potential.

An uniform temperature at the channel walls is assumed, varying in time with a sinusoidal law. Being the temperature uniform along the channel vertical direction, the heat flux in this direction can be considered equal to zero, therefore $\partial T / \partial z = 0$. Consequently:

$$T(\pm L, y, t) = T(x, \pm\chi L, t) = T_w + \Delta T \cos(\omega t). \quad (5.1)$$

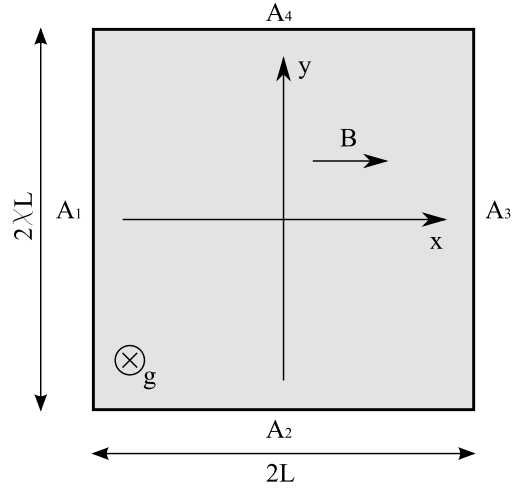


Figure 5.1 — A sketch of the channel.

The average temperature in the channel may be written as:

$$T_m = \frac{\omega}{8\pi\chi L^2} \int_0^{2\pi/\omega} dt \int_{-L}^L dx \int_{-\chi L}^{\chi L} dy T(x, y, t), \quad (5.2)$$

and is identically equal to the average wall temperature T_w . Being the thermal gradient along the channel axis equal to zero, T_m is independent of the height z .

The no-slip boundary condition at the wall may be written as:

$$W(\pm L, y, t) = W(x, \pm\chi L, t) = 0, \quad (5.3)$$

and the average velocity across the channel section is:

$$W_m = \frac{1}{4\chi L^2} \int_{-L}^L dx \int_{-\chi L}^{\chi L} dy W(x, y, t). \quad (5.4)$$

Let us assume the electric potential independent of z , *i.e.* $\phi = \phi(x, y, t)$. To formulate the governing equation for the electric potential, let us write the law of conservation of charge and the generalized Ohm's equation as follows:

$$\nabla \cdot \mathbf{j} = 0, \quad \mathbf{j} = \sigma(-\nabla\phi + \mathbf{U} \times \mathbf{B}), \quad (5.5)$$

it is then possible to combine them in a more compact expression:

$$\nabla^2 \phi = \nabla \cdot (\mathbf{U} \times \mathbf{B}). \quad (5.6)$$

Under the hypothesis of parallel flow and transverse magnetic field oriented along the x axis, the previous equation can be further simplified as:

$$\frac{\partial^2 \phi}{\partial x^2} + \frac{\partial^2 \phi}{\partial y^2} = B \frac{\partial W}{\partial y}. \quad (5.7)$$

The boundary condition of perfectly insulating walls yields:

$$\mathbf{j} \cdot \mathbf{n} = 0, \quad \Rightarrow \quad \frac{\partial \phi}{\partial n} = 0, \quad (5.8)$$

where \mathbf{j} is the current density vector and \mathbf{n} is the direction vector normal to the channel wall.

Assuming the validity of the Oberbeck-Boussinesq approximation, the balance equation for momentum may be written in its three components as follows:

$$\frac{\partial P}{\partial x} = 0, \quad \frac{\partial P}{\partial y} = 0, \quad (5.9)$$

and, along z ,

$$\begin{aligned} \rho_m \frac{\partial W}{\partial t} = -\frac{\partial P}{\partial z} + \mu \left[\frac{\partial^2 W}{\partial x^2} + \frac{\partial^2 W}{\partial y^2} \right] + \\ + \rho_m g \beta (T - T_m) + \sigma \left[\frac{\partial \phi}{\partial y} B - B^2 W \right], \end{aligned} \quad (5.10)$$

where $P = p + \rho_m g z$ is the excess over the hydrostatic pressure, defined as the difference between the pressure and the hydrostatic pressure. As a consequence of (5.9), is $P = P(z, t)$. Moreover, differentiating the (5.10) with respect to z one obtains the identity $\partial^2 P / \partial z^2 = 0$. This shows that $\partial P / \partial z$ depends only on t . In the following it will be assumed that $\partial P / \partial z$ is independent from t as well.

Neglecting viscous dissipation and Joule heating, the balance equation for energy may be written as:

$$\rho_m c_p \frac{\partial T}{\partial t} = k \left[\frac{\partial^2 T}{\partial x^2} + \frac{\partial^2 T}{\partial y^2} \right]. \quad (5.11)$$

The system of governing equations is then assembled from (5.10), (5.11) and (5.7), which can be rewritten in terms of the following dimensionless groups:

$$\begin{aligned}
\xi &= \frac{x}{L}; & \zeta &= \frac{y}{\chi L}; & w &= \frac{W}{W_R}; & w_m &= \frac{W_m}{W_R}; & \eta &= \omega t; \\
\Omega &= \frac{\omega D^2}{\nu}; & V &= \frac{\phi}{BDW_R}; & \theta &= \frac{T - T_m}{\Delta T}; & Re &= \frac{W_R D}{\nu}; \\
Pr &= \frac{\nu}{\alpha}; & Nu &= \frac{\bar{q}_w D}{k\Delta T}; & Gr &= \frac{g\beta\Delta T D^3}{\nu^2}; & GR &= \frac{Gr}{Re}; \\
Ha &= BD\sqrt{\frac{\sigma}{\mu}}.
\end{aligned} \tag{5.12}$$

where W_R and D are the reference velocity and the hydraulic diameter of the channel. The system of governing equation is then rewritten as:

$$\begin{aligned}
\Omega \frac{\partial w}{\partial \eta} &= 1 + \frac{16\chi^2}{(1+\chi)^2} \left[\frac{\partial^2 w}{\partial \xi^2} + \frac{1}{\chi^2} \frac{\partial^2 w}{\partial \zeta^2} \right] + \\
&+ GR\theta + Ha^2 \left[\frac{4}{(1+\chi)} \frac{\partial V}{\partial \zeta} - w \right], \tag{5.13}
\end{aligned}$$

$$\Omega Pr \frac{\partial \theta}{\partial \eta} = \frac{16\chi^2}{(1+\chi)^2} \left[\frac{\partial^2 \theta}{\partial \xi^2} + \frac{1}{\chi^2} \frac{\partial^2 \theta}{\partial \zeta^2} \right], \tag{5.14}$$

$$\frac{\partial^2 V}{\partial \xi^2} + \frac{1}{\chi^2} \frac{\partial^2 V}{\partial \zeta^2} = \frac{1+\chi}{4\chi^2} \frac{\partial w}{\partial \zeta}. \tag{5.15}$$

with the boundary conditions:

$$w(\pm 1, \zeta, \eta) = w(\xi, \pm 1, \eta) = 0, \tag{5.16}$$

$$\theta(\pm 1, \zeta, \eta) = \theta(\xi, \pm 1, \eta) = \cos(\eta), \tag{5.17}$$

$$\left. \frac{\partial V}{\partial \xi} \right|_{\xi=\pm 1} = 0; \quad \left. \frac{\partial V}{\partial \zeta} \right|_{\zeta=\pm 1} = 0. \tag{5.18}$$

The average heat flux exchanged between the walls and the fluid may be written as:

$$\begin{aligned}
\bar{q}_w &= \frac{1}{A_T} \left[\left(-k \int_{A_1} \frac{\partial T}{\partial x} dA + k \int_{A_3} \frac{\partial T}{\partial x} dA \right) + \right. \\
&+ \left. \left(-k \int_{A_2} \frac{\partial T}{\partial y} dA + k \int_{A_4} \frac{\partial T}{\partial y} dA \right) \right], \tag{5.19}
\end{aligned}$$

being $A_1 - A_4$ the wall areas and A_T their sum. Using (5.12) it is possible to rewrite the heat flux in dimensionless form, obtaining an expression of the Nusselt number:

$$Nu = \frac{\chi^2}{(1 + \chi)^2} \left[\left(\int_{-1}^1 \frac{\partial \theta}{\partial \xi} d\zeta \Big|_{\xi=1} - \int_{-1}^1 \frac{\partial \theta}{\partial \xi} d\zeta \Big|_{\xi=-1} \right) + \frac{1}{\chi^2} \left(\int_{-1}^1 \frac{\partial \theta}{\partial \zeta} d\xi \Big|_{\zeta=1} - \int_{-1}^1 \frac{\partial \theta}{\partial \zeta} d\xi \Big|_{\zeta=-1} \right) \right]. \quad (5.20)$$

The Fanning friction factor can be derived from the average viscous stress at the walls:

$$f = 2 \frac{\bar{\tau}_w}{\rho_m W_R^2}, \quad (5.21)$$

being,

$$\bar{\tau}_w = \frac{1}{A_T} \left[\left(\mu \int_{A_1} \frac{\partial W}{\partial x} dA - \mu \int_{A_3} \frac{\partial W}{\partial x} dA \right) + \left(\mu \int_{A_2} \frac{\partial W}{\partial y} dA - \mu \int_{A_4} \frac{\partial W}{\partial y} dA \right) \right], \quad (5.22)$$

in dimensionless form, using (5.12), it is possible to write:

$$f Re = 2 \frac{\chi^2}{(1 + \chi)^2} \left[\left(\int_{-1}^1 \frac{\partial w}{\partial \xi} d\zeta \Big|_{\xi=-1} - \int_{-1}^1 \frac{\partial w}{\partial \xi} d\zeta \Big|_{\xi=1} \right) + \frac{1}{\chi^2} \left(\int_{-1}^1 \frac{\partial w}{\partial \zeta} d\xi \Big|_{\zeta=-1} - \int_{-1}^1 \frac{\partial w}{\partial \zeta} d\xi \Big|_{\zeta=1} \right) \right]. \quad (5.23)$$

5.3 Solution

Exploiting the linearity of the system, which follows the assumption of negligible heat generation, it is possible to solve the system made of (5.13) - (5.15) under the boundary conditions (5.16) - (5.18), decomposing the functions w , θ and V in the following components:

$$w(\xi, \zeta, \eta) = w_0(\xi, \zeta) + w_1(\xi, \zeta) \cos \eta + w_2(\xi, \zeta) \sin \eta, \quad (5.24)$$

$$\theta(\xi, \zeta, \eta) = \theta_0(\xi, \zeta) + \theta_1(\xi, \zeta) \cos \eta + \theta_2(\xi, \zeta) \sin \eta, \quad (5.25)$$

$$V(\xi, \zeta, \eta) = V_0(\xi, \zeta) + V_1(\xi, \zeta) \cos \eta + V_2(\xi, \zeta) \sin \eta, \quad (5.26)$$

so to obtain two new systems, which are linearly independent and stationary. The solution of the first provides the expressions of the average components of the dimensionless velocity, temperature and electric potential fields. The solution of the second represents the distribution of oscillating amplitude of the aforementioned dimensionless fields. The two systems may be written as:

For the average component:

$$\left\{ \begin{array}{l} 0 = 1 + \frac{16\chi^2}{(1+\chi)^2} \left[\frac{\partial^2 w_0}{\partial \xi^2} + \frac{1}{\chi^2} \frac{\partial^2 w_0}{\partial \zeta^2} \right] + \\ + GR \theta_0 + Ha^2 \left[\frac{4}{(1+\chi)} \frac{\partial V_0}{\partial \zeta} - w_0 \right], \\ 0 = \frac{\partial^2 \theta_0}{\partial \xi^2} + \frac{1}{\chi^2} \frac{\partial^2 \theta_0}{\partial \zeta^2}, \\ \frac{\partial^2 V_0}{\partial \xi^2} + \frac{1}{\chi^2} \frac{\partial^2 V_0}{\partial \zeta^2} = \frac{1+\chi}{4\chi^2} \frac{\partial w_0}{\partial \zeta}. \end{array} \right. \quad (5.27)$$

and for the oscillation amplitudes:

$$\left\{ \begin{array}{l}
 \Omega w_2 = \frac{16\chi^2}{(1+\chi)^2} \left[\frac{\partial^2 w_1}{\partial \xi^2} + \frac{1}{\chi^2} \frac{\partial^2 w_1}{\partial \zeta^2} \right] + \\
 + GR\theta_1 + Ha^2 \left[\frac{4}{(1+\chi)} \frac{\partial V_1}{\partial \zeta} - w_1 \right], \\
 \Omega Pr\theta_2 = \frac{16\chi^2}{(1+\chi)^2} \left[\frac{\partial^2 \theta_1}{\partial \xi^2} + \frac{1}{\chi^2} \frac{\partial^2 \theta_1}{\partial \zeta^2} \right], \\
 \frac{\partial^2 V_1}{\partial \xi^2} + \frac{1}{\chi^2} \frac{\partial^2 V_1}{\partial \zeta^2} = \frac{1+\chi}{4\chi^2} \frac{\partial w_1}{\partial \zeta}, \\
 -\Omega w_1 = \frac{16\chi^2}{(1+\chi)^2} \left[\frac{\partial^2 w_2}{\partial \xi^2} + \frac{1}{\chi^2} \frac{\partial^2 w_2}{\partial \zeta^2} \right] + \\
 + GR\theta_2 + Ha^2 \left[\frac{4}{(1+\chi)} \frac{\partial V_2}{\partial \zeta} - w_2 \right], \\
 -\Omega Pr\theta_1 = \frac{16\chi^2}{(1+\chi)^2} \left[\frac{\partial^2 \theta_2}{\partial \xi^2} + \frac{1}{\chi^2} \frac{\partial^2 \theta_2}{\partial \zeta^2} \right], \\
 \frac{\partial^2 V_2}{\partial \xi^2} + \frac{1}{\chi^2} \frac{\partial^2 V_2}{\partial \zeta^2} = \frac{1+\chi}{4\chi^2} \frac{\partial w_2}{\partial \zeta}.
 \end{array} \right. \quad (5.28)$$

The boundary conditions for the first system are:

$$\left\{ \begin{array}{l}
 w_0(\pm 1, \zeta) = w_0(\xi, \pm 1) = 0 \\
 \theta_0(\pm 1, \zeta) = \theta_0(\xi, \pm 1) = 0 \\
 \left. \frac{\partial V_0}{\partial \xi} \right|_{\xi=\pm 1} = 0; \quad \left. \frac{\partial V_0}{\partial \zeta} \right|_{\zeta=\pm 1} = 0,
 \end{array} \right. \quad (5.29)$$

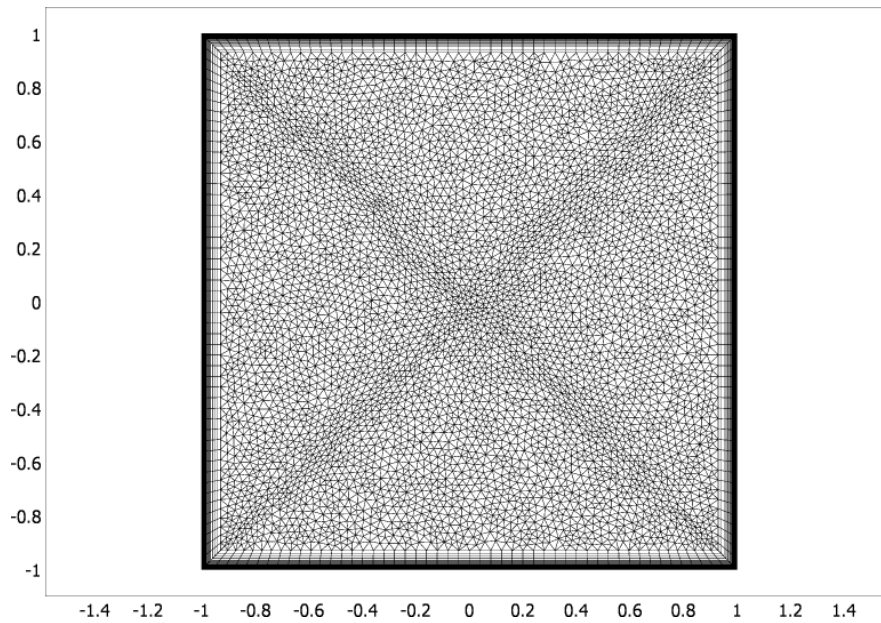
and, for the second:

$$\left\{ \begin{array}{l} w_1(\pm 1, \zeta) = w_1(\xi, \pm 1) = 0 \\ \theta_1(\pm 1, \zeta) = \theta_1(\xi, \pm 1) = 1 \\ \frac{\partial V_1}{\partial \xi} \Big|_{\xi=\pm 1} = 0; \quad \frac{\partial V_1}{\partial \zeta} \Big|_{\zeta=\pm 1} = 0, \\ w_2(\pm 1, \zeta) = w_2(\xi, \pm 1) = 0 \\ \theta_2(\pm 1, \zeta) = \theta_2(\xi, \pm 1) = 0 \\ \frac{\partial V_2}{\partial \xi} \Big|_{\xi=\pm 1} = 0; \quad \frac{\partial V_2}{\partial \zeta} \Big|_{\zeta=\pm 1} = 0, \end{array} \right. \quad (5.30)$$

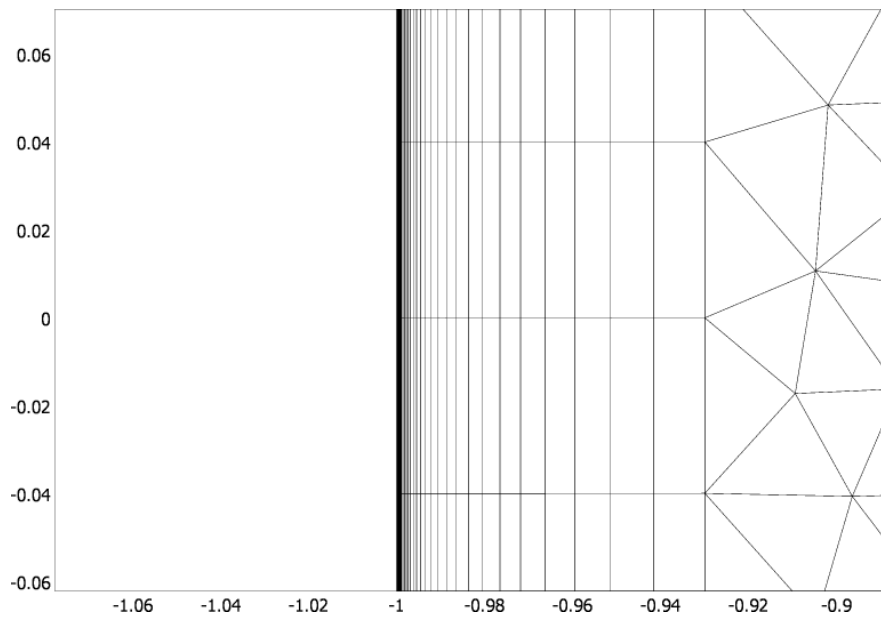
These two systems are solved numerically using the finite element code *COMSOL Multiphysics*. The discretization of the computational domain is shown in Figure 5.2(a). The mesh consists of $\cong 24000$ elements, divided in two groups. The core of the flow was discretized using a free triangular meshing scheme, while the elements at the periphery of the section were modeled by inflation of the boundary elements, starting from a thickness in direction normal to the wall of 10^{-7} , and progressively inflating the thickness of the elements following a geometrical progression with ratio 1.1. Totally 128 layers of quadrilateral elements were created, in order to accurately describe the thin Hartmann layers even for high values of the parameter Ha . A detailed view of the boundary layer elements is given in 5.2(b).

5.4 Results and Discussion

In the following sections the values assumed by the Fanning friction factor and by the Nusselt number will be reported for various flow configurations. As for (5.24)-(5.26), it is as well possible to decompose the functions



(a)



(b)

Figure 5.2 — The discretization of the computational domain: (a) An overview of the whole domain, showing the structured boundary layers and the unstructured core. (b) A detailed view of the structured mesh close to the wall. The thickness of the first element is 10^{-7} .

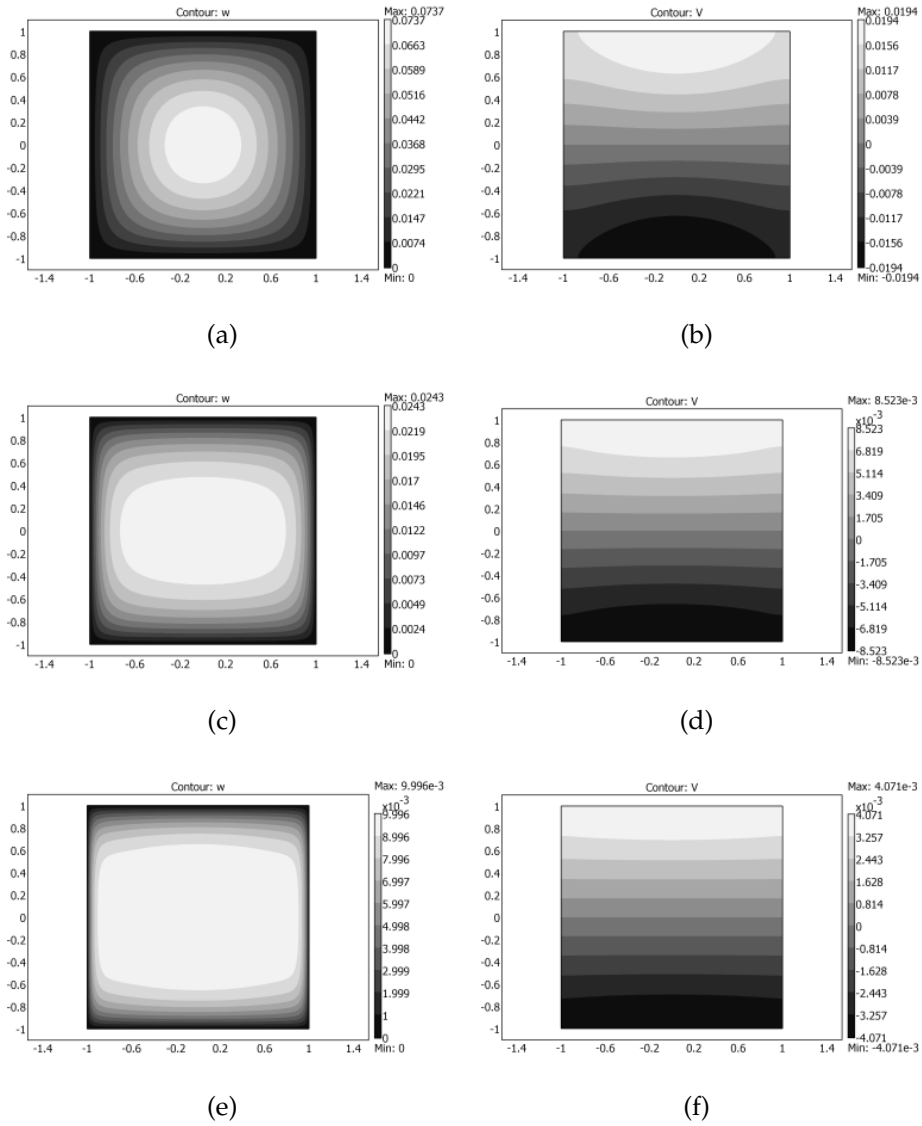


Figure 5.3 — Distributions of average dimensionless velocity (a) (c) (e) and electric potential (b) (d) (f), calculated for $Ha = 0$ (a,b), $Ha = 20$ (c,d), $Ha = 50$ (e,f) in a square channel ($\chi = 1$) for a steady state forced convection with transverse magnetic field.

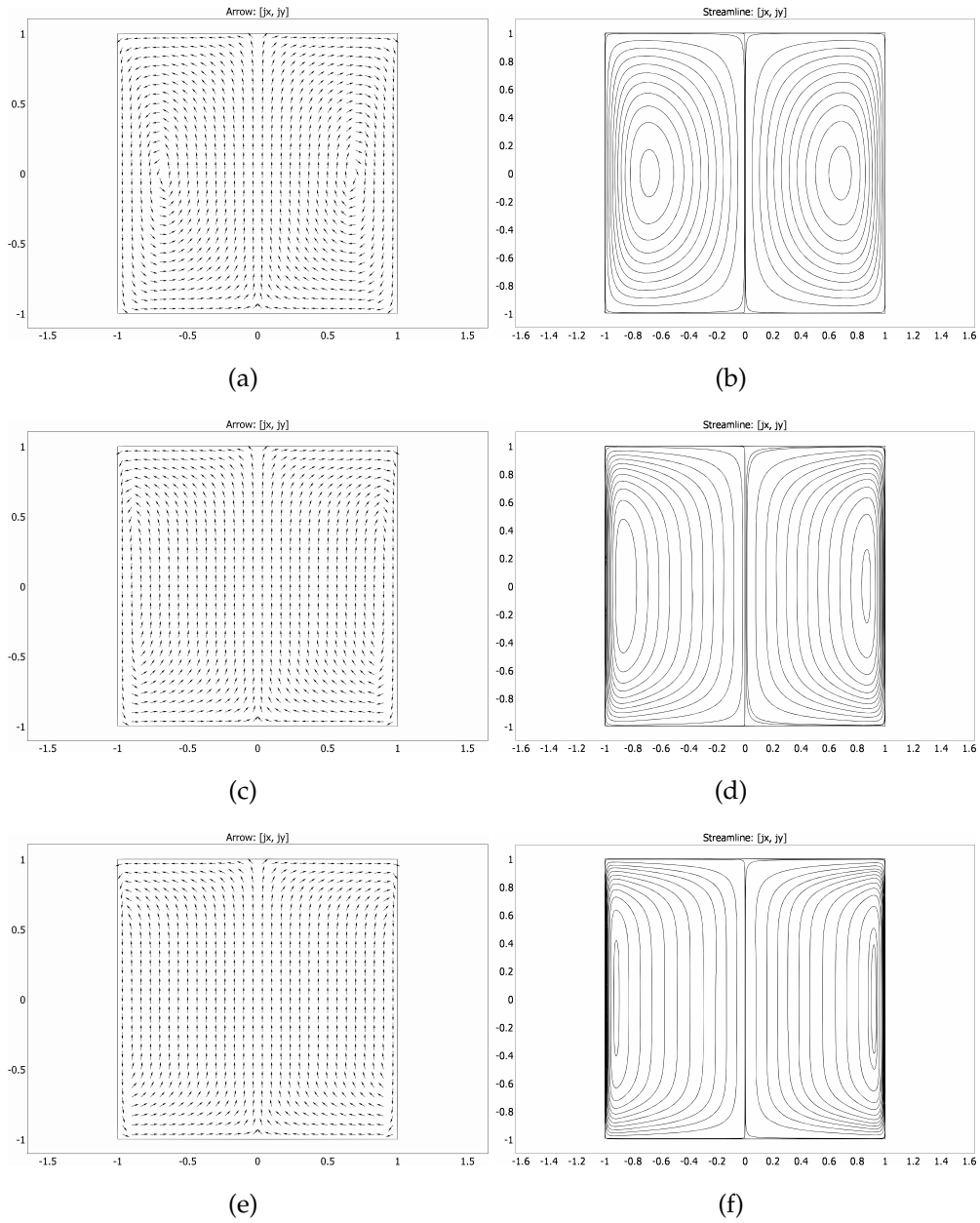


Figure 5.4 — Arrow and streamline plots of the current density vector \mathbf{J} across the duct cross section, calculated for $Ha = 10$ (a,b), $Ha = 50$ (c,d), $Ha = 100$ (e,f) for steady state forced convection with transverse magnetic field.

$f Re$ and Nu in their average and oscillating components. The decomposition is as follows:

$$f Re = f_0 Re + f_1 Re \cos \eta + f_2 Re \sin \eta \quad (5.31)$$

$$Nu = Nu_0 + Nu_1 \cos \eta + Nu_2 \sin \eta \quad (5.32)$$

where the subscript 0 indicates the average components and the subscripts 1 and 2 indicate the oscillation amplitudes of the two oscillating components (respectively oscillating with cosine and sine). Moreover, it is possible to define the resulting oscillation amplitudes as:

$$|f Re| = \sqrt{(f_1 Re)^2 + (f_2 Re)^2}, \quad (5.33)$$

$$|Nu| = \sqrt{(Nu_1)^2 + (Nu_2)^2}.$$

5.4.1 Forced stationary convection without MHD effects

This validation case has been chosen to demonstrate the consistency of the model. In literature an analytical solution (11) is available for this particular configuration which yields exact values of the Fanning friction factor for various aspect ratios of the channel. In Table 5.1 the values of $f Re$ obtained numerically in the present work are reported and compared with those available in the literature.

It should be noted that, to correctly compare the values, the numerical results for $f Re$ were rescaled with respect to w_m , for ease of comparison with the data obtained from the analytical solution. This allows to compare directly the results, at the price of evaluating numerically the integral in (5.4).

After the scaling, it is possible to note that the two series of results are in excellent agreement, with a maximum relative error always smaller than 0.01%. This allows to assume that the model is properly set up and that its results may be extended to more complex configurations.

Table 5.1 — Comparison between the factor $f Re_m$ obtained in the present work and the analytical solution available in literature (11). Stationary forced convection, $GR = 0$, $\Omega = 0$.

χ	reference	calculated	ε
	$f Re w_m$	$f Re w_m$	
1	14.22708	14.22713	0.00%
2	15.54806	15.54814	0.00%
3	17.08967	17.08983	0.00%
4	18.23278	18.23305	0.00%
5	19.07050	19.07092	0.00%
6	19.70220	19.70281	0.00%
7	20.19310	20.19392	0.00%
8	20.58464	20.58570	0.01%
9	20.90385	20.90515	0.01%
10	21.16888	21.17043	0.01%

5.4.2 Forced stationary convection with MHD effects

In Table 5.2 the results obtained for $f Re w_m$ in case of forced convection ($GR = 0$) with a transverse external magnetic field are reported. The results are obtained for several values of the channel aspect ratio.

The results show that the influence of the magnetic field is relevant when the channel has $\chi > 1$, *i.e.* when the distance between the walls orthogonal to the field (the *Hartmann walls*) is smaller than the distance between the walls parallel to the field. In that case, the viscous stress is influenced both by the geometry of the conduit and by the interaction between the flow and the magnetic field, which modifies the wall velocity profile by increasing the local wall velocity gradient. At the same time it is possible to note how, without magnetic field, there exists a symmetry $\chi \rightarrow 1/\chi$ with respect to the values of $f Re w_m$.

In Figure 5.3, contour plots of dimensionless velocity, temperature and electric potential are reported for $Ha = 0$, $Ha = 20$ and $Ha = 50$ in the case of a square channel with $\chi = 1$. In particular, in Figure 5.3(c) the distribu-

Table 5.2 — Values of $f Re$ as a function of Ha in stationary forced convection, $GR = 0$, $\Omega = 0$.

	$\chi = 1/5$	$\chi = 1/2$	$\chi = 1$	$\chi = 2$	$\chi = 5$
Ha	$f Rew_m$	$f Rew_m$	$f Rew_m$	$f Rew_m$	$f Rew_m$
0	19.07	15.55	14.23	15.55	19.07
1	19.08	15.59	14.31	15.65	19.17
10	20.17	19.06	20.37	23.32	27.47
100	51.46	84.19	116.11	147.32	178.03

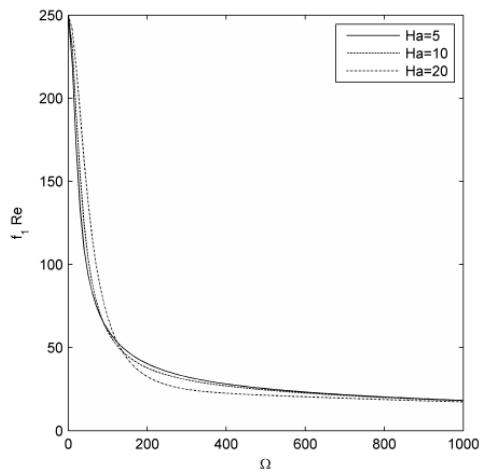
tion of velocity w across the channel section is represented for $Ha = 20$. It is evident that the velocity gradient is greater at the walls normal to the direction of the magnetic field. This effect is more relevant for increasing values of Ha . Moreover, in Figure 5.3(d) the distribution of electric potential V is plotted. It can be noted that V depends mainly on ζ , which is the direction orthogonal to the magnetic field. This implies that the electric and the magnetic field are orthogonal in almost all the duct cross section.

In Figure 5.4, arrow and streamline plots of the current density vector \mathbf{J} across the duct cross section are reported for $Ha = 10$, $Ha = 50$ and $Ha = 100$. It is evident, as reported in Figures 5.4(b), 5.4(d) and 5.4(f), that the current lines close completely inside the section, with no escape of current through the insulated walls. Moreover, it can be noted that for increasing values of the Hartmann number, the closure of the current lines is segregated to a narrow region near the *Hartmann walls*, where consequently the effect of the Lorentz force is more intense, and large velocity gradients appear.

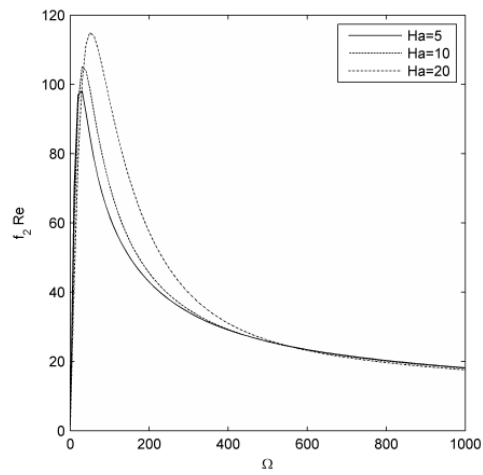
5.4.3 Steady periodic mixed convection with MHD effects

In case of mixed convection, so when $GR \neq 0$, it is possible to study the effects of an oscillating wall temperature on the Fanning friction factor and on the Nusselt number. In Table 5.3 the resulting oscillation amplitudes of $f Re$ and Nu as functions of Ω , Pr and Ha are reported.

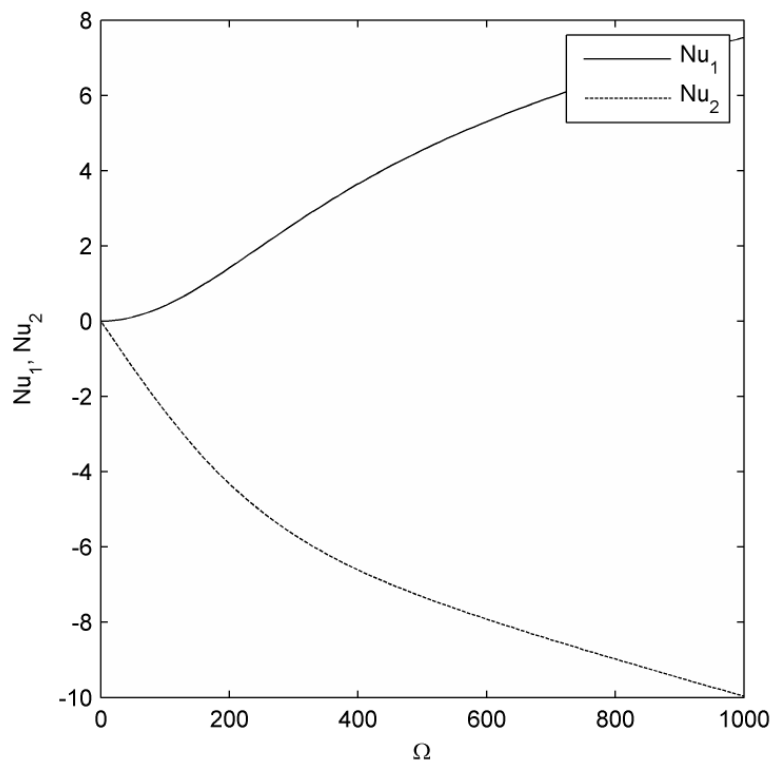
The numerical results prove that $|Nu|$ increases monotonically with Ω ,



(a)



(b)



(c)

Figure 5.5 — Behavior of $f_1 Re$, $f_2 Re$, Nu_1 and Nu_2 as functions of Ω obtained for $Ha = 5, 10, 20$. Results apply to a square channel $\chi = 1$ in mixed convection regime, with $GR = 500$, $Pr = 0.05$.

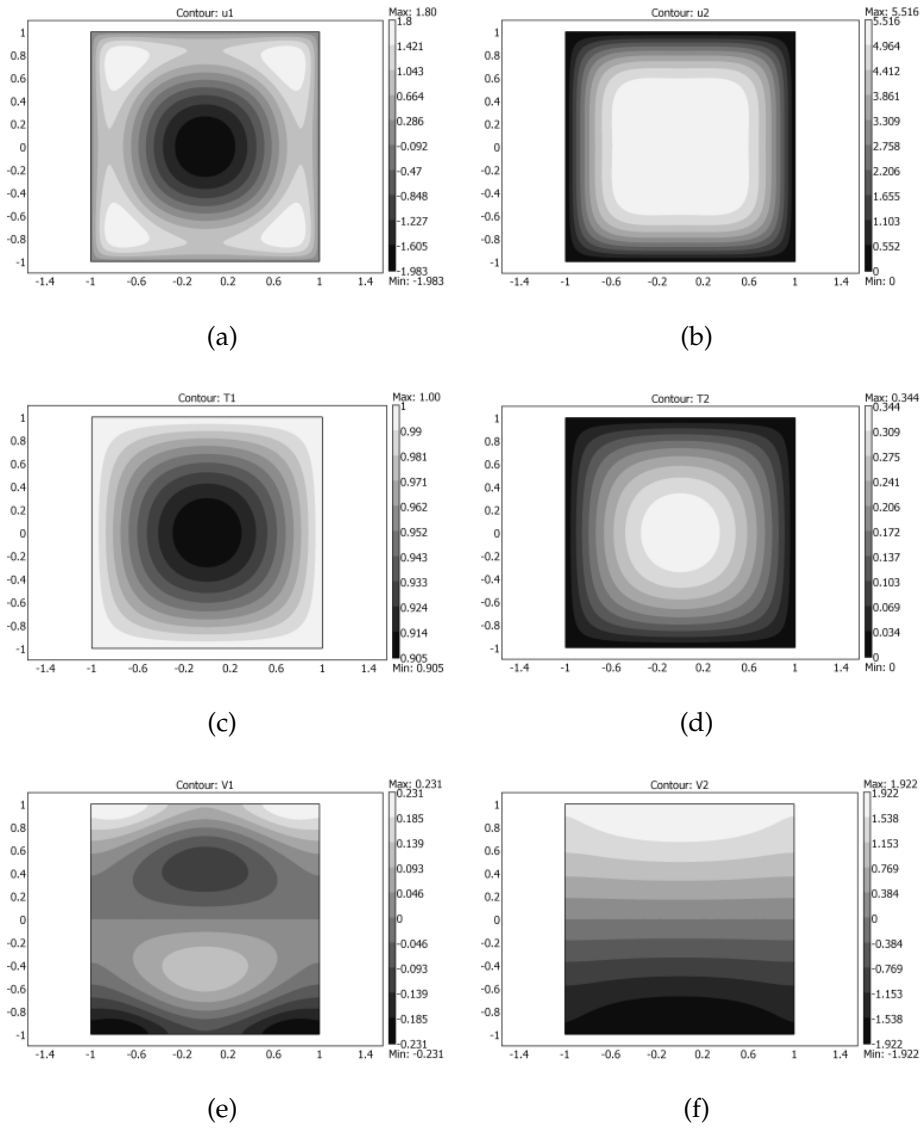


Figure 5.6 — Distributions of oscillation amplitudes for dimensionless velocity (a) (b), temperature (c) (d) and electric potential (e) (f), calculated for $Ha = 0$ and $\chi = 1$, in mixed convection regime, with $GR = 500$, $Pr = 0.05$ and $\Omega = 100$.

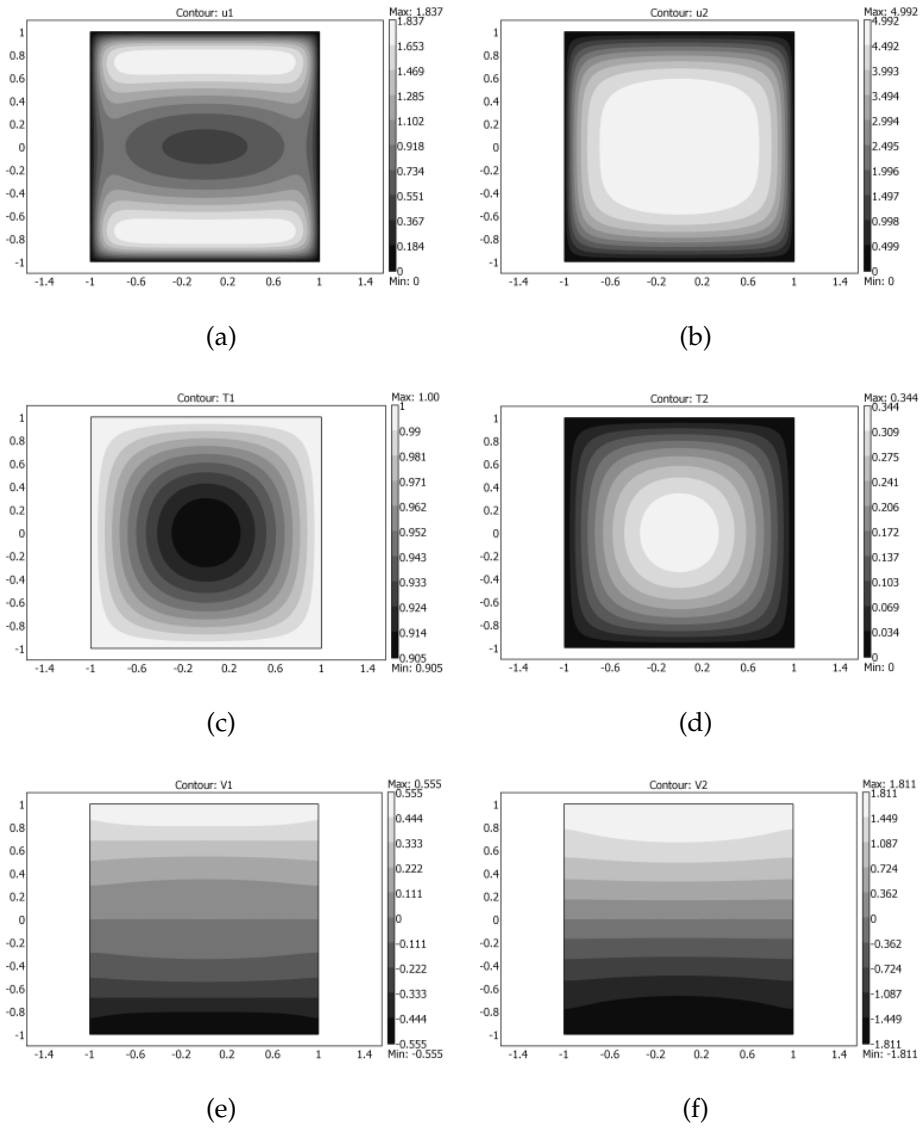


Figure 5.7 — Distributions of oscillation amplitudes for dimensionless velocity (a) (b), temperature (c) (d) and electric potential (e) (f), calculated for $Ha = 20$ and $\chi = 1$, in mixed convection regime, with $GR = 500$, $Pr = 0.05$ and $\Omega = 100$.

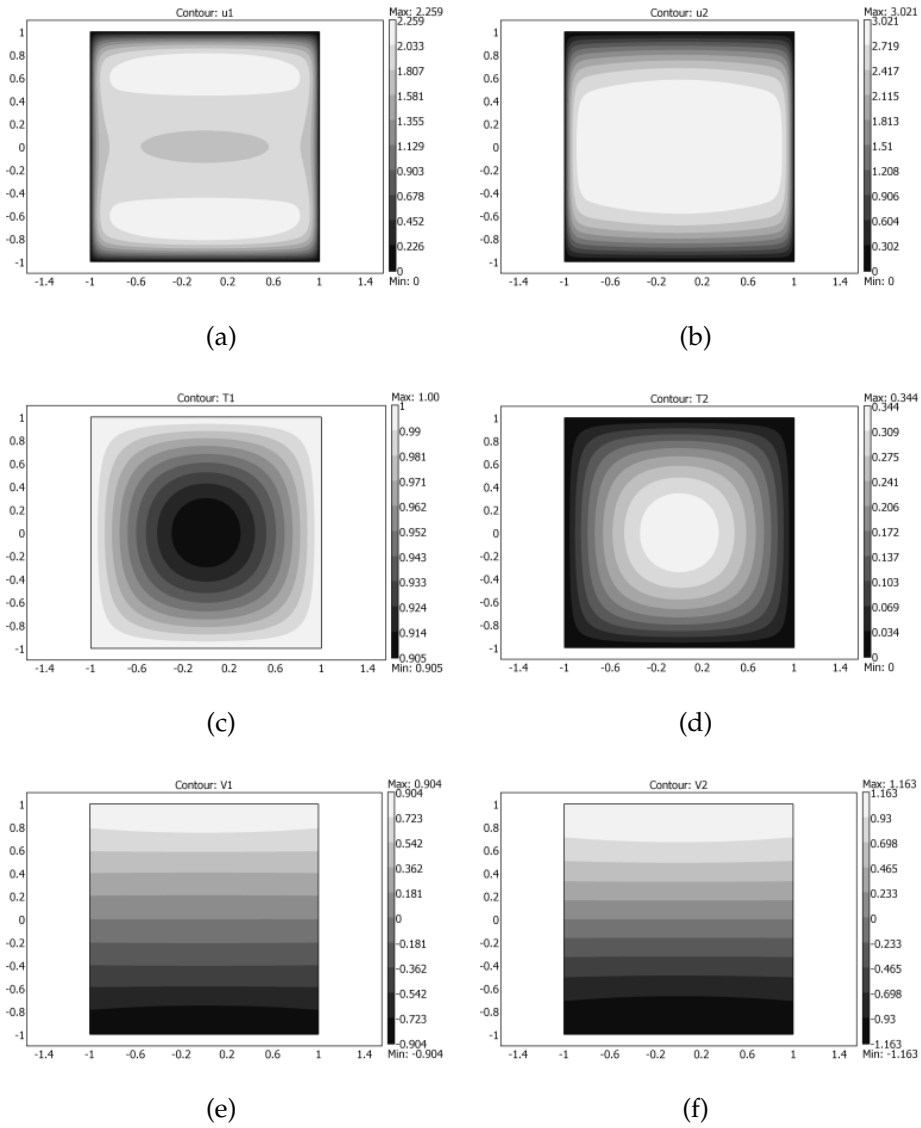


Figure 5.8 — Distributions of oscillation amplitudes for dimensionless velocity (a) (b), temperature (c) (d) and electric potential (e) (f), calculated for $Ha = 50$ and $\chi = 1$, in mixed convection regime, with $GR = 500$, $Pr = 0.05$ and $\Omega = 100$.

Table 5.3 — Values of the oscillating amplitudes of $f Re$ and Nu as a function of Ω . Results obtained for a square channel $\chi = 1$ in mixed convection regime, $GR = 500$.

Ω	$Pr = 0.05$			$Pr = 1$				
	$ Nu $	$Ha = 0$	$Ha = 1$	$Ha = 10$	$ Nu $	$Ha = 0$	$Ha = 1$	$Ha = 10$
		$ f Re $	$ f Re $	$ f Re $		$ f Re $	$ f Re $	$ f Re $
1	0.03	249.73	249.88	250.00	0.50	249.35	249.55	249.72
5	0.12	243.47	247.07	249.91	2.44	234.67	239.20	243.37
10	0.25	227.06	238.92	249.65	4.55	198.58	212.22	226.74
50	1.24	120.94	143.32	241.46	12.50	67.46	68.27	118.82
100	2.44	85.29	92.44	219.48	18.27	50.34	47.49	78.86
500	8.62	36.34	35.55	65.27	42.96	22.36	22.15	18.83
1000	12.50	25.82	25.54	26.78	61.47	15.81	15.75	11.86
5000	29.88	11.56	11.54	9.55	139.63	7.07	7.07	6.34

while $|f Re|$ decreases with Ω . Moreover, in Figure 5.5, the plots of $f_{1,2} Re$ and $Nu_{1,2}$ are reported. It may be noted that $f_2 Re$ shows some absolute maxima whose position is affected by Ha .

In Figure 5.6 the distributions of oscillation amplitudes for the components of velocity w_1 and w_2 (Figures 5.6(a) and 5.6(b)), of temperature θ_1 and θ_2 (Figures 5.6(c) and 5.6(d)), and of electric potential (Figures 5.6(e) and 5.6(f)) are reported for $Ha = 0$. Figures 5.7 and 5.8 show the same type of results for $Ha = 20$ and $Ha = 50$, respectively. The results show that w_1 has both positive and negative values for small values of Ha , while for higher values of Ha it is always positive. On the contrary, w_2 is always positive, but its maximum value across the sections decreases with increasing values of Ha . These results are in agreement with those already shown for the circular pipe.

5.5 Closure

In this chapter the effects of a transverse magnetic field on a steady periodic flow in a vertical rectangular channel, for several values of the channel aspect ratio were illustrated. The driving effect of the steady-periodic regime was the wall temperature, which was assumed uniform across the four walls and varying sinusoidally with time. The Boussinesq approximation was assumed to model buoyancy. The average temperature across the channel section was used as a reference for the linearization of the equation of state $\rho = \rho(T)$. The dimensionless local balance equations were solved numerically in steady-periodic regime using the commercial software *COMSOL Multiphysics*.

In the particular case of forced convection, the numerical results shown in the present work were compared with those available in the literature, obtaining a perfect agreement in the determination of the Fanning friction factor for several values of the channel aspect ratio.

Moreover, in case of steady periodic mixed convection with MHD effects, the amplitudes of the oscillating components of the Fanning friction factor and of the Nusselt number were computed as functions of Ω and Ha . It was shown that the value of $|Nu|$ increases for increasing values of Ω and that $f_1 Re$ is an always decreasing function of the same Ω . Finally, it was proved the existence of a local maximum of $f_2 Re$ for each value of Ha , whose position on the Ω axis shifts towards higher values for increasing values of Ha .

Chapter 6

Conclusions

The main objective of this thesis has been to analyze the heat transfer and fluid dynamics phenomena which are related to steady periodic magnetohydrodynamic mixed convection flows in channels and ducts. In other terms, the flow of an electrically conductive fluid enclosed in channels of various geometries has been studied, assuming the onset of a steady periodic regime induced by an oscillating driving effect (*e.g.* wall temperatures) and under the influence of an externally applied magnetic field, which is not perturbed by the motion of the fluid.

To this aim, a comprehensive literature search has been carried out first, to build the bulk of the govern equations needed to describe the strongly linked behaviors of the velocity, temperature and electric potential fields spanning across the sections of the geometries under examination. In particular the book by Welty *et al.* (13) was used as the reference text for the definition of the fluid dynamics and heat transfer phenomena in mixed convective flow. The books by Roberts (14), Shercliff (15) and Kulikovskiy (16) represented the reference for the classical formulation of ideal MHD, while the book from Müller and Bühler (17) provided the necessary insights in the problem of MHD flow in closed geometries.

Using the aforementioned references, the equation system shown in Chapter two was obtained, the boundary conditions were classified and related to practical applications, and the dimensional analysis of the equa-

tion system has been performed, in order to build up an analytical tool which is able to solve problems with widely different scales, from small channel flow of molten salts to liquid metal flow of cast metal, and so on.

The analytical tool was exploited first in Chapter three, where the solution of the mixed convective flow in a vertical parallel channel in steady periodic regime has been presented, accompanied by a numerical extension of the solution, to account for nonlinear effects which could not be handled by the analytical model. A comprehensive set of results was presented, and the main conclusions of the Chapter showed that the external transverse magnetic field influences both the average velocity distribution and the amplitude of the oscillating velocity component. In particular for increasing values of the Hartmann number, the average velocity profile changes from that of the classical non-magnetic case to the so-called *Hartmann profile*, characterized by a uniform velocity at the core and steep velocity gradients at the walls. Moreover, for increasing values of the Hartmann number it was shown that the critical ratio of the Grashof over Reynolds number for the onset of flow reversal increases accordingly. Finally, with respect to the oscillating components of velocity, it was shown that the effect of the transverse magnetic field is to progressively reduce their amplitudes, up to almost completely suppress them.

In Chapter four, a case of MHD steady periodic mixed convection in a vertical circular pipe was studied using an analytical and numerical approach. In particular, the problem was solved analytically up to the decomposition of the main time-dependent equation system in two stationary subsystems representing the average and oscillating components of the velocity, temperature and electric potential fields. Afterwards, the two systems were solved independently using a commercial finite element solver, *Comsol Multiphysics*. In the solution it was shown that, in the particular case of forced convection, the numerical results for the Fanning friction factor were in perfect agreement with those available in the literature. Moreover, in case of steady periodic mixed convection with MHD effects, it was shown that the value of the dimensionless average heat flux $|Nu|$ increases for increasing values of the dimensionless pulsation Ω and

that the $f_1 Re$ component of the dimensionless Fanning friction factor is an always decreasing function of Ω , while the $f_2 Re$ has a local maximum for each value of Ha , whose position on the Ω axis shifts towards higher values for increasing values of Ha .

In Chapter five, another case of 2D MHD steady periodic mixed convection was studied, this time regarding a vertical rectangular channel. Again an analytical and numerical approach was used, and solutions were provided for several values of, among other parameters, the channel aspect ratio. The problem was solved analytically up to the decomposition of the main time-dependent equation system in two stationary subsystems representing the average and oscillating components of the velocity, temperature and electric potential fields and, afterwards, the two systems were solved independently using the finite element solver *Comsol Multiphysics*, as in the previous Chapter. In the solution it was shown that, in the particular case of forced convection, the numerical results for the Fanning friction factor, computed for several values of the channel aspect ratio, were in perfect agreement with those available in the literature, thus proving the validity of the model. Furthermore, in the case of steady periodic mixed convection with MHD effects, the amplitudes of the oscillating components of the Fanning friction factor and of the Nusselt number were computed as functions of Ω , Ha and χ , the channel aspect ratio. It was shown that the influence of the magnetic field is relevant when the channel has $\chi > 1$, *i.e.* when the distance between the walls orthogonal to the field (the *Hartmann walls*) is smaller than the distance between the walls parallel to the field. In that case, the viscous stress is influenced both by the geometry of the conduit and by the interaction between the flow and the magnetic field, which modifies the wall velocity profile by increasing the local wall velocity gradient. Moreover, it was shown that the value of $|Nu|$ increases for increasing values of Ω and that $f_1 Re$ is an always decreasing function of Ω itself. Finally, it was proved the existence of a local maximum of $f_2 Re$ for each value of Ha , whose position on the Ω axis shifts towards higher values for increasing values of Ha .

6.1 Closure

In this work both analytical and numerical solutions for MHD mixed convection flows in steady periodic regime has been presented. The results obtained have shown that the effect of magnetic field has great influence on the mixed convection heat exchange and fluid flow in steady periodic regime, both in terms of flow pattern modification due to Lorentz forces and heat generation due to Joule effect. A natural continuation of this work would focus on exploring more realistic fluid wall electrical interactions and magnetic field distributions, and on extending the scope of the research to three dimensional geometries, eventually with an eye to more practical, technological applications (*e.g.* fusion reactor blanket flows). This work can be considered as an extension of the research carried out by Barletta *et al.* on the analysis of mixed convection flows in steady periodic regime without MHD effects (9)-(10).

Appendix A

Auxiliary functions for the parallel channel problem

$$\Phi_1(\xi, M, \Omega) = e^{+\xi\sqrt{M^2+i\Omega}} \quad (\text{A.1})$$

$$\Phi_2(\xi, M, \Omega) = e^{-\xi\sqrt{M^2+i\Omega}} \quad (\text{A.2})$$

$$\begin{aligned} \Phi_3(\xi, M, \Omega) = & -\Phi_1(\xi, M, \Omega) \int_0^\xi \frac{\Phi_2(s, M, \Omega)}{-2\sqrt{M^2+i\Omega}} ds + \\ & + \Phi_2(\xi, M, \Omega) \int_0^\xi \frac{\Phi_1(s, M, \Omega)}{-2\sqrt{M^2+i\Omega}} ds \quad (\text{A.3}) \end{aligned}$$

$$\begin{aligned} \Phi_4(\xi, M, \Omega, Pr) = & -\Phi_1(\xi, M, \Omega) \int_0^\xi \frac{\Phi_2(s, M, \Omega)\Phi_R(s, \Omega, Pr)}{-2\sqrt{M^2+i\Omega}} ds + \\ & + \Phi_2(\xi, M, \Omega) \int_0^\xi \frac{\Phi_1(s, M, \Omega)\Phi_R(s, \Omega, Pr)}{-2\sqrt{M^2+i\Omega}} ds \quad (\text{A.4}) \end{aligned}$$

$$\Phi_R(\xi, \Omega, Pr) = -\frac{-e^{1/4(1-4\xi)\sqrt{i\Omega Pr}} + e^{1/4(3+4\xi)\sqrt{i\Omega Pr}}}{-1 + e^{\sqrt{i\Omega Pr}}} \quad (\text{A.5})$$

$$\Psi_{1,a}(M, \Omega, Pr) = A_{1,a}(M, \Omega, Pr) \int_{-1/4}^{1/4} \Phi_1(\xi, M, \Omega) \xi \quad (\text{A.6})$$

$$\Psi_{1,b}(M, \Omega) = A_{1,b}(M, \Omega) \int_{-1/4}^{1/4} \Phi_1(\xi, M, \Omega) \xi \quad (\text{A.7})$$

$$\Psi_{2,a}(M, \Omega, Pr) = A_{2,a}(M, \Omega, Pr) \int_{-1/4}^{1/4} \Phi_2(\xi, M, \Omega) \xi \quad (\text{A.8})$$

$$\Psi_{2,b}(M, \Omega) = A_{2,b}(M, \Omega) \int_{-1/4}^{1/4} \Phi_2(\xi, M, \Omega) \xi \quad (\text{A.9})$$

$$\Psi_3(M, \Omega) = \int_{-1/4}^{1/4} \Phi_3(\xi, M, \Omega) \xi \quad (\text{A.10})$$

$$\Psi_4(M, \Omega, Pr) = \int_{-1/4}^{1/4} \Phi_4(\xi, M, \Omega, Pr) \xi \quad (\text{A.11})$$

$$A_{1,a}(M, \Omega, Pr) = -\frac{\Phi_2(1/4, M, \Omega)\Phi_4(-1/4, M, \Omega, Pr) - \Phi_2(-1/4, M, \Omega)\Phi_4(1/4, M, \Omega, Pr)}{-\Phi_1(1/4, M, \Omega)\Phi_2(-1/4, M, \Omega) + \Phi_1(-1/4, M, \Omega)\Phi_2(1/4, M, \Omega)} \quad (\text{A.12})$$

$$A_{1,b}(M, \Omega) = -\frac{-\Phi_2(1/4, M, \Omega)\Phi_3(-1/4, M, \Omega) + \Phi_2(-1/4, M, \Omega)\Phi_3(1/4, M, \Omega)}{-\Phi_1(1/4, M, \Omega)\Phi_2(-1/4, M, \Omega) + \Phi_1(-1/4, M, \Omega)\Phi_2(1/4, M, \Omega)} \quad (\text{A.13})$$

$$A_{2,a}(M, \Omega, Pr) = -\frac{\Phi_1(1/4, M, \Omega)\Phi_4(-1/4, M, \Omega, Pr) - \Phi_1(-1/4, M, \Omega)\Phi_4(1/4, M, \Omega, Pr)}{\Phi_1(1/4, M, \Omega)\Phi_2(-1/4, M, \Omega) - \Phi_1(-1/4, M, \Omega)\Phi_2(1/4, M, \Omega)} \quad (\text{A.14})$$

$$A_{2,b}(M, \Omega) = -\frac{-\Phi_1(1/4, M, \Omega)\Phi_3(-1/4, M, \Omega) + \Phi_1(-1/4, M, \Omega)\Phi_3(1/4, M, \Omega)}{\Phi_1(1/4, M, \Omega)\Phi_2(-1/4, M, \Omega) - \Phi_1(-1/4, M, \Omega)\Phi_2(1/4, M, \Omega)} \quad (\text{A.15})$$


```

write (*,"(A)",advance='no') "##"
endif
if (i1==step_per) then
write (*,"(A)",advance='no') "]"
endif

if (mod(i1,step_per/scan_pt) == 0) then
k=k+1
u4t_mat(1,k)=tt-(i0-1)*2*pi
u4t_mat(2,k)=u5(11)
u4t_mat(3,k)=u5(21)
u4t_mat(4,k)=u5(31)
u4t_mat(5,k)=u5(41)
endif

if (mod(i1,step_per/freq) == 0) then
write (12,103) tt,u5
endif

do i2=1,nr
u1(i2)=u2(i2)
u2(i2)=u3(i2)
u3(i2)=u4(i2)
u4(i2)=u5(i2)
enddo

if (mod(i1,step_per/mat_pt) == 0) then
k2=k2+1
do i2=1,nr
u_mat(i2,k2)=u5(i2)
th_mat(i2,k2)=t5(i2)
enddo
t_vec(k2)=tt
endif

enddo

!CCCCCC CONTROLLO CONVERGENZA PERIODICO STABILIZZATO CCCCCCCCCCCCCCCCCCCCCC

conv_ps=0.0
do i=1,nr
conv_ps=conv_ps+(u11(i)-u5(i))*2
u11(i)=u5(i)
enddo

print *
print *
write (*,"(A,E14.6)") "## Residual.....", conv_ps

!CCCCCCCCCCCCCCCCCCCCCCCCCCCCCCCCCCCCCCCCCCCCCCCCCCCCCCCCCCCCCCCCCCCCC

enddo

!CCCCCCCCCCCCCCCCCCCCCCCCCCCCCCCCCCCCCCCCCCCCCCCCCCCCCCCCCCCCCCCCCCCCC
!CCCCCCCCCCCCCCCCCCCCCCCCCCCCCCCCCCCCCCCCCCCCCCCCCCCCCCCCCCCCCCCCCCCCC
!CCCCCCCCCCCCCCCCCCCCCCCCCCCCCCCCCCCCCCCCCCCCCCCCCCCCCCCCCCCCCCCCCCCCC

write (9,"(5A14)") "Time", "u(0.1,t)", "u(0.2,t)", "u(0.3,t)", "u(0.4,t)"
write (9,101) u4t_mat

!CCCCCCCCCCCCCCCCCCCCCCCCCCCCCCCCCCCCCCCCCCCCCCCCCCCCCCCCCCCCCCCCCCCCC

u_a=(maxval(u_mat,dim=2)+minval(u_mat,dim=2))/2.
u_b=(1./gr)*(maxval(u_mat,dim=2)-minval(u_mat,dim=2))/2.

th_a=(maxval(th_mat,dim=2)+minval(th_mat,dim=2))/2.
th_b=(maxval(th_mat,dim=2)-minval(th_mat,dim=2))/2.

```


Bibliography

- [1] J.P. Garandet, T. Alboussiere, R. Moreau, Buoyancy driven convection in a rectangular enclosure with transverse magnetic field. *Int. J. Heat Mass Transfer*, 35, pp. 741-748, 1992.
- [2] B. Pan, B. Q. Li, Effect of magnetic fields on oscillating mixed convection. *Int. J. Heat Mass Transfer*, 41, pp. 2705-2710, 1998.
- [3] M. J. Al-Khawaja, R. K. Agarwal, R. A. Gardner, Numerical study of magneto-fluid-mechanic combined free-and-forced convection heat transfer. *Int. J. Heat Mass Transfer*, 42, pp. 467-475, 1999.
- [4] U. Burr, U. Müller, Rayleigh-Benard convection in liquid metal layers under the influence of a vertical magnetic field. *Phys. Fluids*, 13, pp. 3247-3257, 2001.
- [5] J.C. Umawathi, M. S. Malashetty, Magnetohydrodynamic mixed convection in a vertical channel. *Int. J. Non-Linear Mechanics*, 40, pp. 91-101, 2005.
- [6] G. Sposito, M. Ciofalo, One-dimensional mixed MHD convection. *Int. J. Heat Mass Transfer*, 49, pp. 2939-2949, 2006.
- [7] P. A. Davidson, Magnetohydrodynamics in materials processing. *Annu. Rev. Fluid Mech.*, 31, pp. 273-300, 1999.
- [8] J. Reimann, L. Bühler, C. Mistrangelo and S. Molokov, Magnetohydrodynamic issues of the HCLL blanket, *Fusion Engineering and Design*, 81, pp. 625-629, 2006

- [9] A. Barletta, E. Zanchini, Time-periodic laminar mixed convection in an inclined channel, *Int. J. Heat and Mass Transfer*, 46, pp. 551-563, 2003.
- [10] A. Barletta, E. Rossi di Schio, Mixed convection flow in a vertical circular duct with timeperiodic boundary conditions: steady-periodic regime. *Int. J. Heat Mass Transfer*, 47, pp. 3187-3195, 2004.
- [11] R.K. Shah, A.L. London, Laminar forced convection in ducts. In: T.F. Irvine, J.P. Hartnett (Ed.), *Advances in Heat Transfer*, Academic Press, New York, 1978.
- [12] J.S. Walker, Magneto hydrodynamic flows in rectangular ducts with thin conducting walls, *Journal de Mecanique*, 20, pp. 79-112, 1981
- [13] J. Welty, E. Wicks, L. Rorrer, E. Wilson, *Fundamentals of Momentum, Heat and Mass Transfer*, 5th Edition, John Wiley & Sons, January 2008
- [14] P.H. Roberts, *An Introduction to Magnetohydrodynamics*, American Elsevier Pub. Co, 1967
- [15] J.A. Shercliff, *A Textbook of Magnetohydrodynamics*, Pergamon Press, 1965
- [16] A.G. Kulikovskiy, *Magnetohydrodynamics*, Addison-Wesley, 1965
- [17] U. Müller, L. Bühler, *Magnetohydrodynamics in Channels and Containers*, Springer, 2001